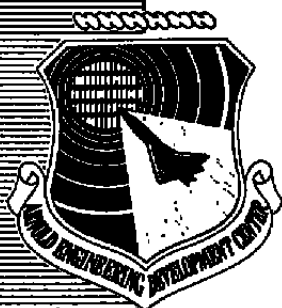


OCT 7 1982

AEDC-TR-82-9
AFRPL-TR-82-17

c.5



Operating Characteristics of an Ablative Pulsed Plasma Engine

R. Dawbarn, R. L. McGuire, S. L. Steely, and J. G. Pipes
Calspan Field Services, Inc.

July 1982

Final Report for Period January 1 — September 30, 1981

Approved for public release; distribution unlimited.

Property of U. S. Air Force
AEDC LIBRARY
F40600-81-C-0004

**ARNOLD ENGINEERING DEVELOPMENT CENTER
ARNOLD AIR FORCE STATION, TENNESSEE
AIR FORCE SYSTEMS COMMAND
UNITED STATES AIR FORCE**

NOTICES

When U. S. Government drawings, specifications, or other data are used for any purpose other than a definitely related Government procurement operation, the Government thereby incurs no responsibility nor any obligation whatsoever, and the fact that the government may have formulated, furnished, or in any way supplied the said drawings, specifications, or other data, is not to be regarded by implication or otherwise, or in any manner licensing the holder or any other person or corporation, or conveying any rights or permission to manufacture, use, or sell any patented invention that may in any way be related thereto.

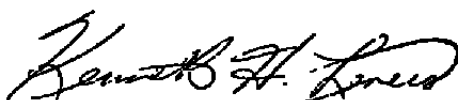
Qualified users may obtain copies of this report from the Defense Technical Information Center.

References to named commercial products in this report are not to be considered in any sense as an endorsement of the product by the United States Air Force or the Government.

This report has been reviewed by the Office of Public Affairs (PA) and is releasable to the National Technical Information Service (NTIS). At NTIS, it will be available to the general public, including foreign nations.

APPROVAL STATEMENT

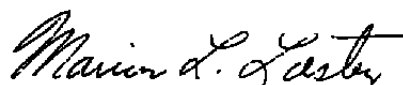
This report has been reviewed and approved.



KENNETH H. LENERS, Captain, USAF
Directorate of Technology
Deputy for Operations

Approved for publication:

FOR THE COMMANDER



MARION L. LASTER
Director of Technology
Deputy for Operations

UNCLASSIFIED

SECURITY CLASSIFICATION OF THIS PAGE (When Data Entered)

REPORT DOCUMENTATION PAGE		READ INSTRUCTIONS BEFORE COMPLETING FORM
1. REPORT NUMBER AEDC-TR-82-9 AFRPL-TR-82-17	2. GOVT ACCESSION NO.	3. RECIPIENT'S CATALOG NUMBER
4. TITLE (and Subtitle) OPERATING CHARACTERISTICS OF AN ABLATIVE PULSED PLASMA ENGINE	5. TYPE OF REPORT & PERIOD COVERED Final Report, January 1 - September 30, 1981	
	6. PERFORMING ORG REPORT NUMBER	
7. AUTHOR(s) R. Dawbarn, R. L. McGuire, S. L. Steely, and J. G. Pipes, Calspan Field Services, Inc., AEDC Division	8. CONTRACT OR GRANT NUMBER(s)	
9. PERFORMING ORGANIZATION NAME AND ADDRESS Arnold Engineering Development Center/DOT Air Force Systems Command Arnold Air Force Station, TN 37389	10. PROGRAM ELEMENT PROJECT, TASK AREA & WORK UNIT NUMBERS Program Element 62302F	
11. CONTROLLING OFFICE NAME AND ADDRESS Arnold Engineering Development Center/DOS Air Force Systems Command Arnold Air Force Station, TN 37389	12. REPORT DATE July 1982	
	13. NUMBER OF PAGES 88	
14. MONITORING AGENCY NAME & ADDRESS (if different from Controlling Office)	15. SECURITY CLASS. (of this report) UNCLASSIFIED	
	15a. DECLASSIFICATION/DOWNGRADING SCHEDULE N/A	
16. DISTRIBUTION STATEMENT (of this Report) Approved for public release; distribution unlimited.		
17. DISTRIBUTION STATEMENT (of the abstract entered in Block 20, if different from Report)		
18. SUPPLEMENTARY NOTES Available in Defense Technical Information Center (DTIC).		
19. KEY WORDS (Continue on reverse side if necessary and identify by block number) electrical propulsion plasma propulsion spacechambers spacecraft contamination solid propellant		
20. ABSTRACT (Continue on reverse side if necessary and identify by block number) The Teflon® pulsed thruster is being considered as an attitude control and station-keeping device for spacecraft and satellites. In determining the compatibility of the pulsed plasma thruster with spacecraft systems, it is necessary to assess the potentially harmful effects which the exhaust products may have on various spacecraft surfaces. Previous efforts to acquire data in space environmental chambers have had limited success due to the interferences caused by exhaust products scattering from the test		

UNCLASSIFIED

SECURITY CLASSIFICATION OF THIS PAGE (When Data Entered)

20. ABSTRACT, Concluded.

facility walls and pumping panels. This report, along with the companion report, "A Study of Test Techniques for Evaluating Ablative Plasma Engines in Vacuum Test Cells," AEDC-TR-81-8 (October 1981), contains data on the operating characteristics of a prototype engine. These data include capacitor discharge currents, fuel usage rates, plasma current between the electrodes, magnetic field maps, VUV and visible spectra with both spatial and temporal resolution, high-speed photographs of the plasma discharge, mass spectrometer analysis of the gases produced by both the engine and the plasma reaction with the test chamber walls, ion gage detection of the neutral gas expansion from the engine, and a time-of-flight quartz crystal microbalance measurement of solid material emitted in the forward flow of the engine. All of these measurements are referenced to the same time zero for each engine pulse, and thus these experiments provide a consistent set of data which can be compared temporally.

PREFACE

The work reported herein was conducted by the Arnold Engineering Development Center (AEDC), Air Force Systems Command (AFSC), for the Air Force Rocket Propulsion Laboratories, (AFRPL), Edwards Air Force Base, California. Lieutenant R. Furstenau was the AFRPL project manager. The results of the research were obtained by Calspan Field Services, Inc., AEDC Division, operating contractor for the Aerospace Flight Dynamics testing effort at the AEDC, AFSC, Arnold Air Force Station, Tennessee, under Project Number D220VM (V32M-B5). The UV spectral data were acquired by J. G. Pipes, L. L. Price, and D. S. Brooks, Calspan Field Services, Inc. Captain Kenneth H. Leners, AEDC/DOT, was the Air Force project manager. The manuscript was submitted for publication on February 2, 1982.

CONTENTS

	<u>Page</u>
1.0 INTRODUCTION	7
2.0 APPARATUS	7
2.1 Pulsed Plasma Engine	7
2.2 Vacuum Chamber	8
2.3 Instrumentation	9
3.0 PROCEDURES AND RESULTS	10
3.1 Operation of the Plasma Engine	10
3.2 Mapping the Plasma Current	17
3.3 Mapping the Magnetic Fields	20
3.4 Photons Produced by the Engine	30
3.5 Gases Produced by the Plasma Engine	53
3.6 Solids Produced by the Engine	70
4.0 SUMMARY	79
4.1 Operation of the Plasma Engine	79
4.2 Plasma Currents	79
4.3 Magnetic Fields	79
4.4 Photons Produced by the Engine	79
4.5 Gases Produced by the Engine	80
4.6 Solids Produced by the Engine	80
5.0 CONCLUSIONS	81
6.0 RECOMMENDATIONS	81
REFERENCES	83

ILLUSTRATIONS

Figure

1. Plasma Engine in Gimbal Mount	8
2. Vacuum Chamber	9
3. Calibration of Rogowski Coil	12
4. Engine Discharge (64- μ fd Capacitors)	14
5. Engine Discharge (80- μ fd Capacitors)	14
6. Rogowski Coil (80- μ fd Capacitors)	15
7. Plan View of Current Probe in Nozzle	16
8. Photograph of Current Probe in Nozzle	17
9. Axial Current Probe	18

<u>Figure</u>	<u>Page</u>
10. Axial Velocity of Plasma Current	19
11. Magnetic Probe, X-Axis (Comparison of Capacitors)	21
12. Magnetic Probe, X-Axis (64- μ fd Capacitors)	22
13. Magnetic Probe (80- μ fd Capacitors)	24
14. Magnetic Probe Location	28
15. Magnetic Probe (Z-Axis)	29
16. Photomultiplier Detector	30
17. Plasma Passing Through Baffle	31
18. Plan View of Spectrometer Installation	32
19. Field of View of Spectrometer	32
20. VUV/UV Spectrum	33
21. Spatial Regions Observed During Temporal VUV/UV Measurements	35
22. Intensity of $A1^+$ (1762 Å) Radiation versus Time	37
23. Intensity of C (1278 Å) Radiation versus Time	38
24. Intensity of C^+ (1324 Å) Radiation versus Time	38
25. Intensity of C^{++} (1176 Å) Radiation versus Time	39
26. C^+ and C^{++} Radiation as a Function of Time	39
27. Intensity of F^+ Radiation versus Time	40
28. Decay of O and H Radiation as a Function of Engine Pulse Number	41
29. Spectrometer Positions for the Doppler Shift Measurements	42
30. Co-added F and A Spectral Lines in Second Order	43
31. Reciprocal Dispersion versus Wavelength	44
32. Photographs of Plasma (Side View)	47
33. Photographs of Plasma with Glass Nozzle	49
34. Photographs of Plasma with No Nozzle (45 deg)	51
35. Installation of Mass Spectrometer	53
36. Calibrated Gas Addition System	54
37. Engine (Small Capacitors)	57
38. Engine (Large Capacitors), Mass Nos. 0 to 110	57
39. Engine (Large Capacitors), Mass Nos. 0 to 36	58
40. Carbon Monoxide (CO), Pressure = 1.8×10^{-5} mm	59
41. Nitrogen (N_2), Pressure = 2.4×10^{-5} mm	59
42. Acetylene (C_2H_2)	60
43. Teflon Sublimation	61
44. Engine Pulse	61
45. Pressure Rise (Masses 28, 31, 69)	62
46. Engine Pulse (All Pumps Closed), 64- μ fd Capacitors	63

<u>Figure</u>	<u>Page</u>
47. Engine Pulse (All Pumps Closed), 80- μ fd Capacitors	64
48. Engine Pulse (Mass 28)	65
49. Engine Pulse (Mass 31)	65
50. Cryopanel, 300°K	66
51. Cryopanel, 77°K	66
52. Cryopanel, - 32°C	67
53. Location of Ion Gage	68
54. Neutral Gas Molecules	68
55. Ion Pulse (Mass 12)	69
56. Carbon Ion Signal	70
57. Ablating Edge of Teflon Fuel Block	71
58. Scanning Electron Micrographs of Deposits	71
59. Material Collected on Test Chamber Walls	73
60. SEM Photograph of Surface of Deposit (12,000X)	73
61. Schematic of Shadow Box	74
62. Specular Absorption by Shadow Box Deposits	75
63. QCM and Chopper Wheel	76
64. Mass Collected by QCM	77
65. IR Absorption Spectrum of Deposit on ATR Plate	78

TABLES

1. Inductance and Resistance of Plasma	13
2. Mass Ablated from Teflon Fuel Bars (256 μ fd)	16
3. Mass Ablated from Teflon Fuel Bars (320 μ fd)	16
4. Species and Associated Wavelengths Identified from the VUV/UV Spectral Survey	34
5. Species Observed in VUV/UV Temporal Measurements	36
6. Velocity Measurement Results	44
7. Ratios of Line Intensities	45
8. Calibration Factors for Various Gases	56

APPENDIX

A. DETERMINATION OF EFFECTIVE R AND L FOR PLASMA DISCHARGE	85
NOMENCLATURE	87

1.0 INTRODUCTION

The Teflon® -fueled pulsed plasma engine is being developed as an attitude control and station-keeping thruster for satellites. In order to determine the compatibility of the pulsed plasma engine with satellite systems it is necessary to fully characterize the thruster's exhaust plume: the exhaust products, the spatial distribution of these products, and their velocities. These data are required in order to determine whether the exhaust plume will product any harmful effects on sensitive satellite components such as thermal control coatings and optical surfaces.

In the past, computer codes such as CONTAM have been used to predict contamination from various liquid monopropellant and bipropellant engines. Basic information concerning the operating characteristics of the plasma engine is needed so that comparable computer codes can be developed. In addition, direct measurement of gas and particle fluxes, especially into the backflow region of the engine, is required both for future verification of the code and for immediate satellite systems evaluation.

The work reported in this document is a continuation of the research reported in AEDC-TR-81-8, October 1981, entitled "A Study of Test Techniques for Evaluating Ablative Plasma Engines in Vacuum Test Cells." In the interest of avoiding repetition, it is suggested that the reader consult the above report for a more detailed introduction than is furnished here. The objectives of this phase of the program are 1) to provide information on the operating characteristics of a prototype plasma engine which might provide a starting point for developing a computer model, and 2) to evaluate methods of making measurements of the plasma and gas flux from future plasma engines.

2.0 APPARATUS

2.1 PULSED PLASMA ENGINE

The prototype engine is shown mounted in a gimbal system (Fig. 1). The rectangular nozzle is made of a ceramic material and is 3.5 in. wide by 4.0 in. high at its exit. The copper electrodes, down which the plasma is accelerated, are visible inside the nozzle. The anode is located at the bottom and the cathode at the top. The body of this engine is approximately an 18-in. cube, which houses four storage capacitors. The total capacitance of the units supplied with the engine was 256 μ fd. During this test series these capacitors were replaced with larger units having a total capacitance of 320 μ fd. The power supplies which provided the high voltages to charge the capacitors and to trigger the spark plug igniter were located outside the vacuum chamber and were connected to the engine via insulated feedthroughs.

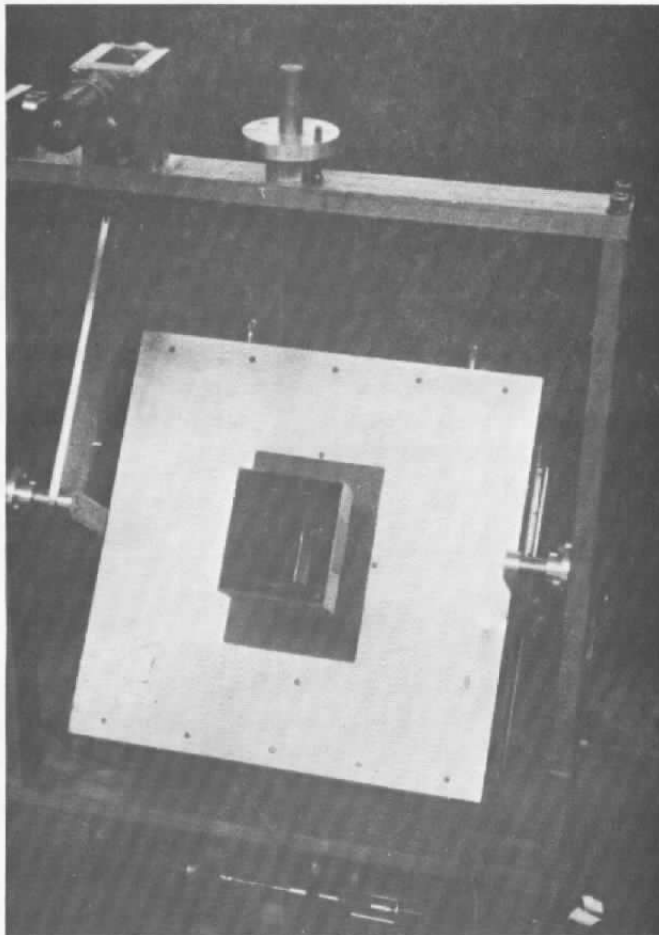


Figure 1. Plasma engine in gimbal mount.

2.2 VACUUM CHAMBER

The AEDC molecular beam chamber was modified by adding two spool pieces to lengthen the test section. A schematic of the chamber is shown in Fig. 2. In order to more clearly display specific components, the length-to-diameter ratio is distorted in this figure. The dimensions are 150 in. long by 36 in. in diameter. The chamber is actually two separately pumped vacuum sections coupled via a 6-in.-diam orifice. Plates with various size skimmers can be installed at this location to isolate the two sections. The engine section has a cryoliner which can be cooled to 77°K with liquid nitrogen. It is pumped with two 6-in. diffusion pumps, each fitted with cryogenic cold traps and isolation gate valves. Its base pressure in this configuration is 5×10^{-7} torr.

The motor was installed in a gimbal system. Both the horizontal and vertical axes of rotation were located at the front face of the capacitor housing. With this mounting the exit of the nozzle moved up or down as the engine was tilted. This permitted the installation of a VUV spectrometer with a fixed field of view, and the exit plane of the nozzle could be scanned by tilting the engine.

A baffle not shown in Fig. 2 was installed during the latter part of the tests. It was constructed of 304 stainless steel sheet and could be baked out *in situ* by heat supplied from two 800-w quartz heat lamps.

The far end of the vacuum chamber is pumped by a 10-in.-diam and a 6-in.-diam diffusion pump and has an LN₂-cooled cryopanel. Its base pressure in this configuration is 1×10^{-7} torr. The instrument mounting platform in this section can be remotely positioned in the X-Y plane. Probes which were used to map the electromagnetic fields at the plasma engine were mounted on this platform and extended through the opening between the vacuum chambers.

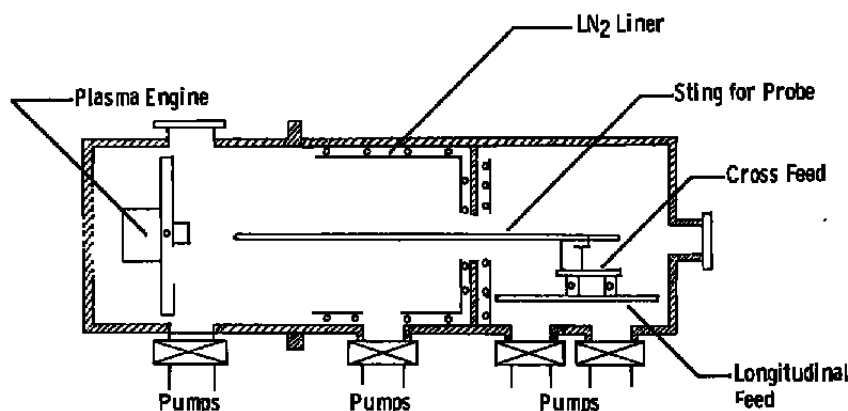


Figure 2. Vacuum chamber.

2.3 INSTRUMENTATION

The standard instrumentation on the vacuum chamber consists of ion and thermocouple gages used to monitor vacuum conditions and copper constantan thermocouples which record cryopanel temperatures. The additional instruments used in this test are noted briefly at this point and are subsequently described in more detail in that portion of the test where they are the focal point of the measurement.

A quadrupole mass spectrometer was used to monitor the gases produced by the engine firings. The instrument was tuned to cover two mass ranges. In the low range it scanned from 1 to 36 amu. In the medium range it scanned from 10 to 110 amu. The spectrometer was also calibrated so that it could be tuned to a specific mass number and thus record the temporal history of that mass number during and after an engine firing.

Attenuated total reflectance (ATR) plates were used to collect contaminant material in the chamber. These plates were operated at 300°K; they were removed from the vacuum chamber after a test sequence and were analyzed in a Beckman IR spectrometer. Absorption spectra in the range from 2.5 to 50 μm were recorded.

A quartz crystal microbalance (QCM) operating at 300°K were also used to collect material emitted by the engine. This QCM was fitted with a rotating chopper wheel which was synchronized to the engine trigger sequencer. Specific delays could be dialed into the sequencer to vary the time between the engine pulse and the full open position of the chopper wheel in front of the QCM.

High-speed photographs of the plasma were taken with a 35-mm camera fitted with a Kerr cell shutter. The Kerr cell was triggered by the engine sequencer with delay times ranging from 0 to 50 μsec . Kerr cell shutter speeds were set to give 1- μsec and 100-nsec exposures.

Magnetic fields were mapped with a glass probe fitted with a small search coil.

Two Rogowski coils were used to monitor current flows. One was mounted around the strip line from the capacitors to the electrodes and thus recorded the discharge of the capacitor bank. The other was mounted in a glass probe and was used to measure the current flowing in the plasma as it traveled down the electrodes.

A visible ultraviolet (VUV) spectrometer was used to view the exit plane of the nozzle. The instrument recorded the complete spectrum from 800 to 4000 Å. In addition, a spectrometer was used to monitor specific spectral lines and thus acquire temporal data for specific engine pulses.

Samples of material emitted by the engine were collected on witness plates. Some of these samples were analyzed under a scanning electron microscope (SEM), and others were used to define shadow patterns and determine the source of the deposit.

3.0 PROCEDURES AND RESULTS

3.1 OPERATION OF THE PLASMA ENGINE

The plasma engine used in these tests is identified in the previous report (Ref. 1) as the millipound engine with the long electrodes. During the performance of these tests several modifications were made. The first was the replacement of the four 64- μ fd storage capacitors with four 80- μ fd capacitors. A later modification was the removal of the ceramic nozzle, and the final configuration change was the installation of a conical glass nozzle. In some instances there is a duplication of data for the various configurations, thus permitting some comparisons of engine operating characteristics.

3.1.1 Timing Sequencer

Many of the experiments conducted in this test series required precise sequencing of the engine trigger pulse and the diagnostic instrument. This was provided by a master sequencing unit with four channels driven by a common 10-MHz clock. Channel A provided the basic pulse repetition rate of the engine, which for most of the tests was set at 65 sec. This was determined to be the time required for the chamber pressure to return to a baseline pressure of 5×10^{-6} torr or lower after an engine firing. Channel B was used to sequence the high-voltage charging relays, which closed at 25 sec into the repetition rate and opened 0.5 sec prior to the end of the repetition. Channel C was triggered by the ending of the channel A cycle and was used to trigger the engine spark plug. Channel C had a resolution of 100 nanoseconds and could be used to delay the engine pulse from 0 to 1 millisecond. Channel D was started by the same ending of the A cycle and provided a similar delay capability for any trigger to a diagnostic instrument.

3.1.2 Power Supplies

Two power supplies were used, one to provide the power for the engine capacitors and the other to trigger the spark plug igniter. The capacitors were charged to 2380 v with a current-limited power supply which was freely floating from ground. The spark plug power supply was also free floating and provided 500 v for the trigger pulse transformer. A 1- Ω resistor in the spark plug circuit was used to prevent any discharge from the plasma into the spark plug circuitry. The only engine problem during this complete program occurred toward the end of the tests when it was observed that the engine would occasionally misfire. The problem was traced to an excessively carboned spark plug and a shorted 1- Ω resistor. The resistor was replaced and the plug cleaned, and the tests were continued with no further misfire problems.

3.1.3 Engine Discharge

All of the experiments and data presented in this report can be referenced to the basic discharge of the capacitors into the plasma. Therefore, these data are presented for each of the engine configurations.

The Rogowski coil mounted in the engine was calibrated *in situ* using the engine capacitors and electrodes as well as an associated integrating circuit. The experimental apparatus is shown in Fig. 3 and consists of a calibrated pulse current coil and shorting bars clamped to the engine electrodes. The capacitors were charged to 90 v and then discharged through the electrodes via the aluminum shorting bar. The outputs of both the Rogowski coil and the calibrated pulse coil were recorded on a dual trace oscilloscope. Multiple discharges were recorded and averaged to provide a calibration of the Rogowski coil.

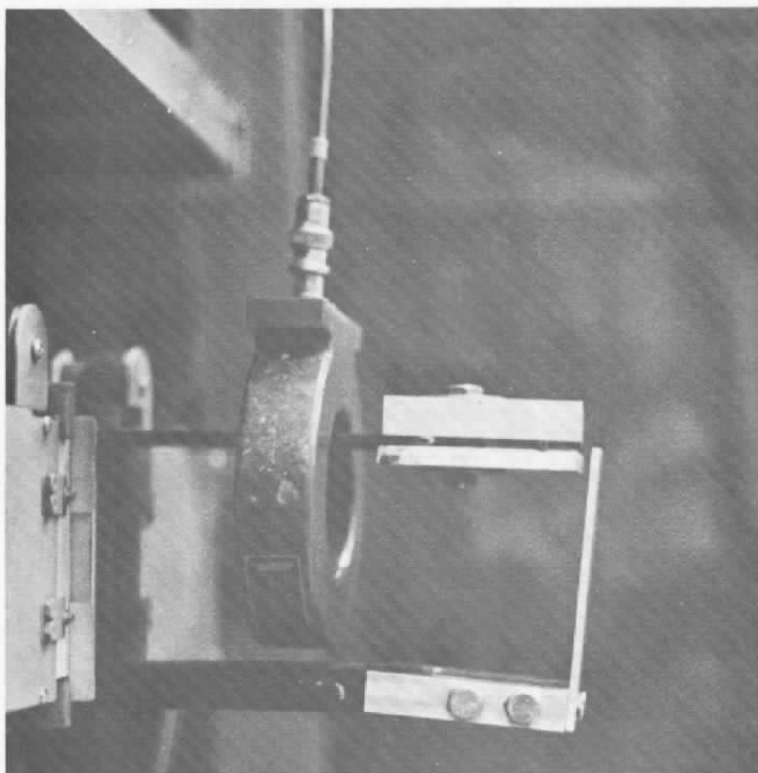


Figure 3. Calibration of Rogowski coil.

The character of the plasma engine discharge is defined by the capacitance of its storage capacitors, the inductance of the current loop formed by the electrodes and the plasma sheet, and the resistance of the combined electrodes and plasma. It can be described by the equation for a damped oscillator, as follows:

$$i = De^{-Rt/2L} \sin\left(\sqrt{\frac{1}{LC} - \frac{R^2}{4L^2}}t\right)$$

where

i = current, amps

R = resistance, ohms

D = normalization constant

L = inductance, henries

t = time, seconds

C = capacitance, farads

For this particular circuit, the actual values of the inductance and the resistance are a function of time since the plasma arc is ablating the Teflon fuel, thus adding current-carrying ions, and at the same time is traveling down the electrodes, thus increasing the inductance. However, by examining the overall characteristics of the discharge cycle as measured by the Rogowski coil, one can obtain time-independent effective values of both L and R . Details of the calculation are included in Appendix A. The values obtained are presented in Table 1.

Table 1. Inductance and Resistance of Plasma

Capacitance (C)	Inductance (L)	Resistance (R)
256 μ fd	8.9×10^{-8} H	1.9×10^{-2} ohm
320 μ fd	9.7×10^{-8} H	1.3×10^{-2} ohm

The measured discharges from both engine configurations are shown in Figs. 4 and 5. These cycles are compared to the theoretical damped oscillations calculated using the above values of L , C , and R .

The most obvious observation from these data is that the larger capacitors decreased the discharge frequency as expected. It is also noted that the increased energy resulted in lowering the effective resistance of the discharge due to more effective ablation and an increase in the current-carrying ions and electrons. The slight increase in the inductance with the larger capacitors could be due to changes in the internal structure of the capacitors as well as changes in the location of the plasma discharge between the electrodes. No changes in this basic discharge cycle were noted when the nozzle was removed from the engine for later tests.

Data are presented in Fig. 6 for the discharge of the engine fitted with 80- μ fd capacitors but charged to lower voltage levels. These data were acquired primarily to see if the apparent discontinuity which occurred part way in the reverse cycle of the discharge of the engine fitted with the 64- μ fd capacitors was due to the lower energy of the smaller capacitors.

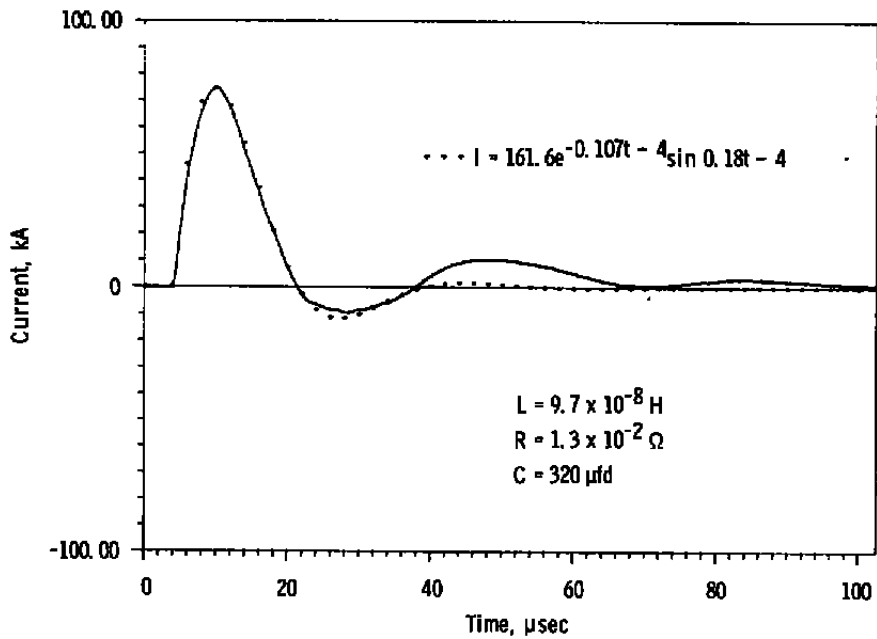


Figure 4. Engine discharge (64- μfd capacitors).

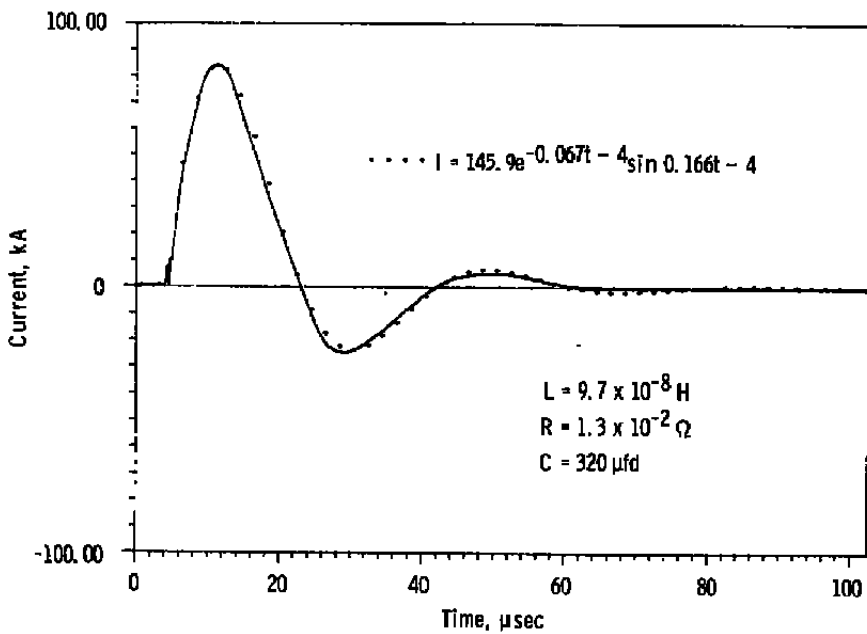


Figure 5. Engine discharge (80- μfd capacitors).

Apparently this was not the case since the data presented in Fig. 6 show well-behaved damped oscillations. One possible explanation is the fact that the Teflon blocks had burned nonuniformly due to a sticking feed spring when the engine had the 64- μ fd capacitors (Blocks LH2 and LH3, Fig. 7). When the 80- μ fd capacitors were installed, this feed problem was corrected and the Teflon fuel bar faces were machined square.

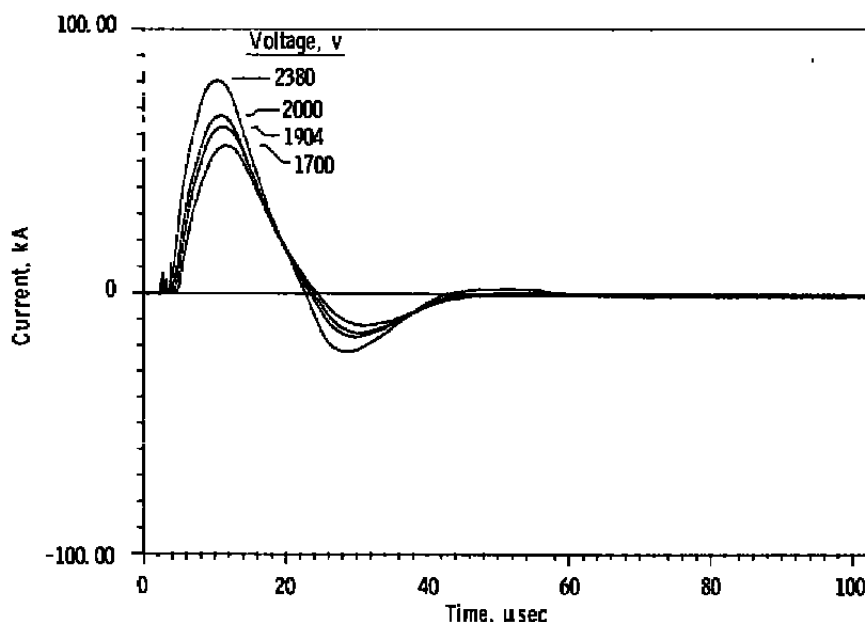


Figure 6. Rogowski coil (80- μ fd capacitors).

3.1.4 Fuel Rod Usage Rate

The average mass of Teflon ablated per engine pulse was measured for the engine fitted with both sets of capacitors. The engine was fired with a 65-sec duty cycle with the capacitors charged to 2380 v for all these tests. The data which show the mass loss per fuel block and the average total mass per engine pulse are presented in Tables 2 and 3. The location of specific fuel blocks identified as LH1, etc., can be determined by consulting Fig. 7. In this figure, the dashed lines on several of the blocks indicate the uneven erosion during the period the engine was operated with the smaller capacitors. The nonuniform ablation is reflected in the mass losses as recorded in the tabulated data.

Apart from the obvious increase in the usage rate with the larger capacitors, the only other difference noted was the more uniform erosion of the fuel blocks.

**Table 2. Mass Ablated from Teflon
Fuels Bars (256 μ fd)**

Bar	m, gm	Bar	m, gm
LH1	1.08	RH1	0.60
LH2	1.02	RH2	1.64
LH3	1.62	RH3	1.26

Total Mass Loss = 7.22 gm

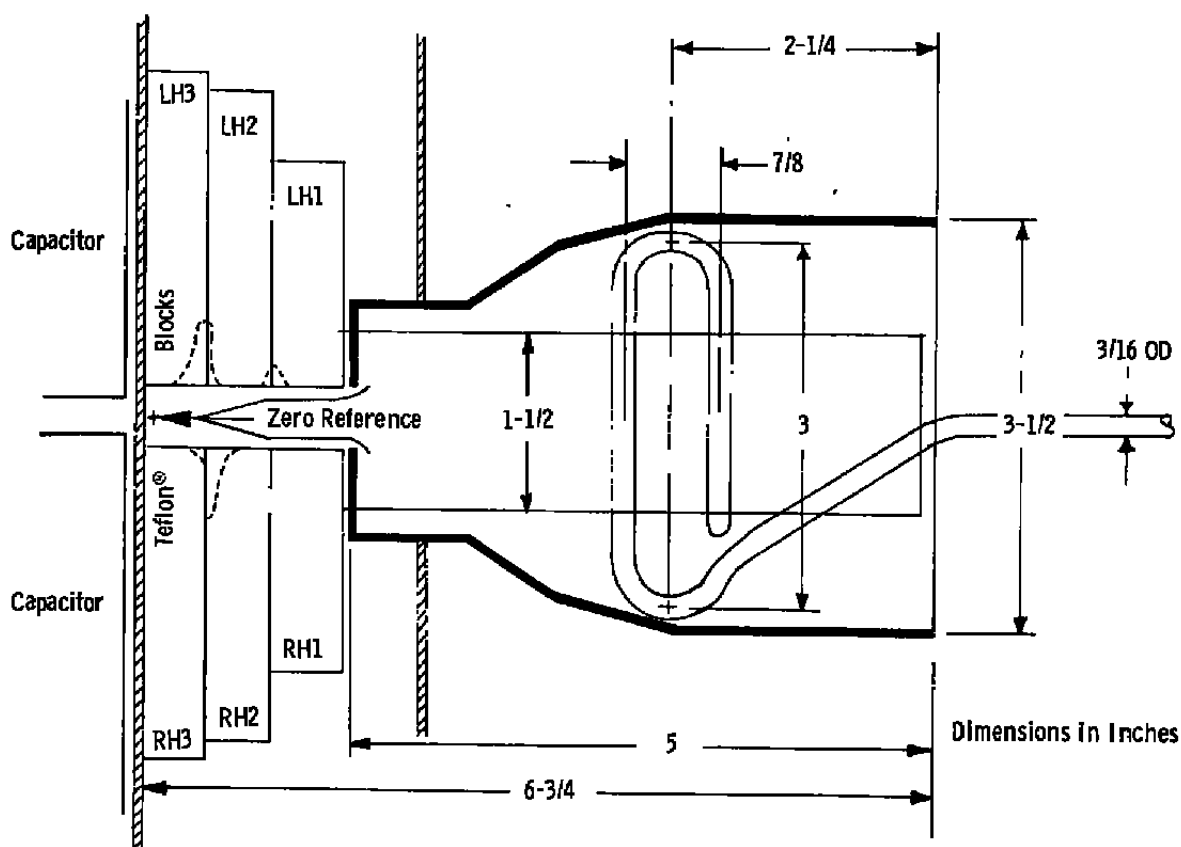
Number of Pulses = 6184

Average Mass per Pulse = 1.16×10^{-3} gm**Table 3. Mass Ablated from Teflon
Fuel Bars (320 μ fd)**

Bar	m, gm	Bar	m, gm
LH1	0.43	RH1	0.35
LH2	1.08	RH2	1.04
LH3	1.67	RH3	1.56

Total Mass Loss = 6.13 gm

Number of Pulses = 3589

Average Mass per Pulse = 1.71×10^{-3} gm**Figure 7. Plan view of current probe in nozzle.**

3.2 MAPPING THE PLASMA CURRENT

A Rogowski coil was fabricated and installed in a glass envelope to be used to measure the current flowing in the plasma as it traveled down the electrodes. The probe is shown pictorially in Fig. 8, and its dimensions are presented in Fig. 7. The current probe was calibrated using the same technique as was used to calibrate the engine current coil. In this calibration the glass-covered coil was looped over the cathode of the engine. The probe was installed in the test chamber at the end of a 7-ft sting arm, and the far end of the sting was secured to the X-Y traversing mechanism in the test chamber. This permitted the probe to be remotely positioned at various locations in the plasma.

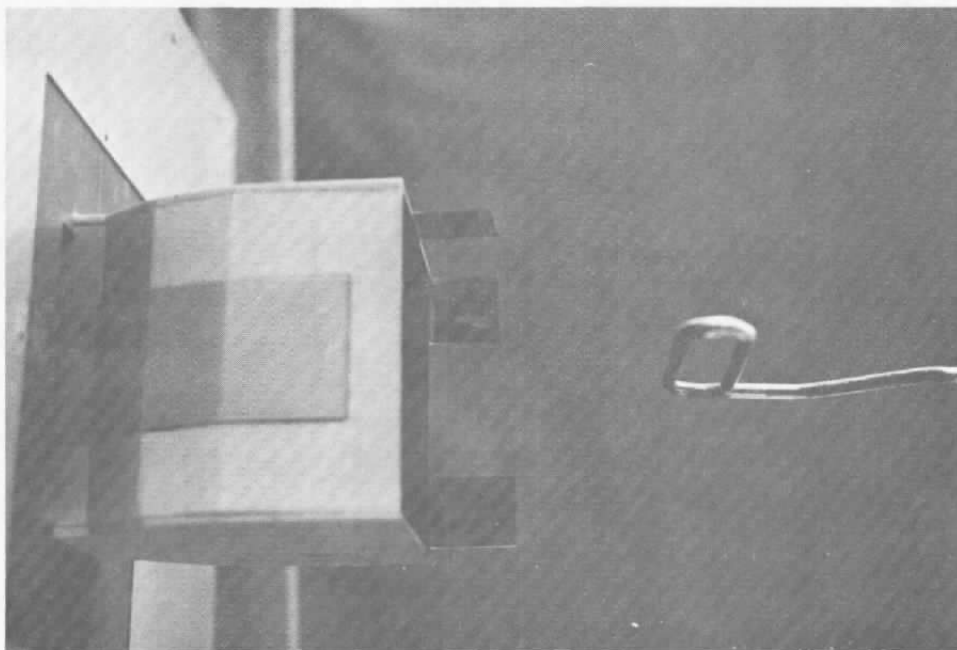
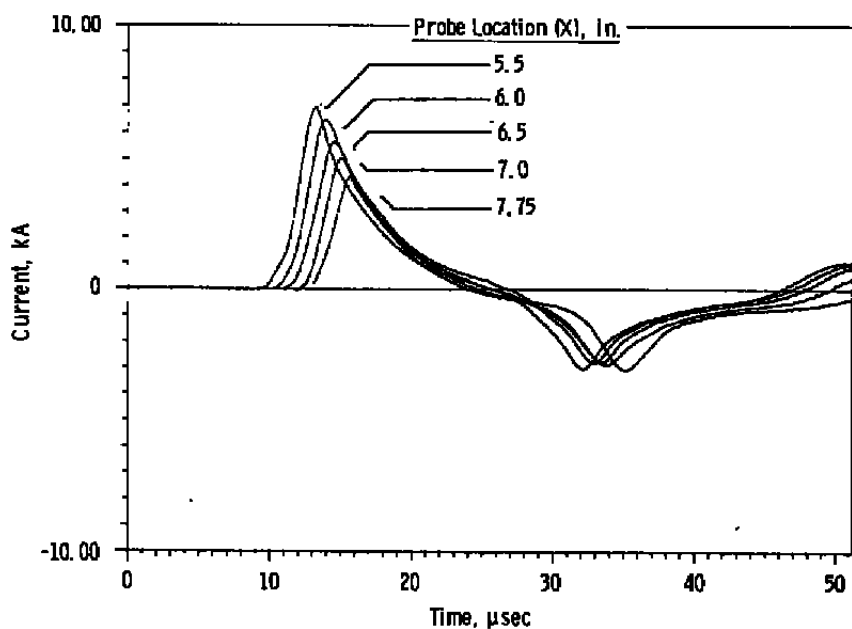


Figure 8. Photograph of current probe in nozzle.

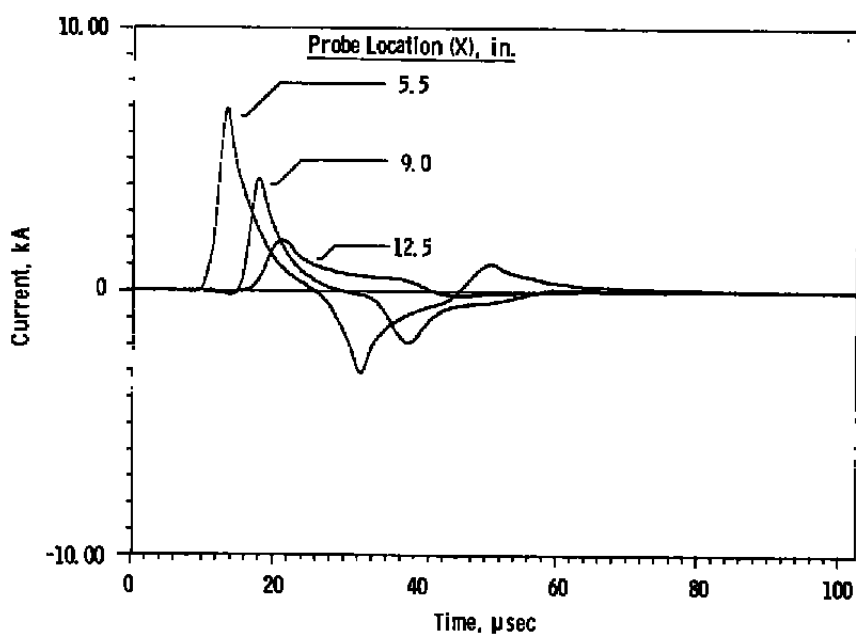
The data are presented in Fig. 9. All of the dimensions are referenced to the backwall in the Teflon section of the engine and are measured to the center of the current loop.

The three distinct plasmoids are quite evident in the probe response at the 5.5-in. location. Data from the current probe were used to calculate the average axial velocity of the plasma current as it passed out of the engine. These velocity data are presented in Fig. 10 and

show the maximum velocity to occur outside of the nozzle. The perturbation at the exit plane of the nozzle is possibly associated with the attachment of the plasma discharge at the end of the anode, as is seen in the high-speed photographs presented in Section 3.4.5.

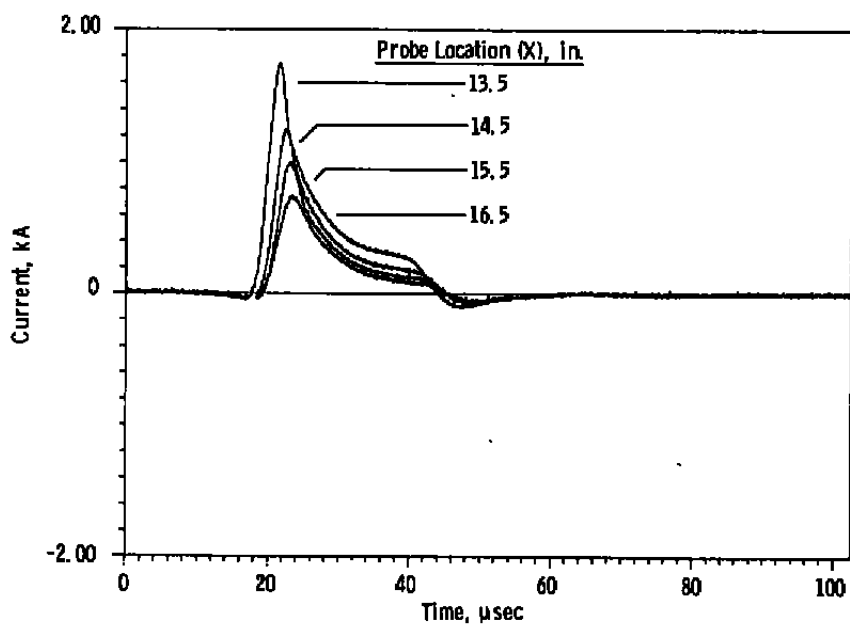


a. Probe at 5.5, 6.0, 6.5, 7.0, and 7.75 in.



b. Probe at 5.5, 9.0, and 12.5 in.

Figure 9. Axial current probe.



c. Probe at 13.5, 14.5, 15.5, and 16.5 in.
Figure 9. Concluded.

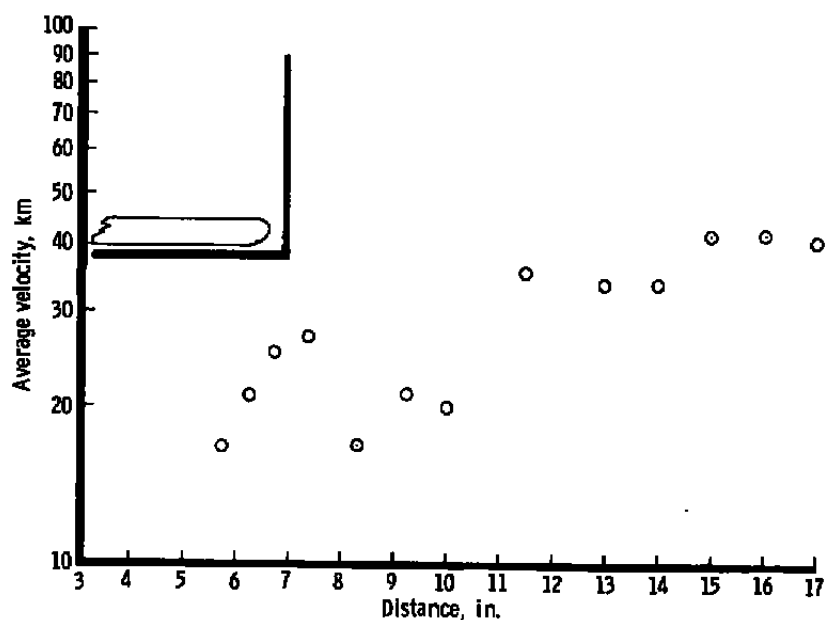


Figure 10. Axial velocity of plasma current.

3.3 MAPPING THE MAGNETIC FIELDS

A small magnetic field probe was constructed and housed in a glass sting. The coil consisted of a single layer of 15 turns of 40 gage enameled copper wire wound with an effective diameter of 2.5 mm. This coil was soldered to a length of miniature coaxial cable and inserted in a 5-mm OD glass tube which had been sealed and blown to a hemispherical shape at the far end. The complete probe assembly was mounted on the X-Y traversing mechanism in the test cell and oriented so that the axis of the coil was horizontal between the engine electrodes.

An integrating network was used with the coil. This consisted of a 10,050- Ω resistor and a 0.53- μ fd capacitor (both values were measured). The frequency response of the probe is determined by the time constant

$$\tau = \frac{L}{R}$$

where L is the inductance of the coil and R is the resistive load.

For a given coil,

$$L = Fn^2r, \mu H$$

where

$$\begin{aligned} r &= \text{effective radius, cm,} \\ n &= \text{number of turns, and} \\ F &= \text{coil factor} \sim r/\ell. \end{aligned}$$

For this coil the form factor, F, was 0.029 (Ref. 2). The time constant for this coil was

$$\tau = 8 \times 10^{-11} \text{ sec}$$

which is more than adequate to follow the 25-kHz ringing frequency of the engine discharge.

When an integrating circuit is used on the output from the coil, then

$$V_i = nA \frac{dB}{dt}$$

becomes

$$V_o = \frac{nA}{RC} B$$

where

V = volts, v

A = effective area of coil, m^2

R = resistive load, Ω

C = capacitance, μfd

B = magnetic field, Tesla

The calibration factor determined for this coil was 7.2 Teslas/volt.

Magnetic probes which are used in strong electric fields can pick up an additional signal due to capacitive coupling (Ref. 3). One solution is to shield the probe using a cage of wires. However, this shield can result in a deterioration of the response time of the coil. The need for shielding was investigated by using the coil in the engine pulse and then rotating it 180 deg and re-recording the signal. The electrostatic component, if present, would not invert and thus would have been detectable. It was determined that shielding was not required for these tests.

The data acquired by the probe for the engine fitted with both size capacitors are presented in the following figures. Figure 11 compares the magnetic fields at an axial station

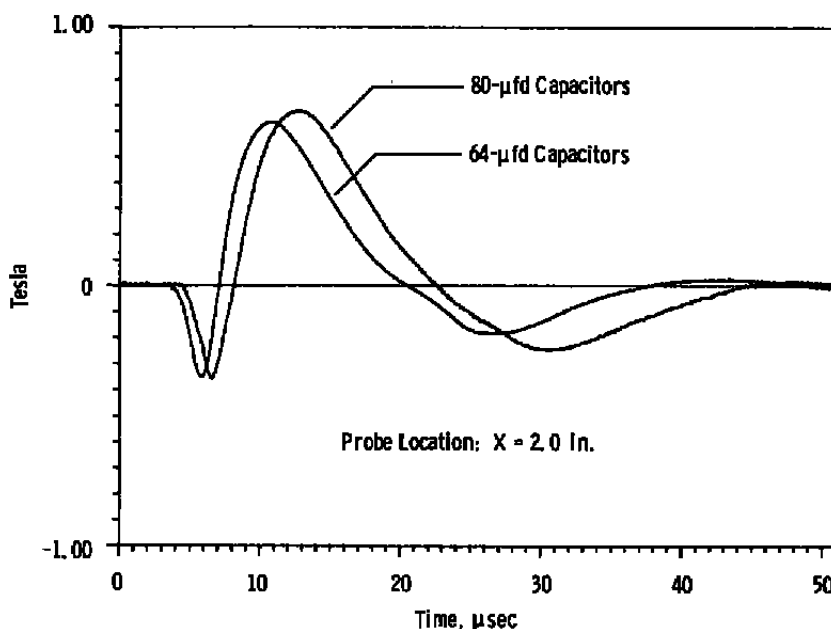
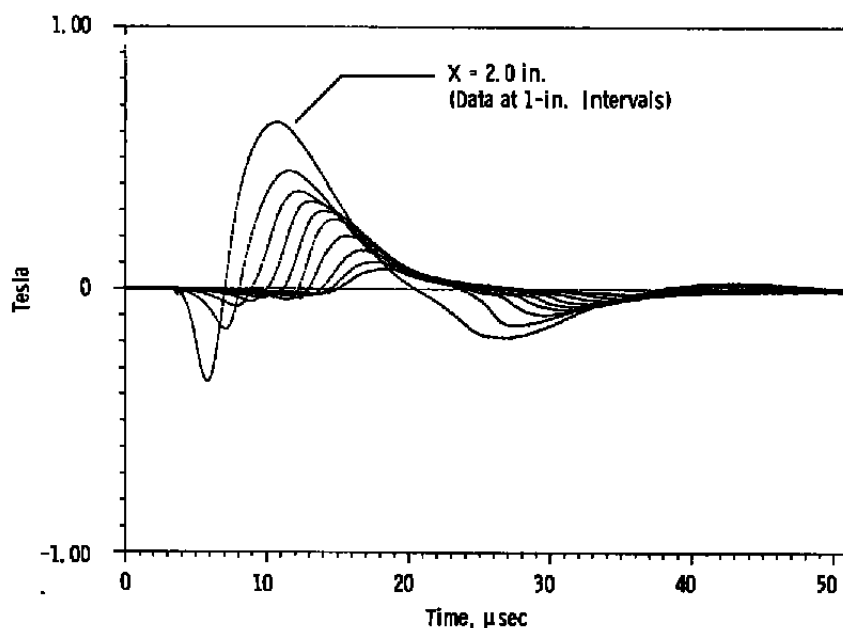


Figure 11. Magnetic probe, X-axis (comparison of capacitors).

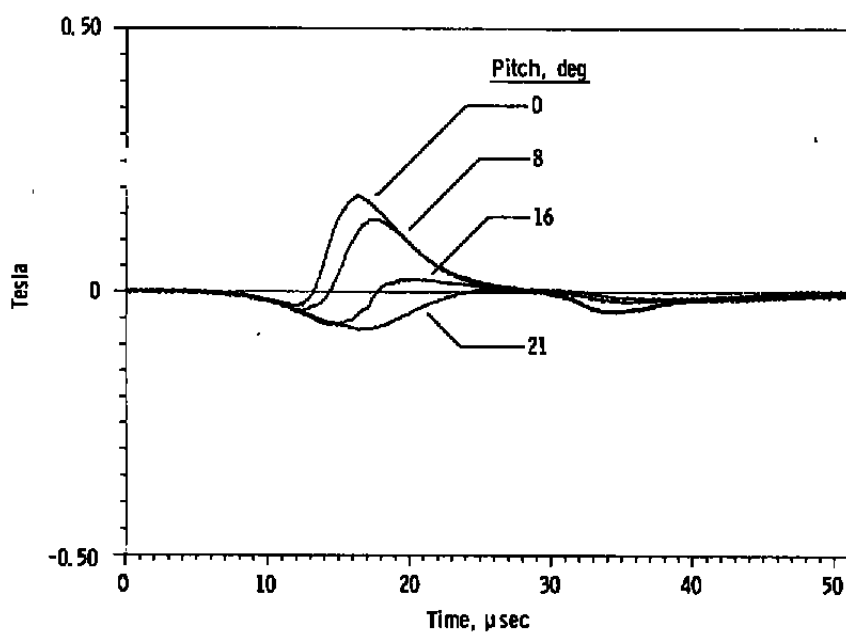
$X = 2$ in. for each engine configuration. The more intense but delayed peak with the $80\text{-}\mu\text{fd}$ capacitors is in agreement with the observations of the current discharge cycles presented previously. It is also interesting to note the slight deformation in the leading edge of the second pulse when the engine was configured with the $64\text{-}\mu\text{fd}$ capacitors. This also is directly comparable to a similar perturbation observed in the discharge data. Figures 12a, b, and c present axial and radial magnetic probe data for the engine with the small capacitors. Only radial data at $X = 8.0$ in. were taken with this configuration. Figures 13a through g and i contain both axial and radial data for the engine with the $80\text{-}\mu\text{fd}$ capacitors. The Y-axis plots represent the engine rotating about the Y-axis and located as shown in Fig. 14. This, therefore, is a vertical profile of the fields at the exit of the engine. The Z-axis data, Figs. 15a and b, are a horizontal scan across the exit plane of the engine. The pivoting Z-axis is through the same point as the Y-axis previously noted in Fig. 14. All X distances are measured with the engine in its 0-deg position, and of course the probe stays fixed at this location while the engine is pivoted.

General observations from these data are that the fields are not symmetric in the vertical plane but are so in the horizontal plane. With the probe at the rear wall of the discharge cavity the absence of a negative precursor indicates that the arc is striking downstream of the probe coil. With the coil at $X = 0.5$ in. the arc starts upstream of the probe with the magnetic field reversing as the current passes the probe at $t = 6.5\text{ }\mu\text{sec}$, or $2.5\text{ }\mu\text{sec}$ into the discharge cycle.

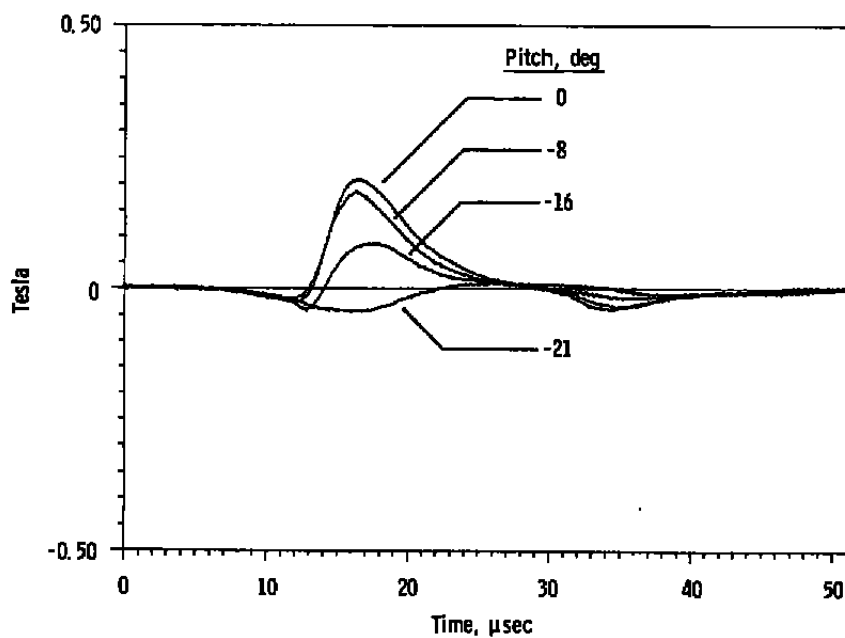


a. Data at 1-in. intervals

Figure 12. Magnetic probe, X-axis ($64\text{-}\mu\text{fd}$ capacitors).

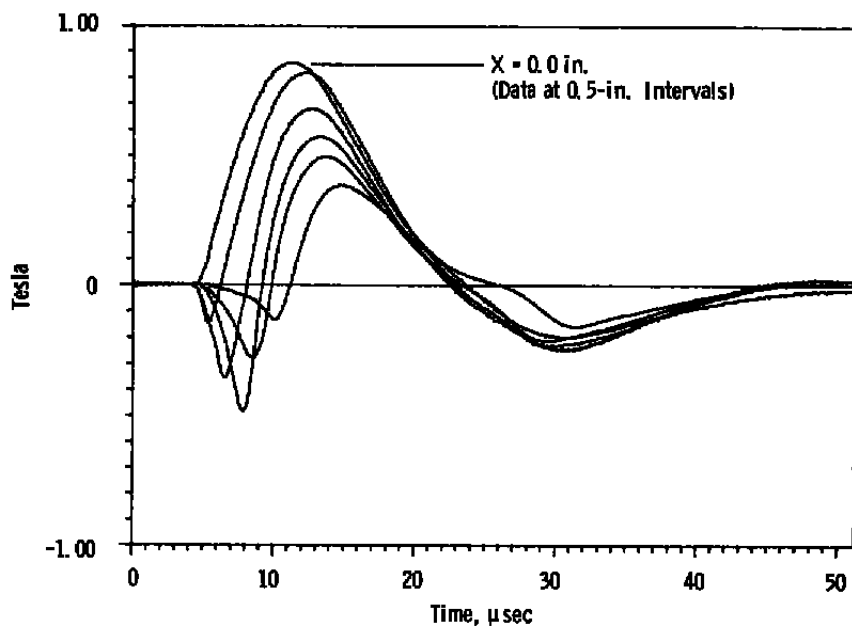


b. $X = 8$ in., pitch above centerline

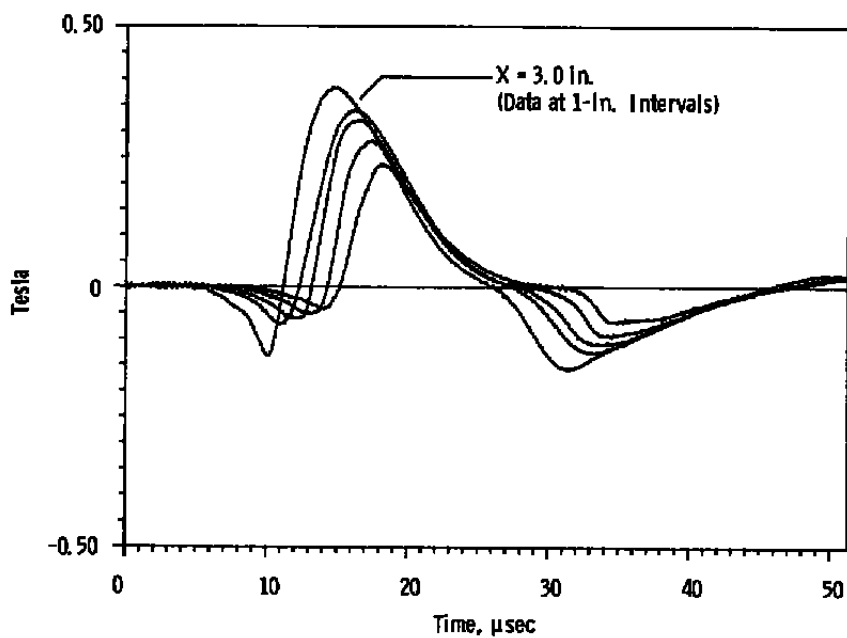


c. $X = 8$ in., pitch below centerline

Figure 12. Concluded.

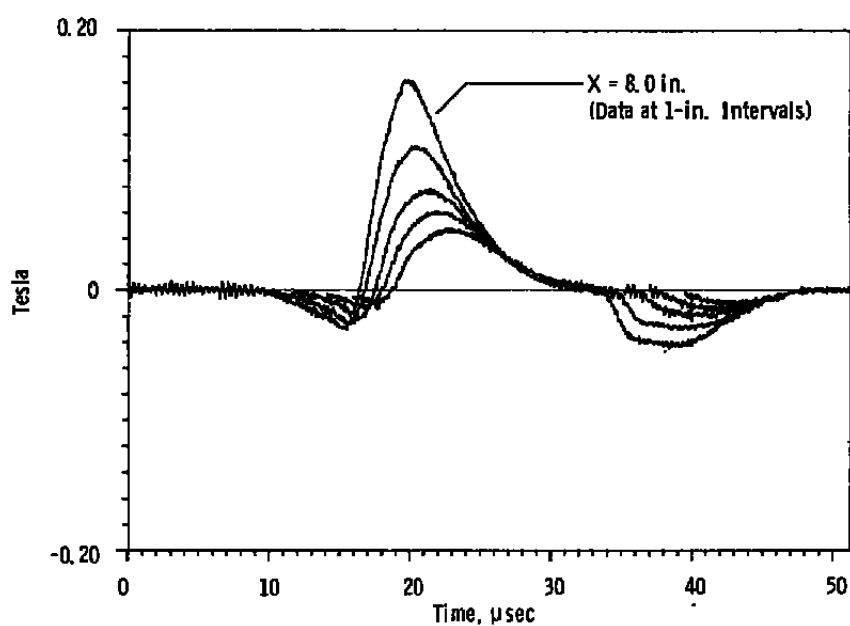


a. X-axis, $X = 0$, data at 0.5-in. intervals

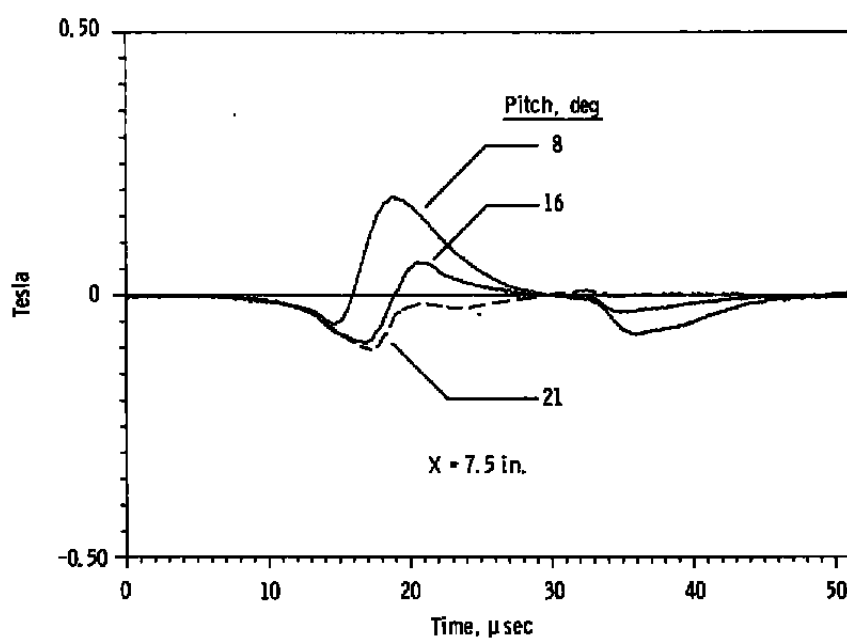


b. X-axis, $X = 3.0$ in., data at 1-in. intervals

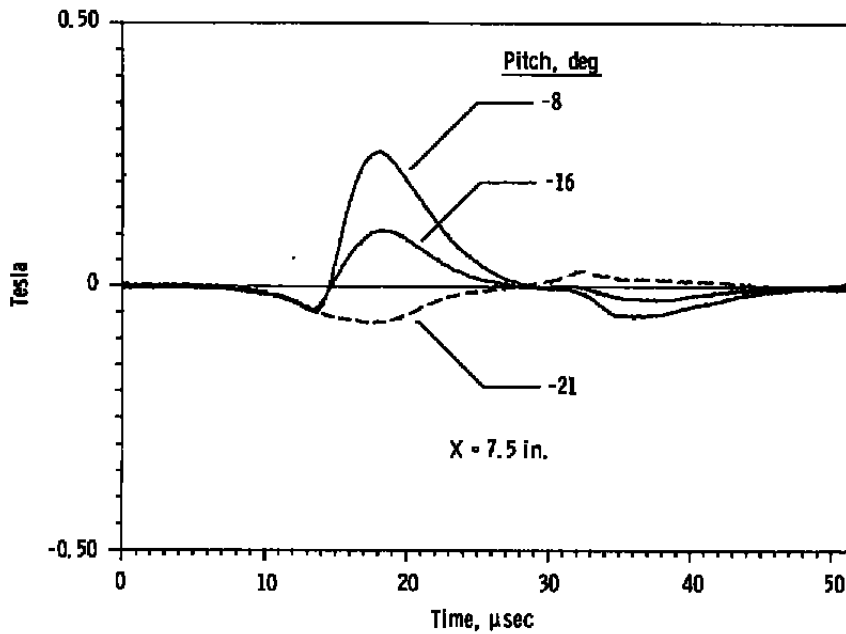
Figure 13. Magnetic probe (80- μ fd capacitors)



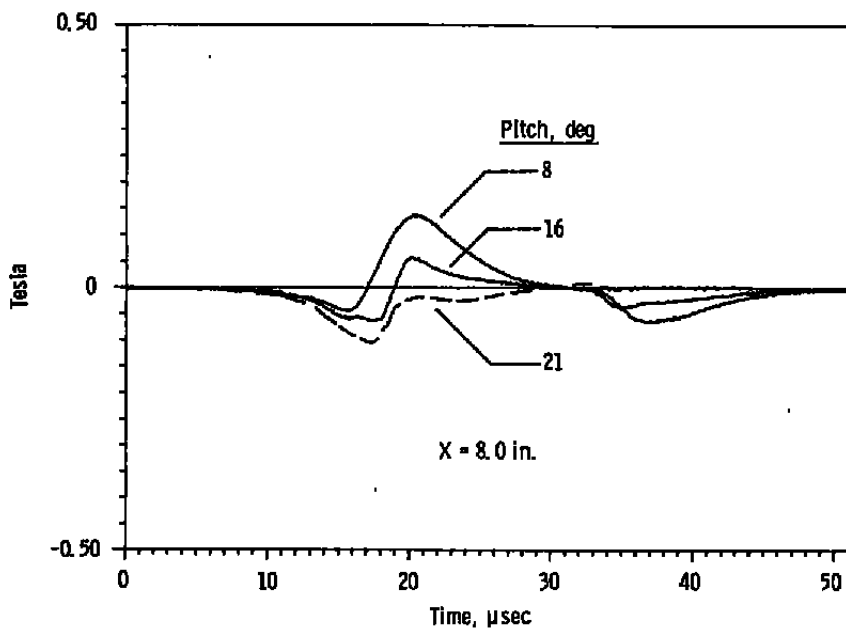
c. X-axis, $X = 8.0$ in., data at 1-in. intervals



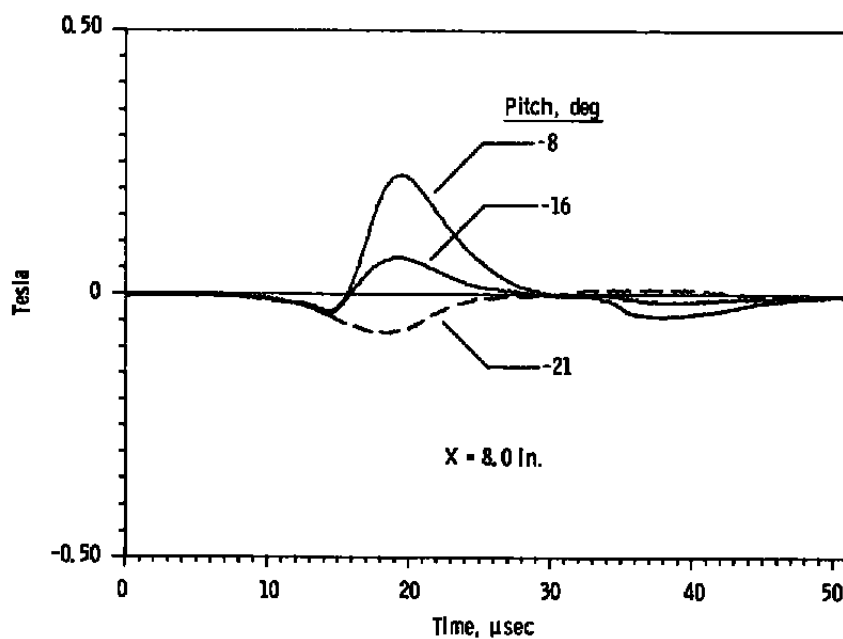
d. Y-axis, $X = 7.5$ in., pitch above centerline
Figure 13. Continued.



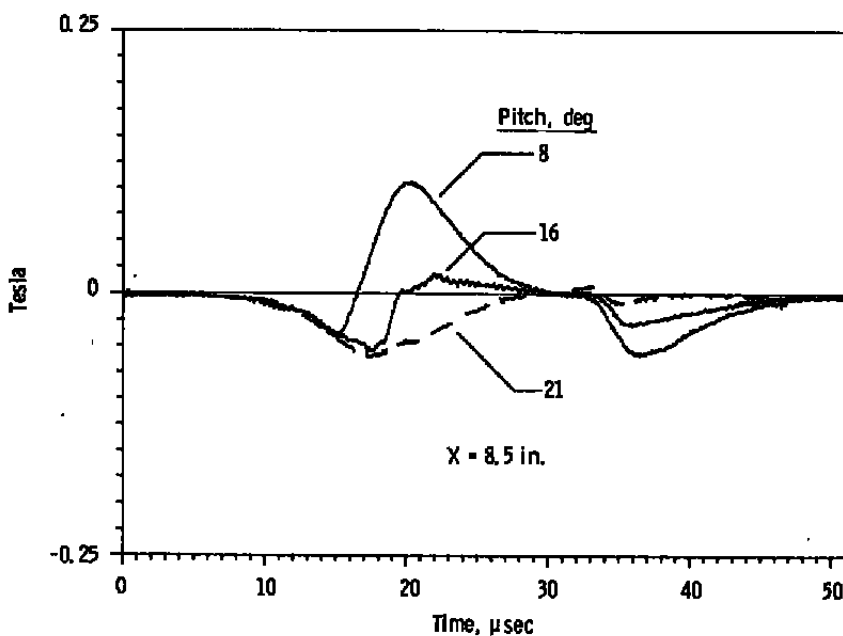
e. Y-axis, $X = 7.5 \text{ in.}$, pitch below centerline



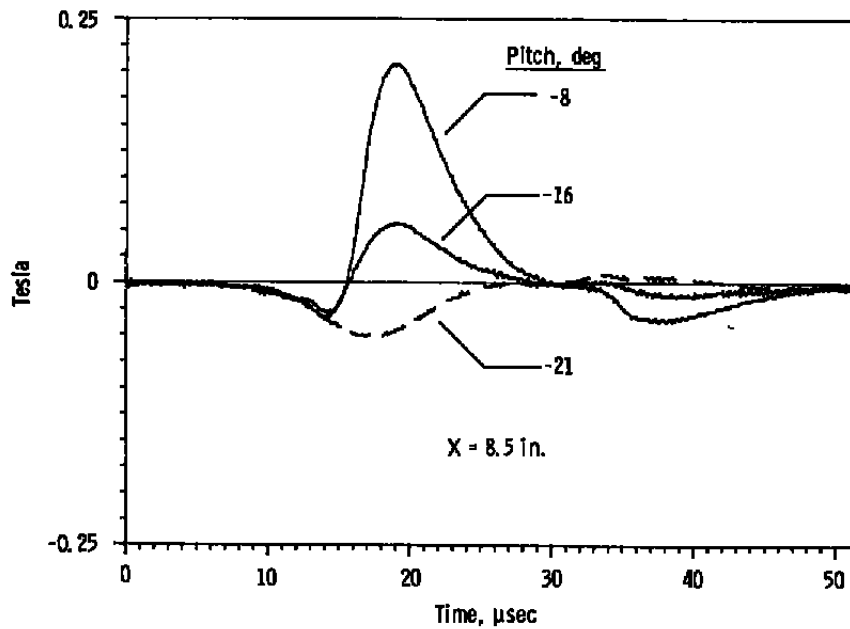
f. Y-axis, $X = 8.0 \text{ in.}$, data above centerline
Figure 13. Continued.



g. Y-axis, $X = 8.0 \text{ in.}$, pitch below centerline



h. Y-axis, $X = 8.5 \text{ in.}$, pitch above centerline
Figure 13. Continued.



i. Y-axis, X = 8.5 in., pitch below centerline
Figure 13. Concluded.

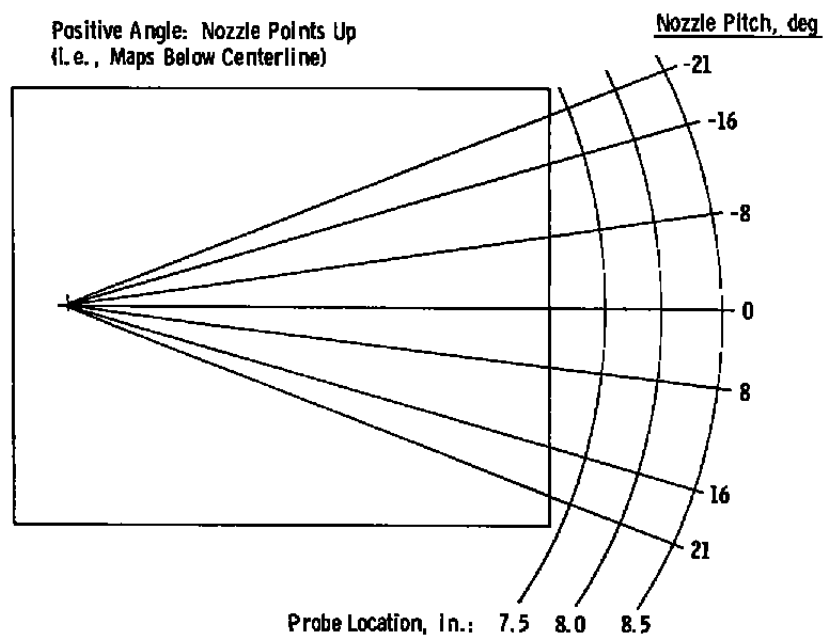
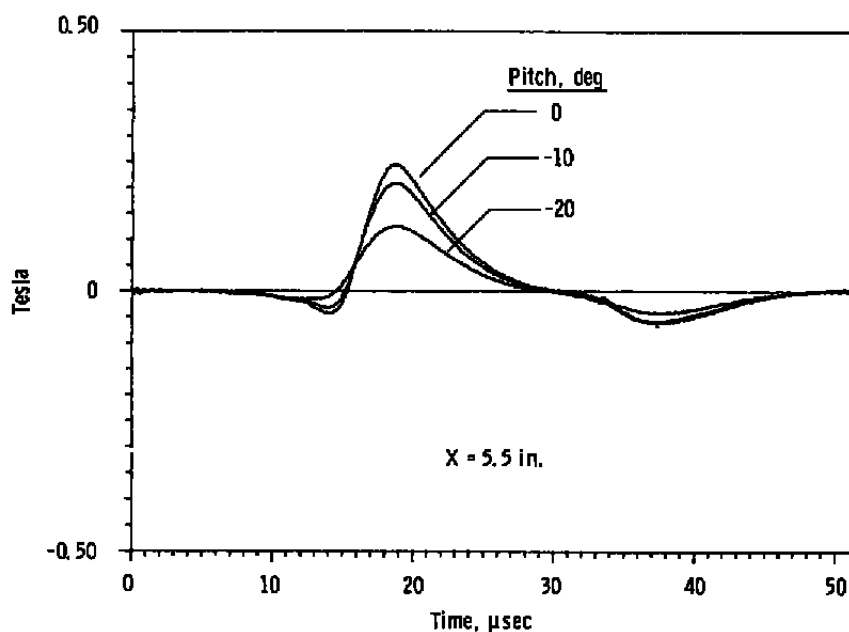
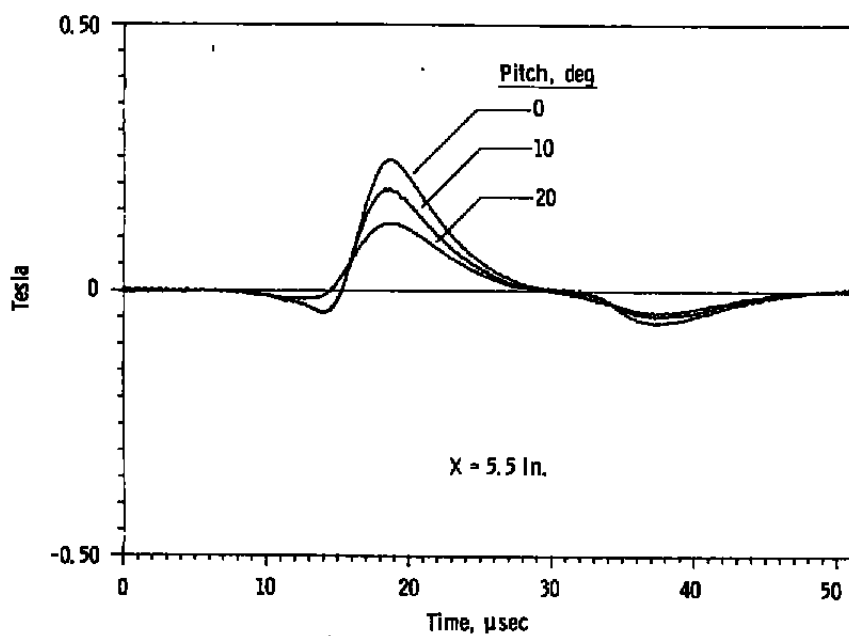


Figure 14. Magnetic probe location.



a. Pitch below centerline



b. Pitch above centerline

Figure 15. Magnetic probe (Z-axis).

3.4 PHOTONS PRODUCED BY THE ENGINE

During a single pulse the engine emits a mixture of photons, electrons, ions, gas molecules, and particles. Each of these interact with surfaces in the test chamber, producing a secondary set of photons, electrons, ions, gases, and possible particles. This section presents the results of experiments that were performed to try to identify primary engine products compared to chamber-induced contributions.

3.4.1 Electromagnetic Emissions

The engine discharge is accompanied by an intense pulse of photons with a significant portion of this electromagnetic energy contained in the ultraviolet wavelengths. During this test sequence data were acquired to document both the spatial spectra at the exit plane of the nozzle and a temporal record of some of the more intense wavelengths. In addition to the primary photons there is a secondary emission when the high-energy plasma collides with any chamber surface. This was recorded by a photomultiplier located downstream of the engine and viewing the end wall of the test cell (1.32 m downstream of engine nozzle exit). As can be seen in Fig. 16, the detector recorded first the reflection of the initial flash of the engine pulse and then the secondary photons as the plasma arrived at the wall. The delay and flight distance can be used to calculate a plasma main pulse velocity of 40,000 sec. A more

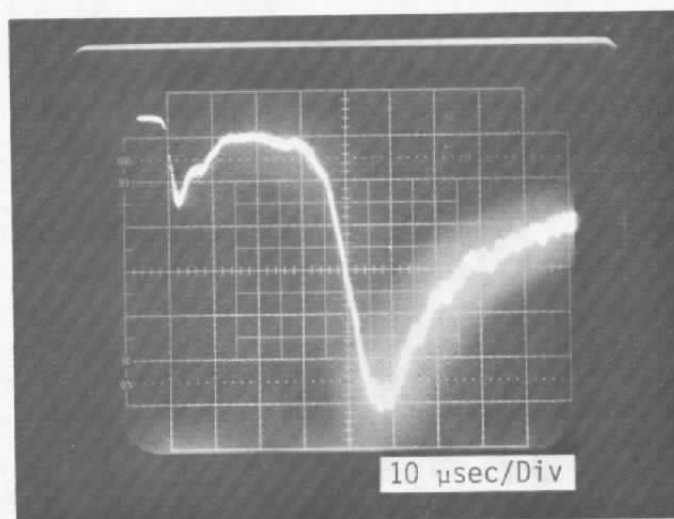


Figure 16. Photomultiplier detector.

visual demonstration of this secondary emission is seen as the plasma hits the baffle assembly which was installed downstream of the engine in a later test (Fig. 17).

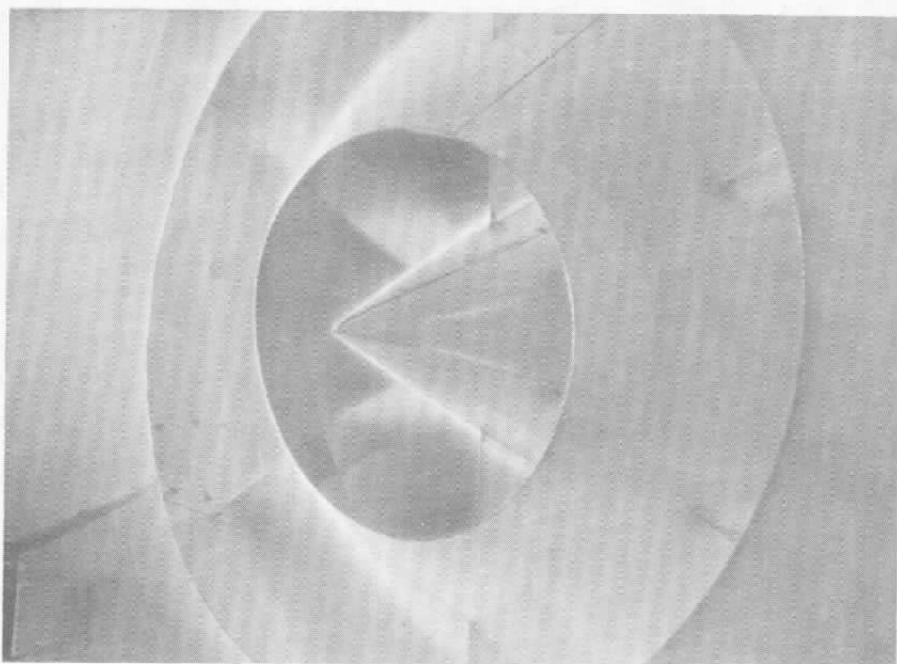


Figure 17. Plasma passing through baffle.

3.4.2 VUV/UV Spectroscopic Survey

Previous visible and near ultraviolet spectroscopic measurements of the pulsed plasma plume are discussed in Ref. 1. For the VUV measurements, a 0.5-m Seya-Namioka vacuum ultraviolet spectrometer (McPherson Model 235) was fitted to the research chamber without use of collection optics (see Fig. 18). For the spectral measurements, a 512-element silicon diode array detector, preceded by a microchannel intensifier tube, was adapted to the focal plane of the spectrometer. A terphenyl scintillator wafer was laminated to the intensifier input fiber optic for conversion of ultraviolet to visible radiation. With a 600-line/mm tripartite concave grating, blazed at 1500 \AA and having a reciprocal dispersion of 36 \AA/mm , the spectrometer recorded a spectral segment of 700 \AA at a resolution of 7 \AA . The shortest wavelength observable was 800 \AA , and although the detector was sensitive to visible radiation, the longest wavelength reported in this survey was near 4000 \AA .

To observe different emission regions, the spherical aberration of the spectrometer was used as an advantage. Spherical aberration caused the field of view of the spectrometer to assume a horizontal slot geometry so that at the plume location the field was 7 mm high and 30 mm wide. This field was fixed; however, the pulse plasma thruster could be pitched to achieve the different field locations shown in Fig. 19.

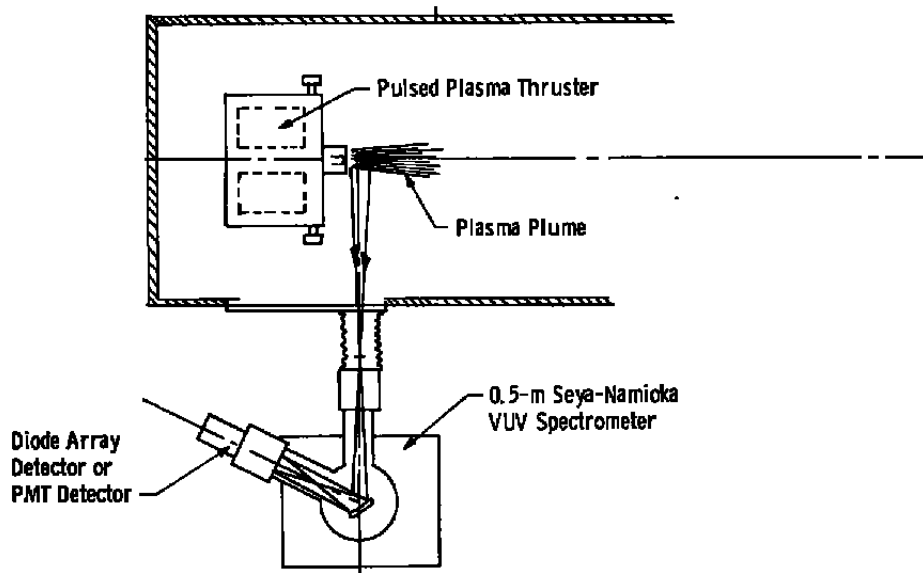


Figure 18. Plan view of spectrometer installation.

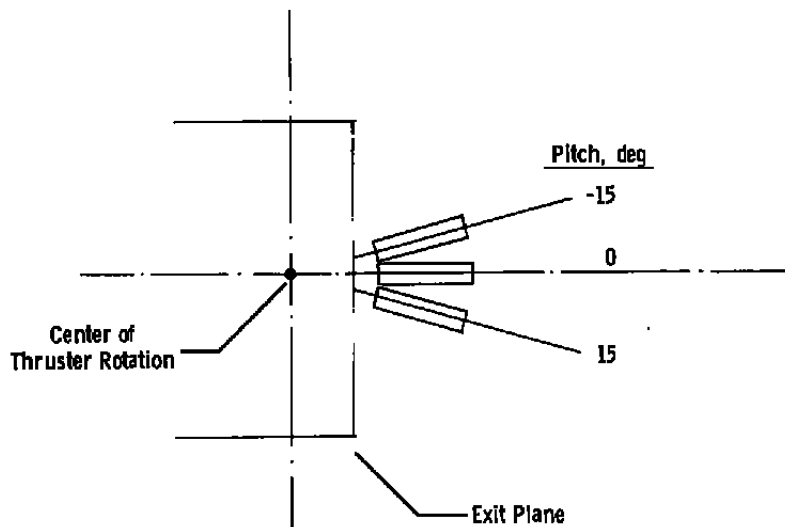


Figure 19. Field of view of spectrometer.

A complete VUV/UV spectrum was recorded by incrementing the spectrometer at 500-Å intervals and co-adding ten thruster plume emissions for each interval. The composite spectrum for the three spatial locations observed is shown in Fig. 20. Table 4 gives a listing of the species identified from the VUV/UV spectra as well as several unidentified spectral lines. Carbon atoms and ions are the predominant emitting species observed in the spectral survey. Single-ionized aluminum, copper, and fluorine are also present and originate from

Table 4. Species and Associated Wavelengths Identified from the VUV/UV Spectral Survey

Wavelength, Angstroms	Species	Wavelength, Angstroms	Species
858	C ⁺	1762	Al ⁺
904	C ⁺	1931	C
977	C ⁺⁺	2133	Cu ⁺ 2136
1010	C ⁺	2194	Al (Cu ⁺ 2192)
1037	C ⁺	2244	Cu ⁺ 2247
1066	C ⁺	2297	C ⁺⁺
1176	C ⁺⁺	2354	1176 C ⁺⁺ , Order II
1247	C ⁺⁺	2511	C ⁺
1278	C	2646	1324 C ⁺ , Order II
1302	C ⁺ ?	2670	1336 C ⁺ , Order II
1324	C ⁺	2747	C ⁺
1336	C ⁺	2837	C ⁺
1361	?	2993	C ⁺
1397	?	3059	F ⁺
1432	C	3096	1549 C ⁺⁺⁺ , Order II
1463	C	3123	1561 C, Order II
1549	C ⁺⁺⁺	3315	1657 C, Order II
1561	C	3441	?
1595	Cu ⁺ ?	3502	F ⁺
1605	?	3518	?
1628	?	3539	F ⁺
1641	Cu ⁺ ?	3590	C ⁺
1657	C	3601	F/F ⁺
1667	Al ⁺	3849	F ⁺
1686	Cu ⁺ ?	3876	C ⁺
1706	Cu ⁺ ?	3901	Al ⁺ ?
1723	Al ⁺	3920	C ⁺
1746	Cu ⁺ ?	3972,74	F ⁺ , C ⁺

for the +15-deg position, indicating much higher temperatures near the anode region of the plasma plume.

The survey spectrum shows that the plasma is quite complex but also demonstrates that emission VUV spectroscopy of improved spatial, spectral, and temporal quality would be a very useful diagnostic technique for measuring temperatures and species concentrations.

3.4.3 Temporal VUV Measurements

The temporal VUV measurements were performed using the same Seya-Namioka spectrometer, although a solar blind photomultiplier tube (PMT) was used as the detector. The PMT was an EMR Photoelectric 541G-09-18 having a CsTe photocathode sensitive to wavelengths between 1100 and 2200 Å. For the few measurements below 1100 Å and 2200 Å an EMI 9635 B PMT, preceded by a sodium salicylate-coated window, was employed. PMT signals were recorded by a Nicolet Model 204 digital oscilloscope.

Six prominent emitting species were observed for the spatial locations shown in Fig. 21. The species and the peak signal levels are listed in Table 5 with the pitch angle of the thruster identifying the spatial location observed.

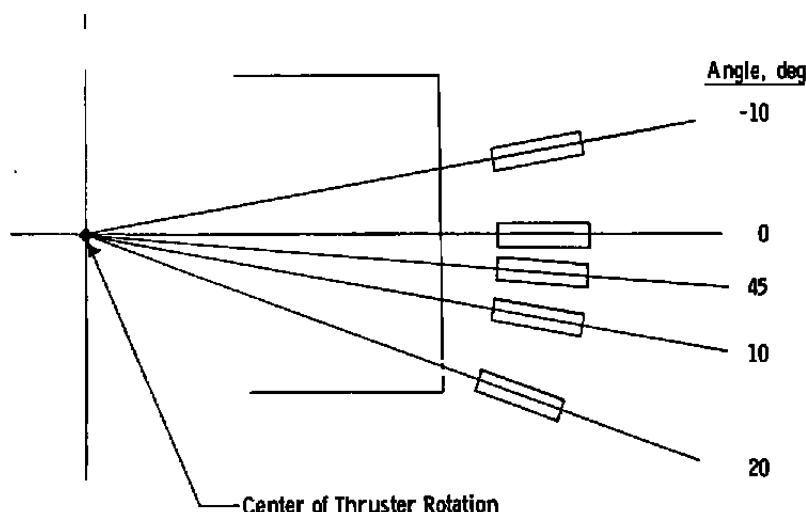


Figure 21. Spatial regions observed during temporal VUV/UV measurements.

All of the species observed can be characterized as emitting in two pulses nominally 10 μsec in duration and separated by roughly 20 μsec . The peak radiation occurs at $t = +15 \mu\text{sec}$, about 5 μsec after the peak current, due to the time required for the plasma to exit the thruster and enter the field of view of the VUV spectrometer. Differences in intensities range up to two orders of magnitude. Absolute calibration of the spectrographic system was beyond the scope of the survey; nevertheless, it is instructive to compute order-of-magnitude intensities and compare these values to the VUV solar irradiance. It should be noted that strong VUV in some circumstances could be considered a contamination source since VUV irradiation is a common method of promoting polymerization of volatile condensable materials.

Table 5. Species Observed in VUV/UV Temporal Measurements

Specie	Wavelength, Å	Engine Pitch Angle, deg	Signal Level, 1st Peak	Signal Level, 2nd Peak
A1+	1762	4.5	5.00	---
A1+	1762	10.0	8.00	0.80
A1+	1762	20.0	4.00	1.00
A1+	1762	-10.0	4.50	0.80
C	1278	4.5	0.70	0.02
C	1278	10.0	0.60	0.04
C	1278	20.0	0.10	0.04
C	1278	-10.0	0.60	0.02
C+	858	4.5	0.04	0.01
C+	904	4.5	0.05	0.04
C+	1010	4.5	0.06	0.03
C+	1324	4.5	0.03	0.01
C+	1324	10.0	0.04	0.02
C+	1324	20.0	0.05	0.01
C+	1324	-10.0	0.04	0.01
C++	977	4.5	0.06	0.01
C++	1176	4.5	0.09	0.03
C++	1176	10.0	0.09	0.02
C++	1176	20.0	0.20	0.02
C++	1176	-10.0	0.15	0.02
F+	3502	0.0	0.07	0.02
F+	3849	0.0	0.08	0.03
F+	4025	0.0	0.09	0.02
F+	3502	-10.0	0.08	0.02
H	1216		0.02	0.005

The most intense emission observed was the A1⁺ line at 1762 Å, Fig. 22; however, aluminum is not present in the Teflon fuel, but is a constituent (Al₂O₃) of the ceramic wall located in front of the Teflon blocks. The intensity of this A1⁺ line is calculated from the equation

$$N_{\lambda} = K \frac{S_{\lambda}}{J_{\lambda}}$$

where N_{λ} is the radiance of the plasma for a select spectral line, S_{λ} is the PMT signal, J is the PMT radiant sensitivity (photocathode), and the constant K contains geometric factors,

load resistance, spectrometer efficiency, and PMT gain. For the $A1^+$ peak radiation,

$$N_{1762} = 10^{17} \text{ photons sec}^{-1} - \text{sr}^{-1} - \text{cm}^{-2}$$

is an order-of-magnitude radiance. The associated uncertainty is not greater than a factor of ten and is mainly due to uncertainties in the spectrometer efficiency. For a surface located 1m from the plasma emission the irradiance, assuming an average plasma area of 100 cm^2 , would be $10^{15} \text{ photons sec}^{-1} - \text{cm}^{-2}$. The solar VUV irradiance in a $0.1\text{-}\text{\AA}$ bandpass is $6 \times 10^8 \text{ photons sec}^{-1} - \text{cm}^{-2}$ (Ref. 4). Although the major plasma emission is only $10 \mu\text{sec}$ in duration and contains many fewer lines than the solar VUV flux, the VUV irradiance from the plasma is 10^6 times more intense than the solar VUV flux.

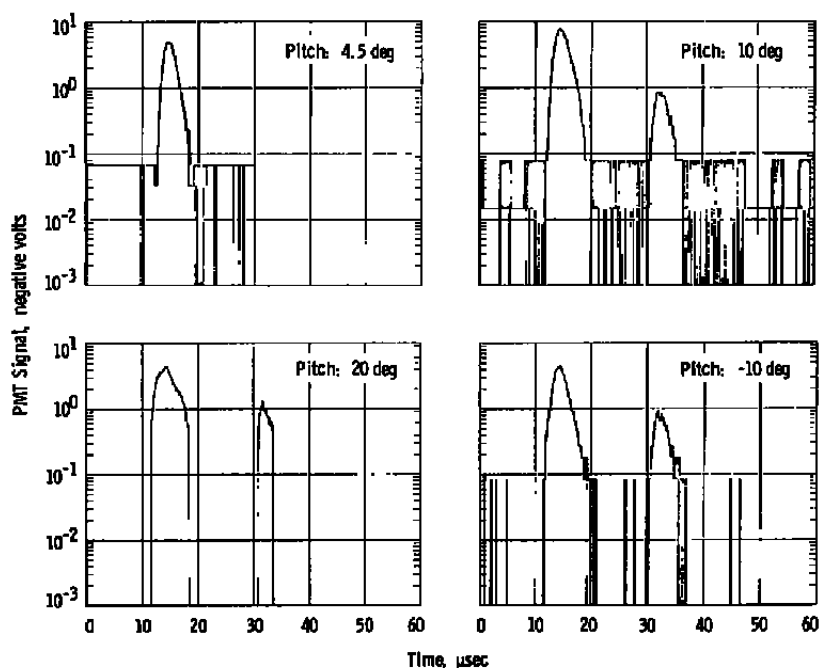


Figure 22. Intensity of $A1^+$ (1762 \AA) radiation versus time.

The radiation of the neutral carbon emission line (1278 \AA), the single-ionized carbon emission line (1324 \AA), and the double-ionized carbon emission line (1176 \AA) is shown as a function of time in Figs. 23, 24, and 25, respectively. Figure 26 shows the emissions of C^+ and C^{++} lines at other wavelengths. Fluorine could not be observed in the VUV since its prominent emission lines are below 800 \AA ; thus, middle UV radiation was recorded as shown in Fig. 27. As is clear in all the temporal emission measurements the radiation emitted is characteristic of the energy discharge in the plasma thruster, that is, two well-defined pulses of radiation. Also, the difference in the intensities of the two VUV pulses is in reasonable agreement with the measured differences in the two current pulses during one thruster firing.

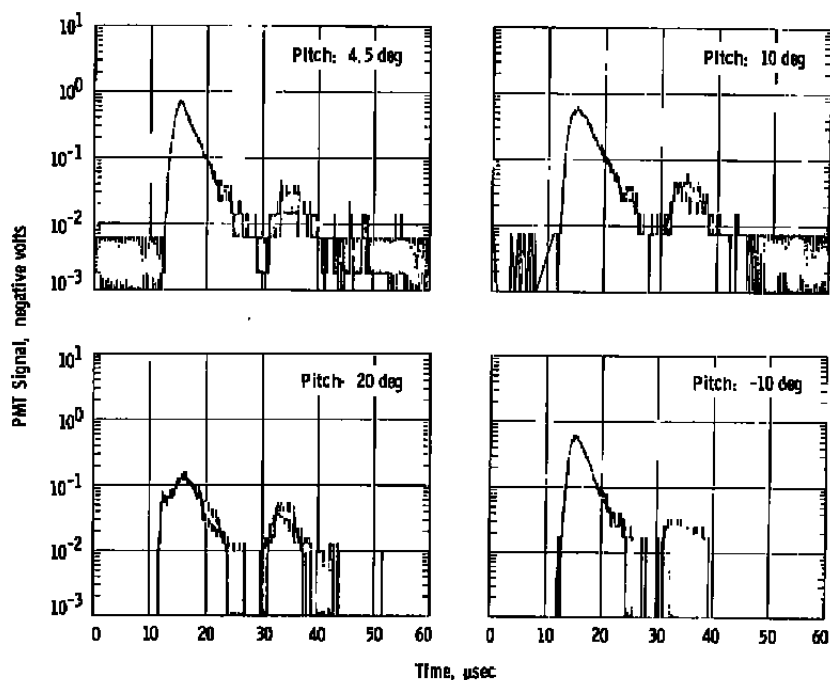


Figure 23. Intensity of C (1278 Å) radiation versus time.

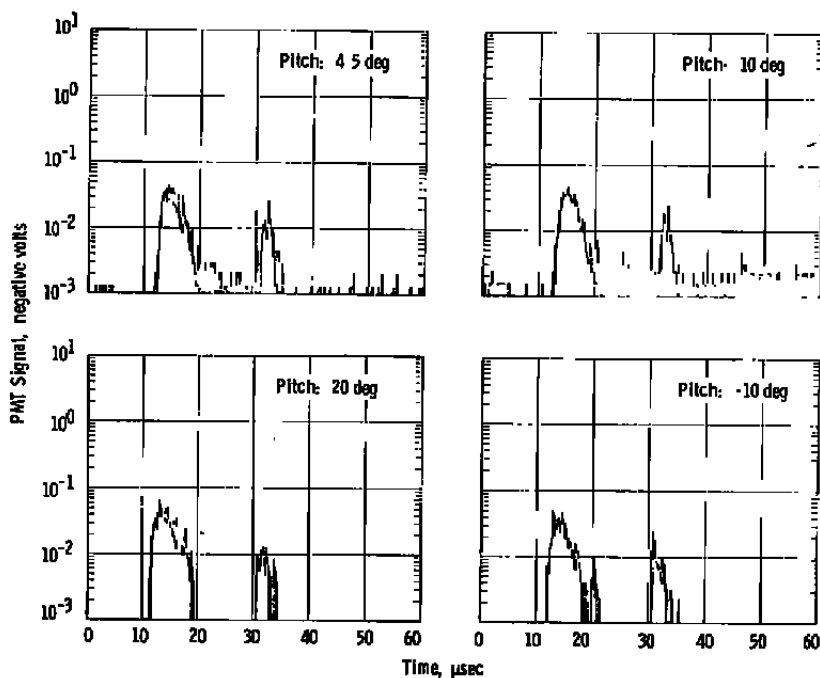


Figure 24. Intensity of C⁺ (1324 Å) radiation versus time.

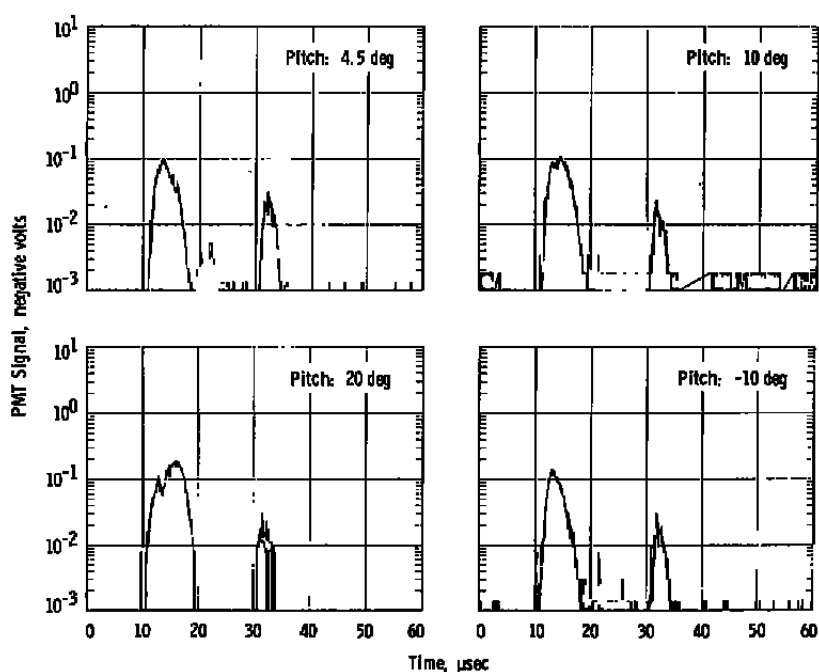


Figure 25. Intensity of C^{++} (1176 Å) radiation versus time.

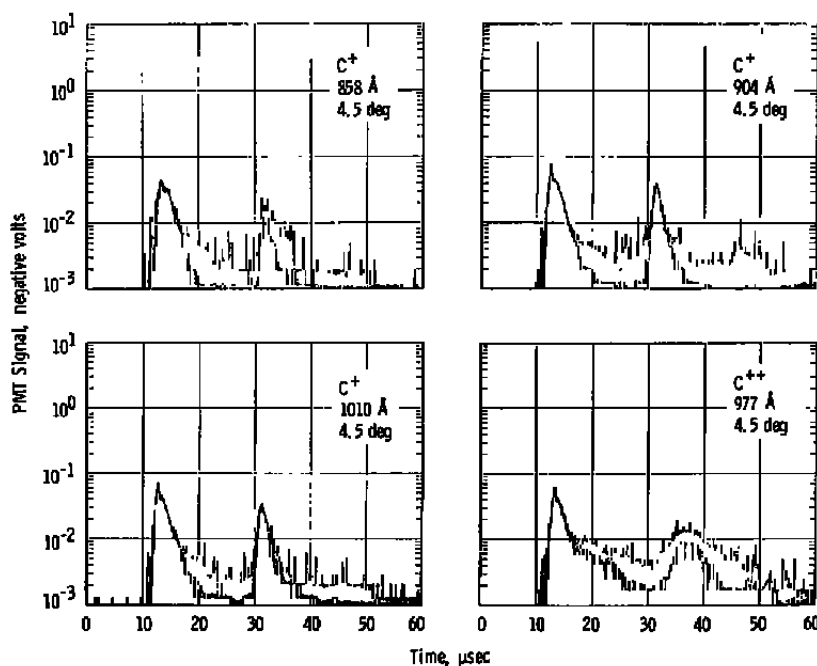


Figure 26. C^+ and C^{++} radiation as a function of time.

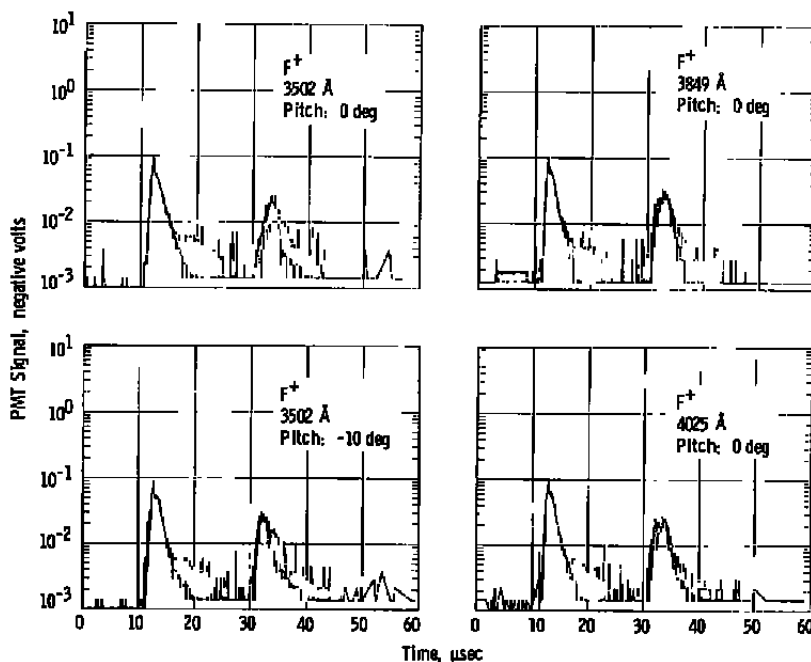


Figure 27. Intensity of F^+ radiation versus time.

Finally, the plasma was monitored for evidence of H and O. The intensity of the hydrogen alpha line at 1216 Å was recorded, as was the oxygen line at 7772 Å. These lines were monitored for the first 50 pulses following two weekend shutdowns of the engine. The data presented in Fig. 28 are not directly comparable to each other since they were taken after different shutdown periods. However, they both demonstrate that the H and O source is rapidly depleted with the first few engine pulses and then reaches a level where further decay is very slow. These data, along with information gained from the mass spectrometer studies, suggest that the H and O emissions are from water vapor absorbed on the inner surfaces of the motor nozzle. The small but continued contribution of H and O emission lines in the spectra is thought to be due to the readsorption of a small amount of H_2O in the time period between engine firings (duty cycle 1 pulse/65 seconds).

3.4.4 Doppler Shift Velocity Measurements

Ablated atoms and ions from the pulsed plasma engine were known to have velocities of tens of kilometers per second. Calculations indicated that the light emission Doppler shifts associated with these velocities should be large enough to measure with a 0.75-m focal length spectrometer fitted with an intensified diode array detector. It was realized, however, that the results would not necessarily be indicative of the terminal velocity, but would represent a velocity at which the line's spectral intensity is near a maximum. This was because no

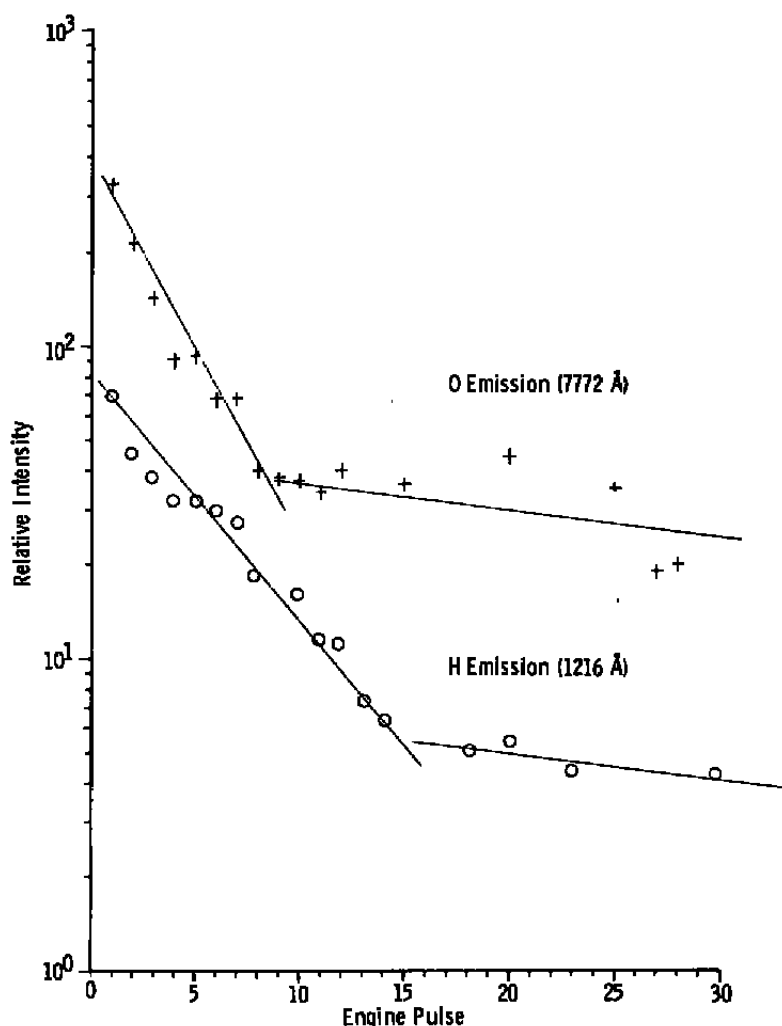


Figure 28. Decay of O and H radiation as a function of engine pulse number.

temporal resolution of the pulse was possible with this detector; all the pulse's light would be collected within the 5-msec exposure time.

Eight spectral lines were chosen for measurement on the basis of their spectral isolation, intensity, and proximity to lines of similar quality from either a mercury or an argon calibration light source. Included were five fluorine, one singly ionized fluorine, and two singly ionized carbon lines.

A spherical mirror was positioned to focus light from the arc region onto the entrance slit, and this arrangement is shown in Fig. 29 as the 0-deg position. Also shown are the spectrometer's other two positions at 90 deg and approximately 80 deg, neither of which

used collection optics. The spectra were displayed by a multichannel analyzer and recorded on floppy disk. Pulses were co-added when necessary to obtain sufficient intensity. Calibration spectra were recorded after each plasma line acquisition. All spectra were recorded in second order to enhance the method's sensitivity; the reciprocal dispersion ($\text{\AA}/\text{channel}$) was reduced to less than half due to an inherent decrease with increasing wavelength. A spectrum in which an argon calibration line was co-added with a plasma fluorine line is shown in Fig. 30.

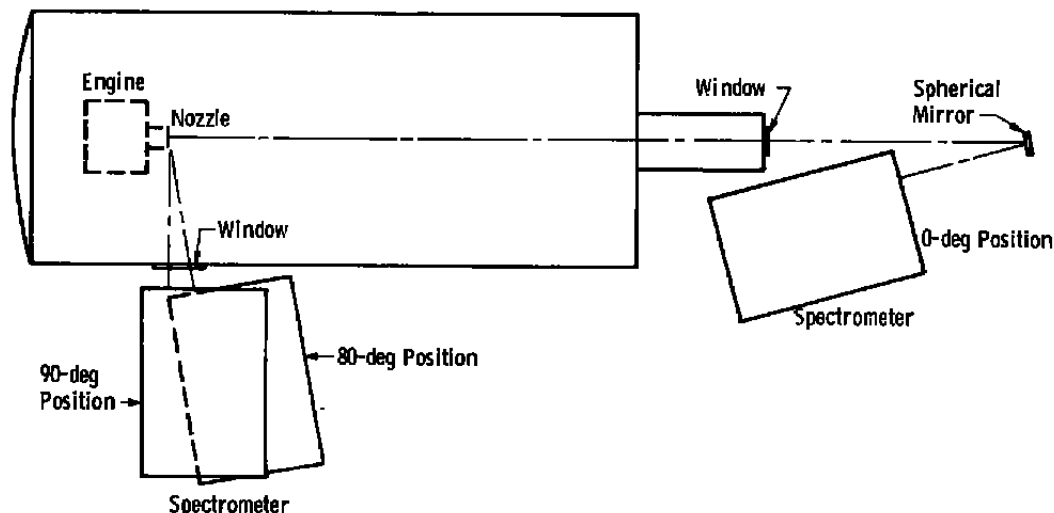


Figure 29. Spectrometer positions for the doppler shift measurements.

At low velocities, the velocity V in kilometers per second may be calculated from the Doppler shift by the following:

$$V = \frac{c\Delta\lambda}{\lambda_0}$$

where c is the velocity of light (2.998×10^5 km/sec), $\Delta\lambda$ is the wavelength shift in \AA , and λ_0 is the wavelength of the spectral line at zero velocity in \AA . After each plasma and calibration line was plotted in magnified form by means of an X-Y recorder directly from the multi-channel analyzer, the channel numbers of the peak positions were carefully determined. Then previously determined values of the reciprocal dispersion, Fig. 31, were used to calculate the wavelength shifts from the zero velocity channel positions.

Individual and average measurement results are presented in Table 6. Spectral line intensity ratios between the 0-deg and the 80- and 90-deg positions were also calculated, and these are presented in Table 7. Upon examination of the results in the tables, it can be concluded that:

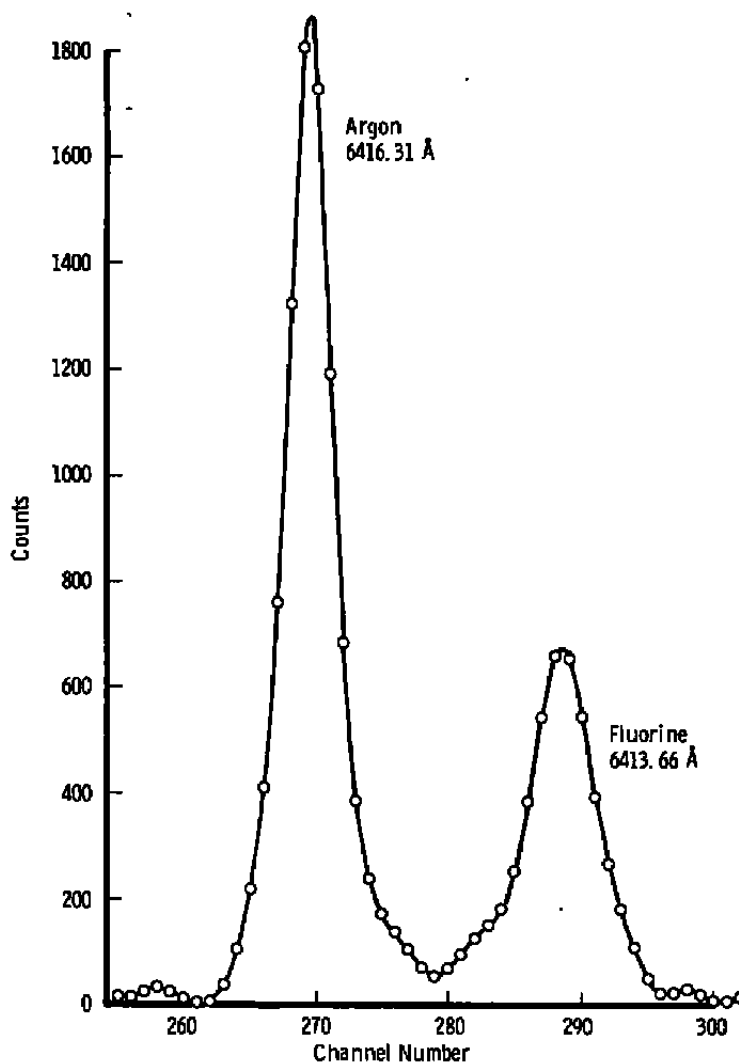


Figure 30. Co-added F and A spectral lines in second order.

1. The velocities are less than the maximum plasma velocity, implying that the terminal velocities were not attained at the mean time of light emission.
2. The carbon ion velocity is greater than the fluorine velocity. However, the velocity ratio is not consistent with an equipartition of energy.
3. Nearly all the ionic emission occurs near the arc, and little occurs outside the nozzle.
4. Neutral fluorine emission extends to outside the nozzle. This is verified by the dominant red emission seen in color photographs of the plasma plume.

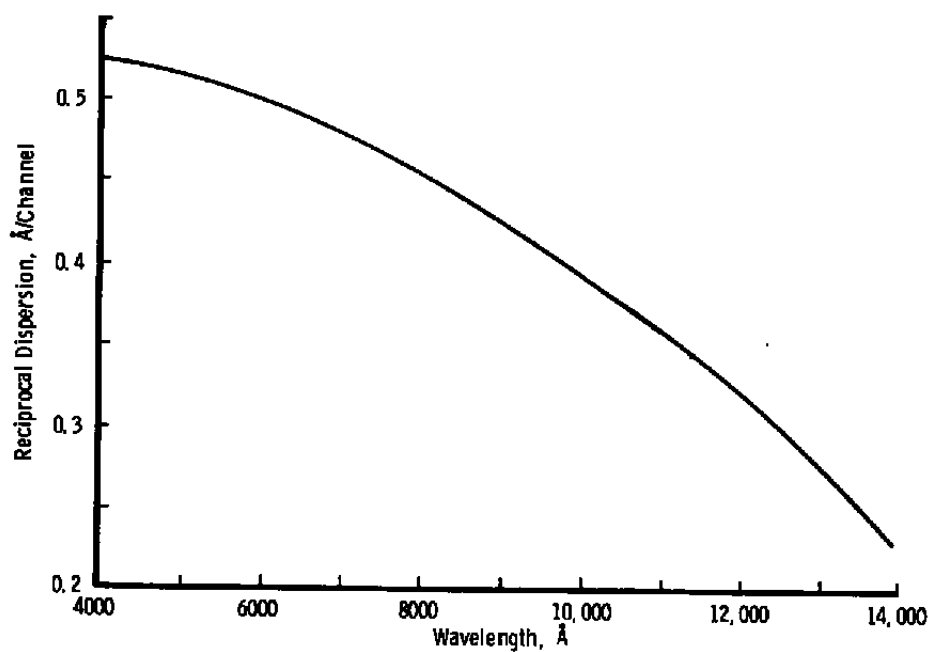


Figure 31. Reciprocal dispersion versus wavelength.

Table 6. Velocity Measurement Results

Species	Wavelength (l), Å	Velocity, km/sec		
		Spectrometer Position, deg		
		0	80	90
F	6413.66	9	4	3
	6690.47	15	7	2
	6773.97	11	4	2
	6870.22	11	5	2
	6966.35	16	6	1
F ⁺	4933.25	12	13	---
C ⁺	5648.08	22	10	---
	6098.62	29	13	---
Average Values:				
	F	12	5	2
	F ⁺	12	13	---
	C ⁺	25	11	---

Table 7. Ratio of Line Intensities

Species	$\frac{I(80 \text{ deg})}{I(0 \text{ deg})}$	$\frac{I(90 \text{ deg})}{I(0 \text{ deg})}$
F	1/8	1/60
C ⁺	1/30	1/160
F ⁺	1/40	1/170

This attempt at Doppler shift measurement revealed trends but could be improved by temporally resolving the individual emissions. This would require a fast, gateable detector or possibly, for the more intense lines, a Kerr cell shutter on the spectrometer.

3.4.5 High-Speed Photograph of the Plasma

The engine pulse sequencer was used with a Kerr cell shutter to obtain photographs of the plasma traveling down the electrodes and leaving the engine. The sequencer was set up so that the D channel timer started on the engine trigger pulse and the Kerr cell was tripped by the D channel output. The setting of the D channel thus established the delay time for the photograph. The D channel in this configuration had a resolution of 100 nsec and could be programmed to delay up to a maximum of 100 msec.

Two pulse-forming networks were used with the Kerr cell during these tests. The first gave a shutter open time of 1 μ sec and the other gave 100 nsec. Trial exposures were made and it was found that an exposure of 1 μ sec at f/2 with ASA 400 film (40-mm lens) was adequate to record both the first and second plasmoids as they exited the engine nozzle. The 100-nsec exposure at f/2 provided more detailed photographs of the structure in the first plasmoid, but there was not sufficient light to photograph the second plasmoid.

After the sequencing and exposure problems were solved, a series of photographs was taken of the engine pulsing with a fixed delay. This series of photographs indicated that the engine pulses were very repeatable even to the reproduction of fine detail in the structure observed in the plasma. It was therefore considered feasible to obtain a time-sequenced history of the plasma leaving the engine by photographing successive plasma pulses with the D-channel progressively delayed. This technique provided photographs of the first and second plasmoids leaving the engine. This photo sequence, shown in Fig. 32, was taken with the engine fitted with the 64- μ fd capacitors. Each exposure was for 1 μ sec with an aperture of f/2. When the negatives were printed, an optimum exposure and color balance was set for the frame at 18- μ sec delay. All other frames were printed at these settings. This resulted in

some overexposure and loss of detail in the earlier part of the discharge but gives a better feeling for the relative intensity of the various phases of the discharge. The glass probe visible in these photographs houses the small magnetic search coil. After the changeover of the capacitors the nozzle of the engine was removed and a glass nozzle was installed. Figure 33 presents photographs of the plasma accelerating down the electrodes. These photographs were taken with a 100-nsec exposure of $f/2$. They show more detail in the plasma structure since there is less blur due to the higher shutter speed, and they are also nearer to optimum exposure for this part of the discharge. There was insufficient light to photograph either the first plasmoid after it had left the engine or the formation of the second plasmoid with this exposure. A final set of photographs of the engine firing without any nozzle is presented in Fig. 34. This sequence again used the 100-nsec shutter to capture as much detail as possible. Of main interest in this sequence are the hot spots forming on the anode. The first spots are seen at 24 μsec , near the throat of the engine. By 33 μsec they are well distributed over the entire anode. This period of time coincides with the current reversal in the engine discharge (Fig. 5). Along with the hot spots on the anode there is also a significant event occurring at the cathode at 33 μsec . This type of burst, which also has been observed at the cathode, occurs on an intermittent basis. Further comment on the possible cause of this phenomenon is presented in Section 3.5.

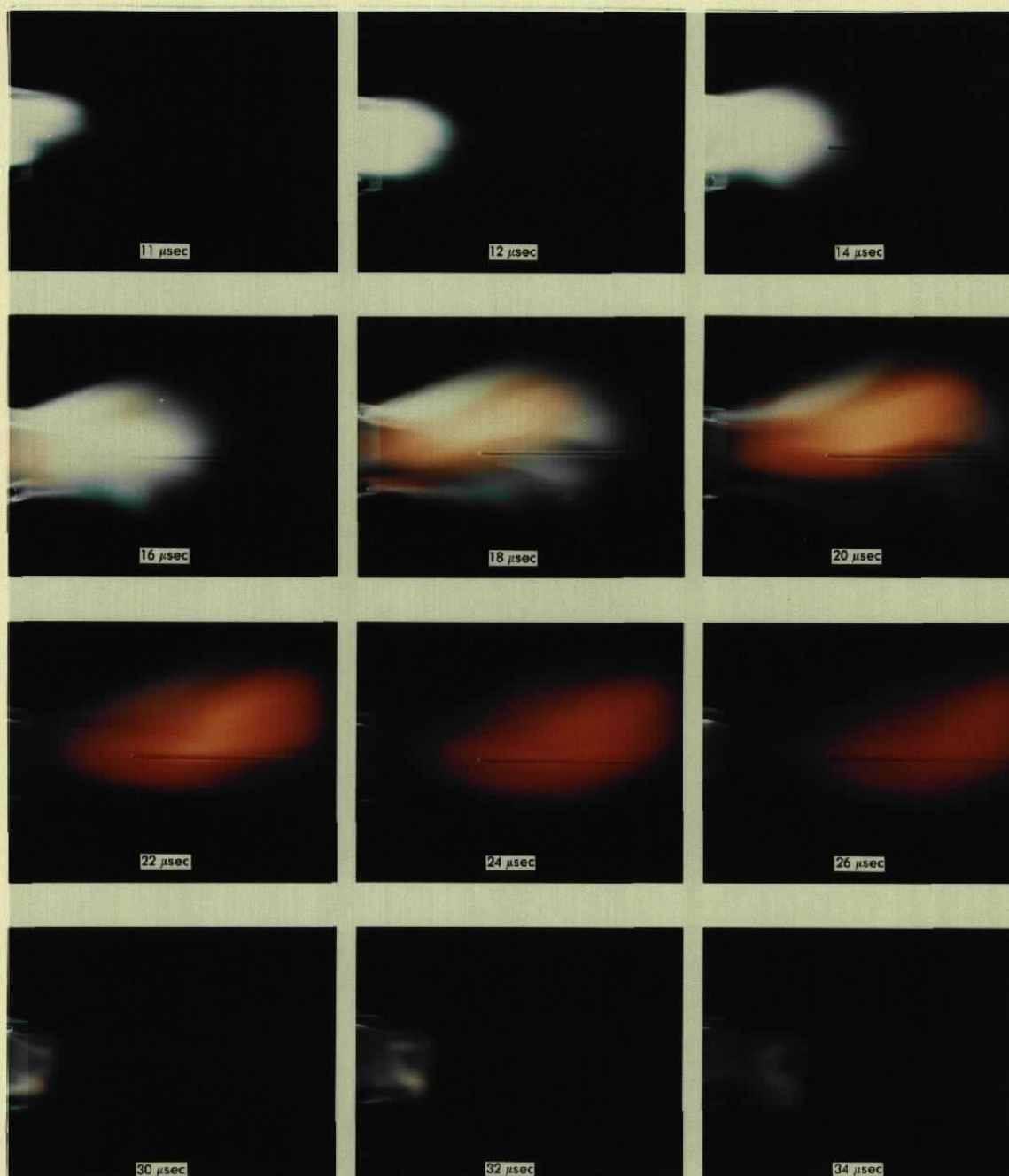


Figure 32. Photographs of plasma (side view).

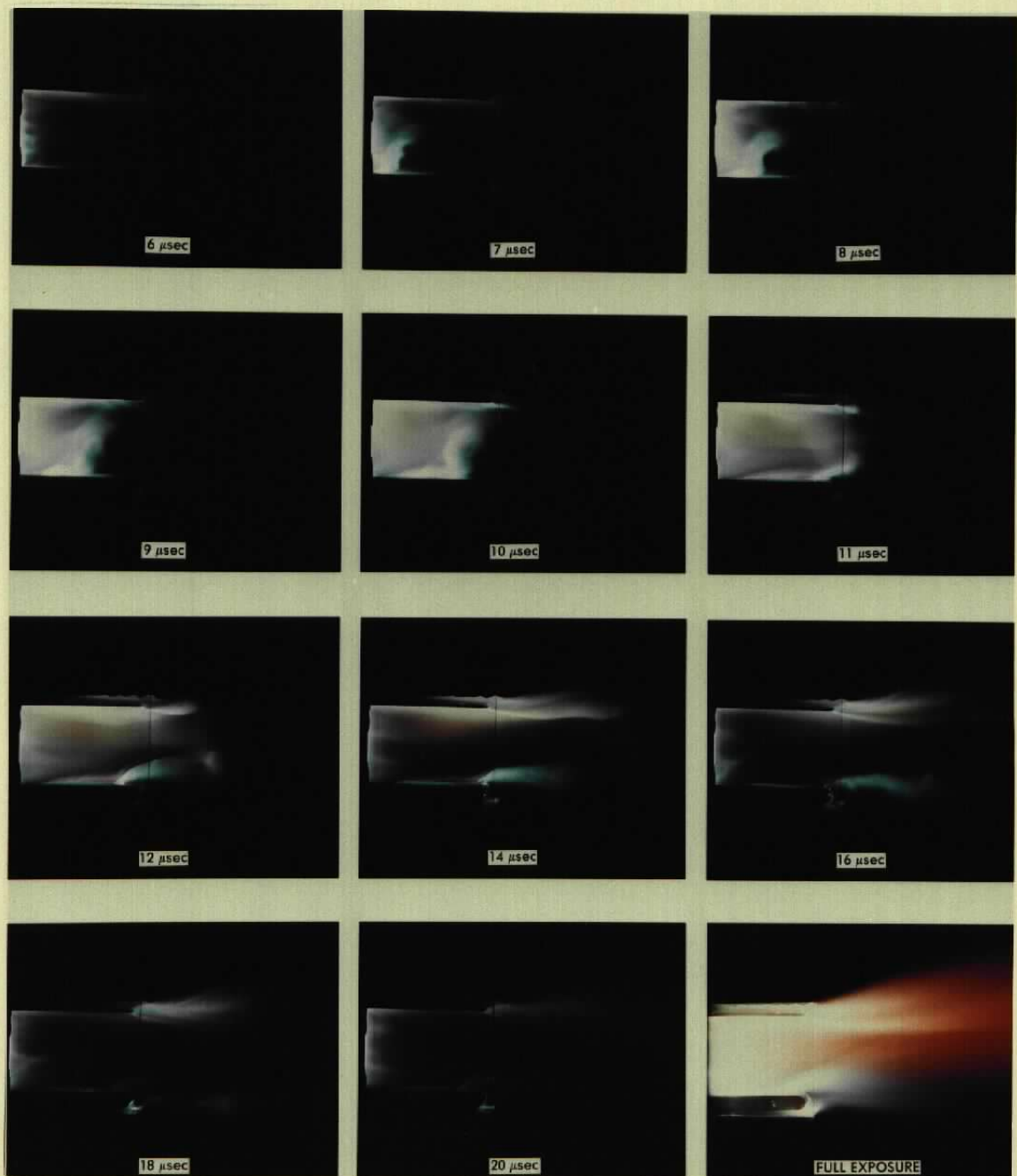


Figure 33. Photographs of plasma with glass nozzle.

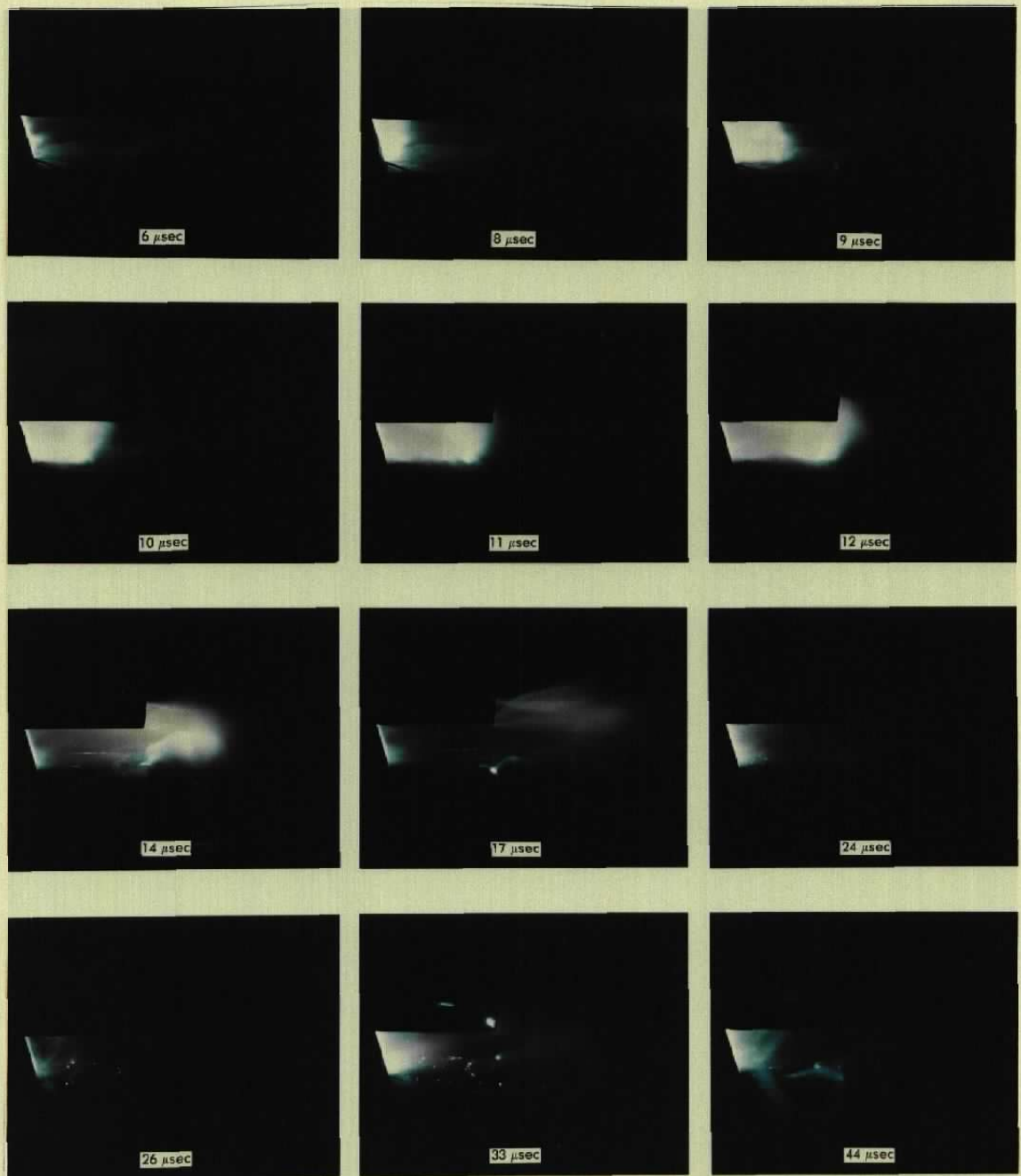


Figure 34. Photographs of plasma with no nozzle (45 deg).

3.5 GASES PRODUCED BY THE PLASMA ENGINE

Each engine pulse is followed by a rapid pressure rise in the vacuum chamber which then decays to a base pressure as the vacuum pumps remove the gases. Preliminary measurements with a mass spectrometer (Ref. 1) had shown this gas load to be a mixture of gases associated with the Teflon sublimation plus a significant quantity of HF and a gas with a molecular weight of 28. The tests reported in this section were conducted to better define these gases and, if possible, to determine their origin.

The early attempts to use the mass spectrometer in the direct flow from the plasma engine were not successful due to interferences from photoelectrons and reflected ions. During this phase of the program a mass spectrometer was installed as shown schematically in Fig. 35. The small sampling orifice and the ionization head of the spectrometer were aligned with the exit plane of the engine nozzle. A solenoid-activated shutter could be operated to cover the orifice to block any radiation or direct flow from the engine. However, in this position there was sufficient clearance below the shutter to allow the randomized gas molecules in the test cell to flow through the orifice and be sampled by the mass

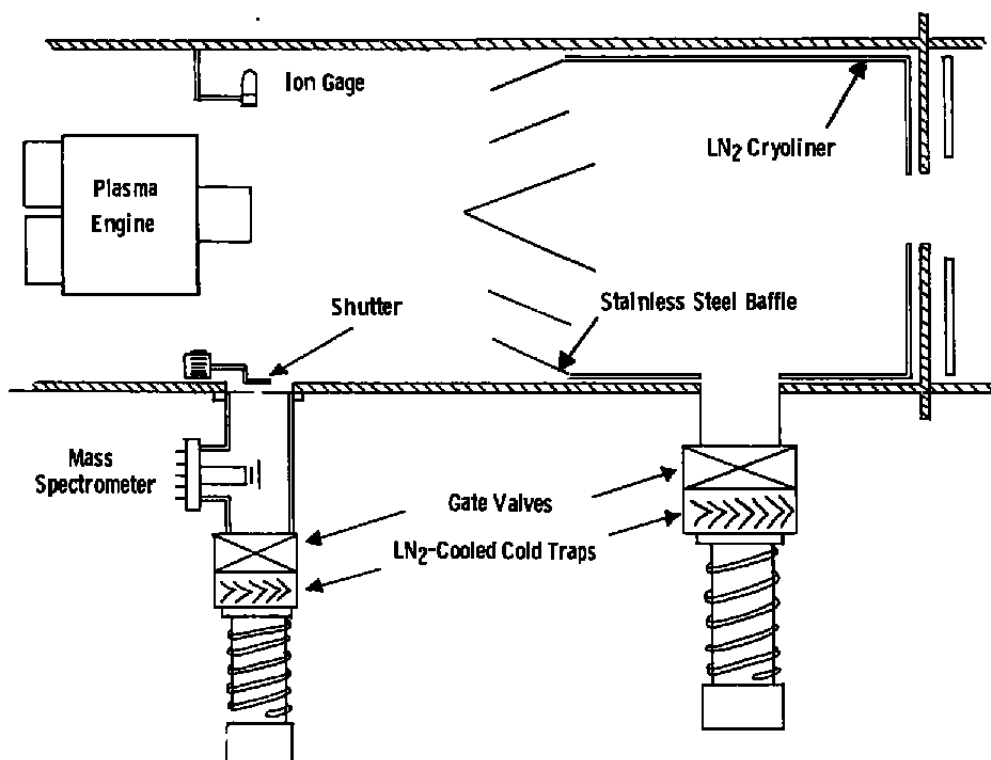


Figure 35. Installation of mass spectrometer.

spectrometer. In order to provide some quantitative data on the gases generated by the plasma engine a gas calibration system was developed to be used with both the chamber ionization gages and the mass spectrometer.

3.5.1 Calibration of the Ion Gages and Mass Spectrometer

Ionization-type pressure gages have different sensitivities for different gases. Most vacuum gages are supplied with a pressure readout which has been calibrated to read vacuum chamber pressure with air as the primary gas. There is a significant difference between the chamber pressure and the gage readout when gases with different ionization potentials are used. Therefore, a calibrated gas addition system was connected to the test chamber, and a technique was developed to calibrate the chamber pressure gages.

The gas addition system is shown schematically in Fig. 36. Sample gases which could be obtained in pressurized bottles were connected as needed at valve H. A gas generator consisting of a stainless steel reservoir which contained 20 gm of the Teflon fuel block mounted in a nichrome heater was connected at valve J. Gases from either source could be used to charge the reservoir, and this pressure could be determined by an aneroid-type pressure gage calibrated from 0 to 800 mm. This gage calibration was not dependent on gas

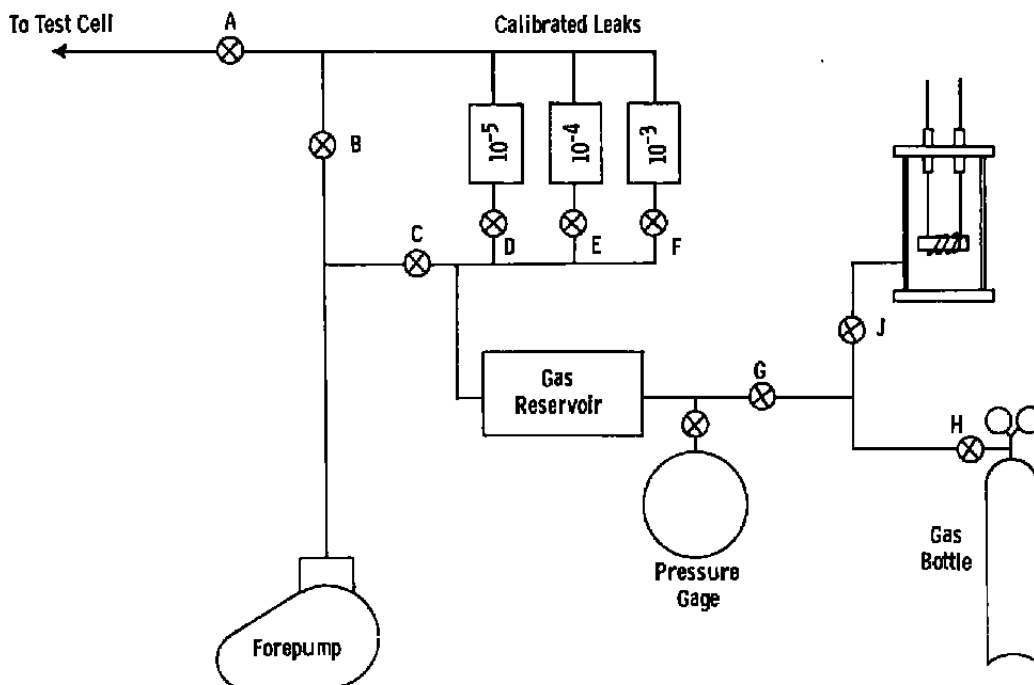


Figure 36. Calibrated gas addition system.

species. The gas from the reservoir could be bled into the test chamber through any one of three sintered steel leaks by opening the appropriate valves. Construction and calibration of the sintered steel leaks are described in detail in Ref. 5.

Once calibrated for each of the gases of interest, the leaks were used to add these gases to the test cell at controlled rates so that the ion gages could be calibrated. The technique used was to first pump the vacuum chamber to its base pressure and then close all the gate valves. With no pumping the chamber pressure slowly rose due to outgassing. This rate of pressure rise was recorded. Next the valves were opened and the chamber was again pumped to its base pressure. At this point the reservoir of the gas addition system was charged with the gas of interest, and a calibrated leak was opened. The pressure in the gas reservoir was adjusted until the ion gage on the test cell read in the low 10^{-5} -torr range. The gage valves were then closed and once again, with no pumping, the chamber pressure rose and its rate of rise as indicated by the ion gage was recorded. From Boyle's equation,

$$\frac{d(PV)}{dt} = \frac{dn}{dt} RT$$

or, for constant values of T,

$$P \frac{dV}{dt} + V \frac{dP}{dt} = \frac{dQ}{dt}$$

where

$$\frac{dV}{dt} = \text{pumping speed of the pumps, } \ell/\text{sec}$$

$$\frac{dP}{dt} = \text{rate of pressure change, torr/sec}$$

$$Q = \text{gas addition, torr-}\ell$$

$$P = \text{vacuum chamber pressure, torr}$$

$$V = \text{vacuum chamber volume, } \ell$$

When the gage valves closed, then

$$\frac{dV}{dt} = 0$$

enabling the equation to be rewritten

$$V\left(\frac{\beta dP_g}{dt}\right) = kP_f$$

where

P_g = pressure as read by the ion gage, torr

β = a calibration factor for the gage

k = conductance of the leak, ℓ/sec

P_f = reservoir pressure in the gas addition system, torr

Thus the gage calibration factor can be obtained from

$$\beta = \frac{kP_f}{V\left(\frac{dP_g}{dt}\right)}$$

The volume of the test chamber was calculated from measurements of its internal dimensions and was determined to be 2676 ℓ . Values of k and β for the various gases are presented in Table 8. The vacuum chamber pressures reported in various figures in this text have all been corrected for the dominant gas species.

Table 8. Calibration Factors for Various Gases

Gas	β	k , ℓ/sec	Molecular Weight
N_2	1.00	1.05×10^{-3}	28
CO	0.75	1.05×10^{-3}	28
H_2	1.77	3.4×10^{-3}	2
$(C_2F_4)_2$	0.33	0.34×10^{-3}	200
C_2H_2	0.40	1.09×10^{-3}	26
CO_2	0.57	0.82×10^{-3}	44
HF	?	?	20

The mass spectrometer was calibrated by adding the specific gas of interest to the vacuum chamber and recording the equilibrium pressure by the ion gage. Then its correction factor was used to determine the true chamber pressure. This was used to calibrate the partial pressure peak height recorded by the mass spectrometer.

3.5.2 Sampling with Mass Spectrometer

Figures 37 and 38 present the mass spectra of the gases produced in the chamber for engine firings with both the small and large capacitors and no cryogenic pumping. These data were taken many weeks apart with the mass spectrometer removed and reinstalled and

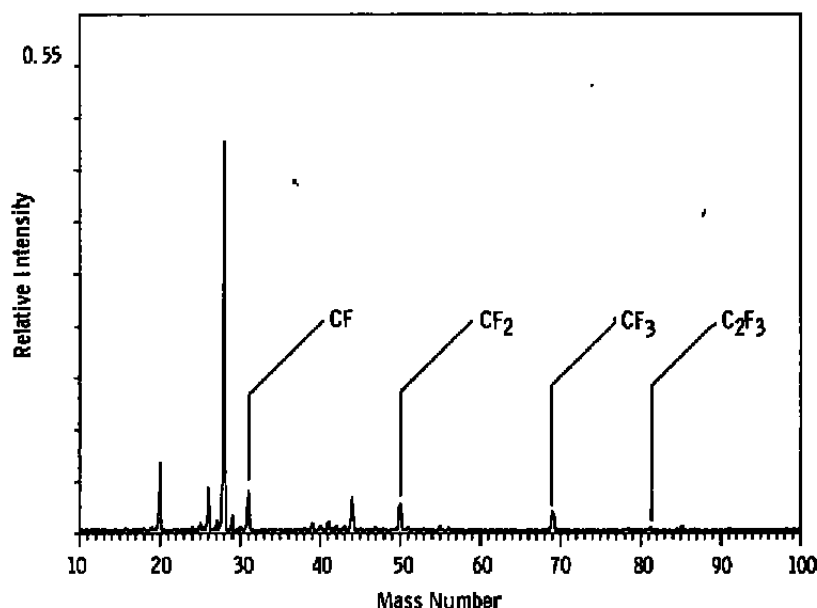


Figure 37. Engine (small capacitors).

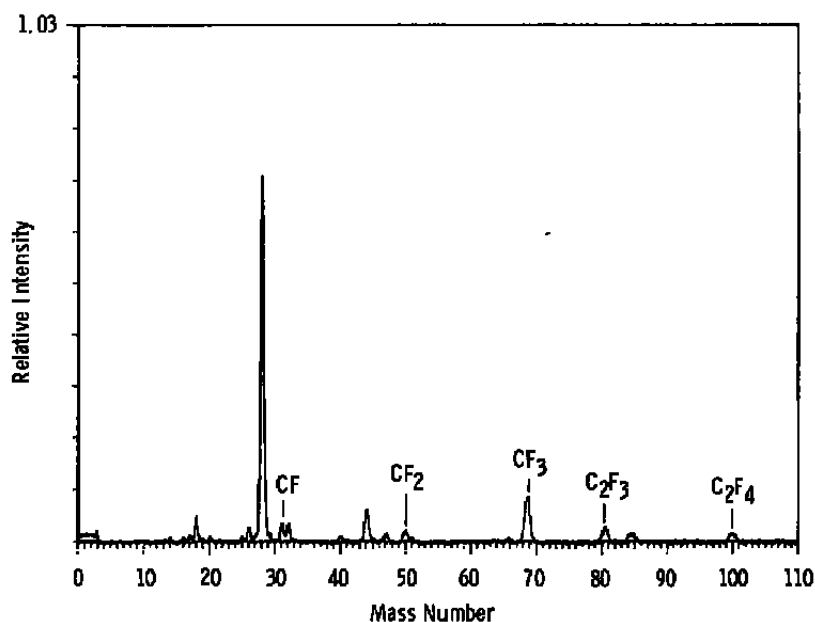


Figure 38. Engine (large capacitors), mass Nos. 0 to 110.

realigned, thus changing its sensitivity; therefore, they cannot be used to determine the relative quantities of gases produced by the different capacitors. In general, however, there was an increase in the gas load with the larger capacitors. The primary point of interest is that for both firings the major gas load is from gases with masses 28 and 20, neither of which is associated with the general cracking pattern from the Teflon. Mass 20 had previously been positively identified as HF, and mass 28 had been suggested as possibly N_2 being desorbed from test chamber walls (Ref. 1). However, closer examination of the spectrum in the lower mass range during these tests (Fig. 39) shows significant peaks at 12 and 16 with only a slight contribution at 14. This would suggest that mass 28 is CO rather than N_2 . This fact was confirmed by adding pure gases to the test cell (Figs. 40 and 41). Also, as noted in Fig. 39,

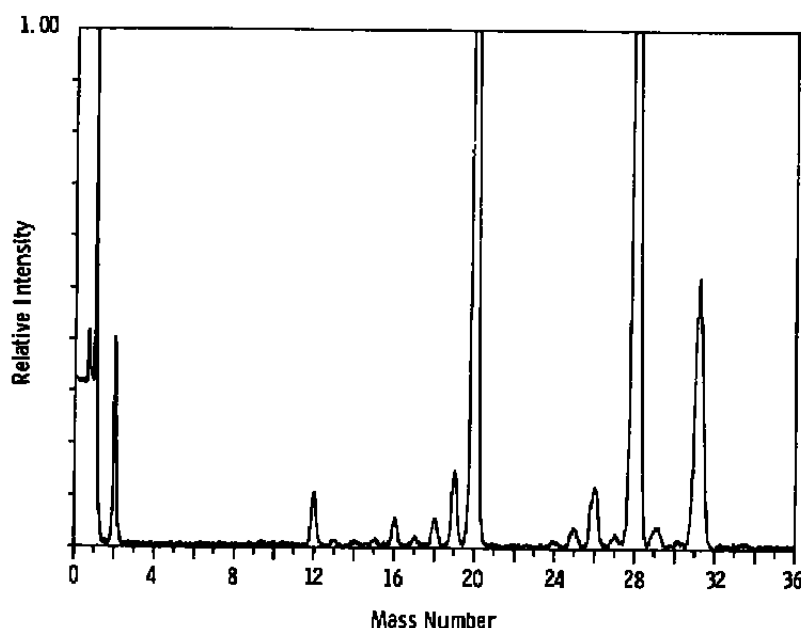


Figure 39. Engine (large capacitors), mass Nos. 0 to 36.

there is a significant contribution of H_2 to the chamber gas load from an engine pulse. In addition, mass 26 is also present. The only gas which has this as a dominant peak is acetylene (C_2H_2) (Fig 42).

The combination of these data suggests a source of H and O with these atoms reacting with the atomic C and F produced by the engine. The most obvious contributor of the hydrogen and oxygen is water (H_2O), and the Teflon fuel was considered a likely source.

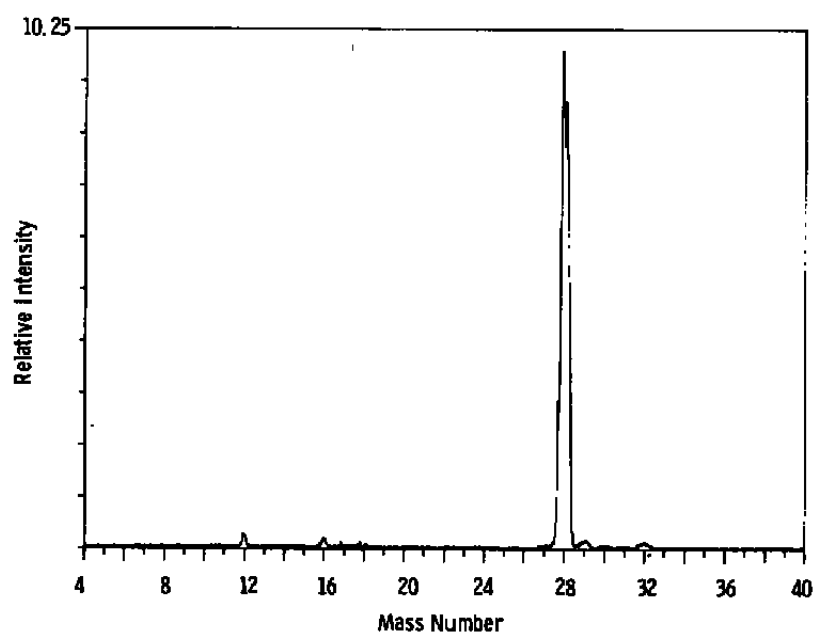


Figure 40. Carbon monoxide (CO), pressure = 1.8×10^{-5} mm.

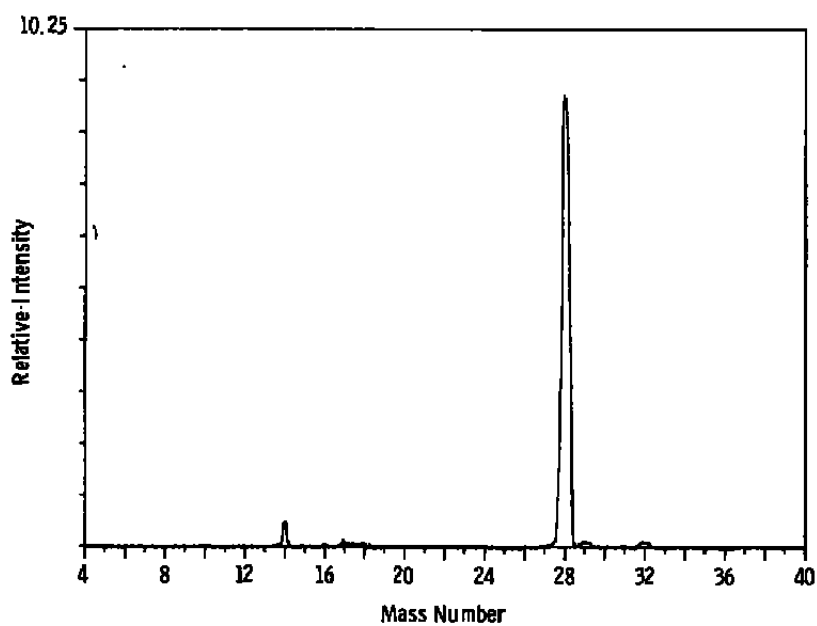


Figure 41. Nitrogen (N₂), pressure = 2.4×10^{-5} mm.

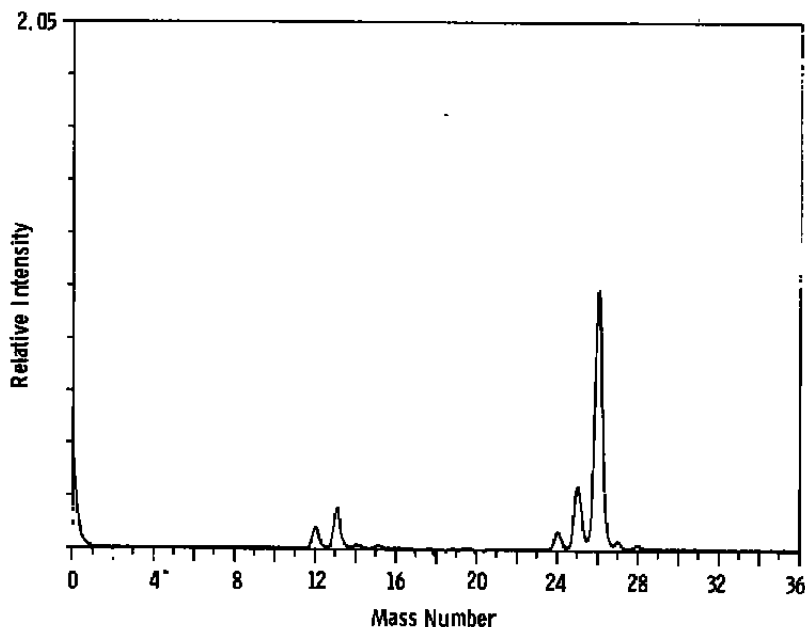


Figure 42. Acetylene (C_2H_2).

3.5.3 Analysis of Teflon

A sample of the Teflon was cut from the engine fuel bars, installed in a nichrome heater, and located just above the sampling orifice to the mass spectrometer. The chamber was pumped down to its normal operating range (2×10^{-6} torr), and the Teflon was slowly heated. The mass spectrum of the gases evolved is shown in Fig. 43. There was no evidence of H_2O (mass 18) in this test. Without changing the mass spectrometer sensitivity, the chamber was pumped to its base pressure and then the engine was fired. The spectrum of the gaseous products is presented in Fig. 44. In comparing the C_xF_y ions it is noted that the engine pulse spectrum shows a higher concentration of mass 69. This indicates that the gases from the engine pulse contain a mixture of C_2F_4 , CF_4 , and C_2F_6 , with a larger concentration of the CF_4 and C_2F_6 species than the pyrolysis products from the Teflon in the nichrome heater. The fact that the major part of the 69 peak is from a different gas from the 31 peak is shown by the rate of pressure rise of the two peaks after an engine firing (Fig. 45). Mass 69 rises much slower. When normalized to the mass 28 peak it parallels the rate of rise of mass 28. This would suggest that these gases which produce mass 69 in the spectrometer are being formed by chamber wall reactions similar to the CO.

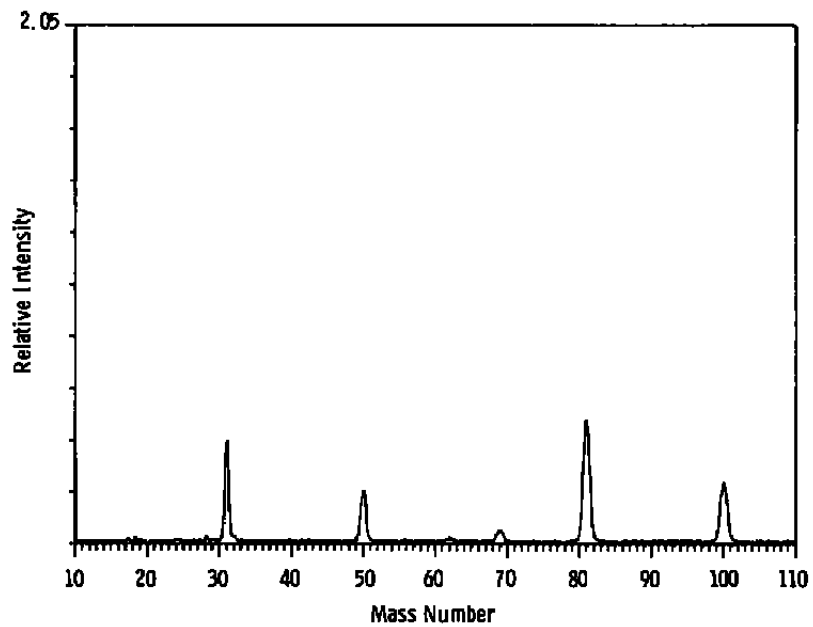


Figure 43. Teflon sublimation.

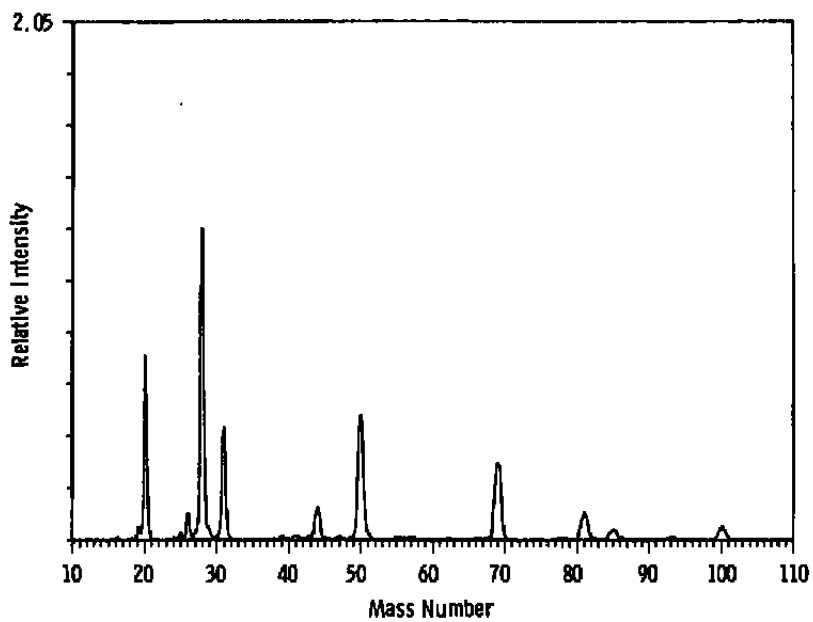


Figure 44. Engine pulse.

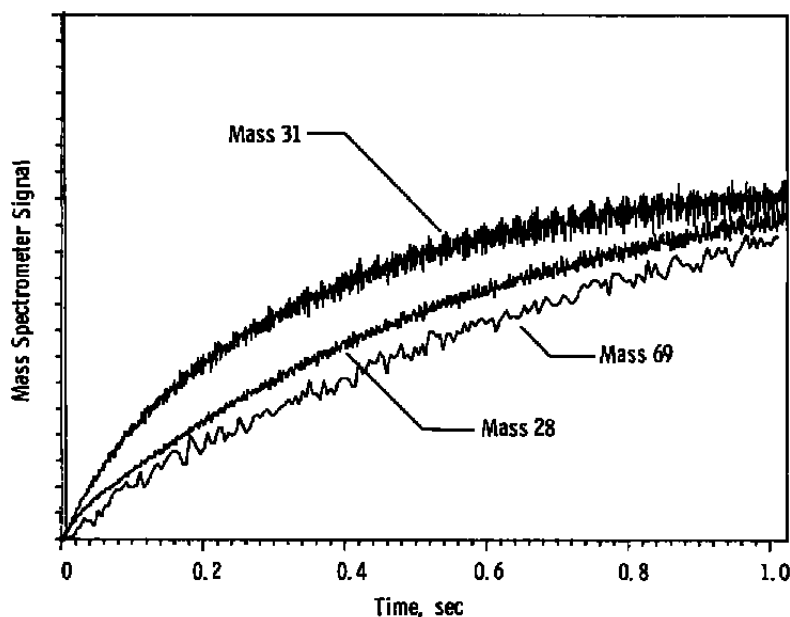


Figure 45. Pressure rise (masses 28, 31, 69).

3.5.4 Quantity of Gases Produced per Engine Pulse

The quantity of gases produced per engine pulse was determined by closing all gate valves and then firing the engine one time. The net increase in pressure is presented in Fig. 46 for the 64- μ fd capacitors and in Fig. 47 for the 80- μ fd capacitors. These pressures are as read by the ion gage and are not corrected for gas species. Both figures contain two pressure traces. The lower curve is the pressure rise due to the normal outgassing of chamber walls. Later data from the mass spectrometer indicate that the major peaks of this gas load are at masses 18 and 28. Superimposed on this baseline chamber pressure are the rapid rise and subsequent pressure history following a single engine pulse. The initial rise and decay are not caused by a gage overshoot but represent a pressure decay due to absorption on the chamber walls of some gas produced by the engine pulse. This represents a room temperature absorption since there were no cooled or cryogenic panels in this test. The slow continued rise reflects the continued gas load contribution from the chamber outgassing.

This experiment was repeated with the mass spectrometer tuned to monitor the 28 peak. The pressure rise is presented in Fig. 48. These data have been corrected for the ion gage and mass spectrometer sensitivities and are presented as the partial pressure of CO. Figure 49 presents the data under the same conditions of a closed chamber for mass 31. Again the data are presented in terms of the actual partial pressure. It can be quite easily seen that the gases involved in the rapid pressure decay of Figs. 46 and 47 are those associated with mass 31:

i.e., C_2F_4 , CF_4 , and C_2F_6 . The partial pressures of the major gas species H_2 , CO , and C_2F_4 are tabulated in Fig. 47. No technique was available for calibrating for HF , and no information on HF cracking patterns or sensitivities was found in the literature (Refs. 6 and 7); thus, this gas and possible contributions from C_2H_4 are included as the residual pressure required to account for the observed total gage pressure rise, but the actual partial pressure is in question. Using the chamber volume and the partial pressure of the C_2F_4 leads to an estimate of 0.8×10^{-3} gm of gas produced per engine pulse. If it is assumed that all the CO observed resulted from reactions of atomic carbon produced by the engine, then the volume of CO accounts for an additional 0.1×10^{-3} gm of carbon from the engine. The quantity of fluorine involved could not be measured, but ratioing the quantity of F atoms to C atoms, assuming complete dissociation of the parent monomers, would account for an additional mass of 0.3×10^{-3} gm. This leads to an accountable mass of 1.2×10^{-3} gm of material per engine pulse. The total mass ablated was measured at 1.71×10^{-3} gm. The additional studies which were conducted to complete this mass balance are presented in Section 3.6.

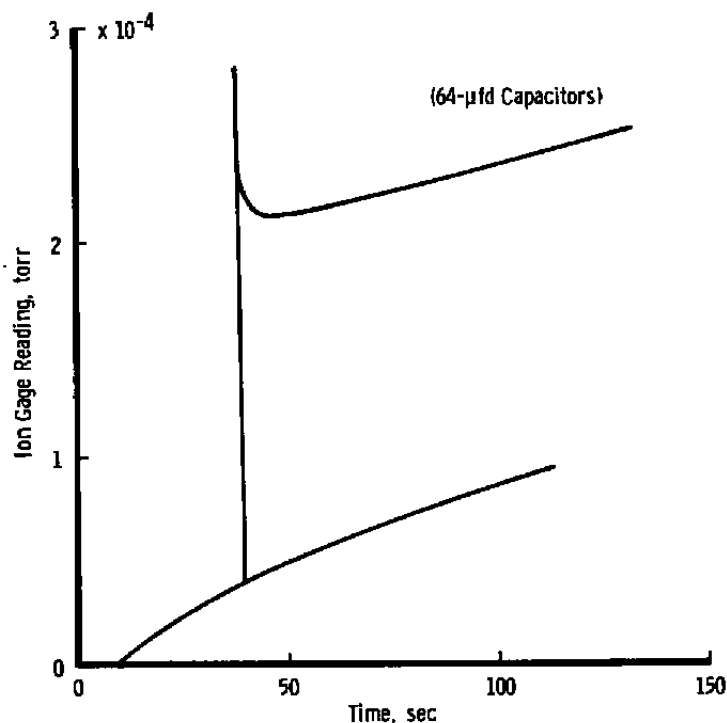


Figure 46. Engine pulse (all pumps closed), 64- μ fd capacitors.

The mass spectra presented in Figs. 50 and 51 represent engine firings with the only change being the cryopanel temperature. The item of interest is the 2.5-fold increase in the mass 28 peak height. Allowing for the fact that gages calibrated at 300°K monitoring gases

at 77°K must be corrected for the so-called thermal transpiration effect (i.e., a factor equal to the square root of the temperature ratio, $\sqrt{300/77}$), then it is apparent that the quantity CO produced has actually increased by a factor of 5. The complexity of the chemical reactions which are occurring on the cryogenic panels is probably best illustrated in Fig. 52. This is a mass spectrum of gases evaporating from a cryopanel after a test series of 200 engine pulses.

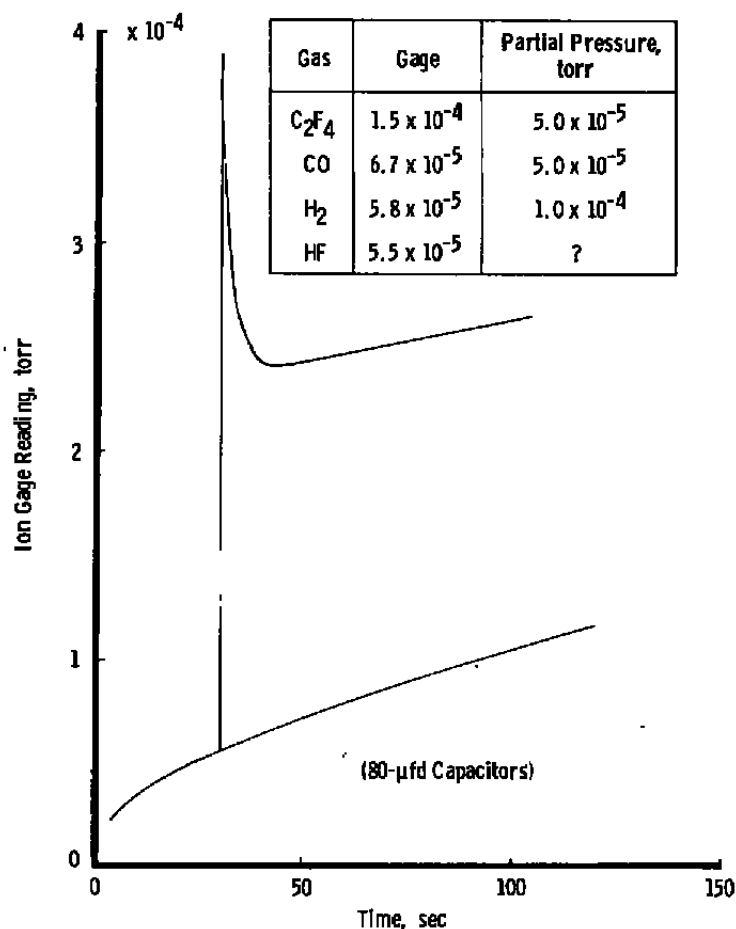


Figure 47. Engine pulse (all pumps closed), 80-μfd capacitors.

It can be concluded from this series of tests that the H₂, HF, and CO are produced by reactions of the C and F atoms with water vapor absorbed on surfaces in the test cell. Studies with the UV spectrometer (Section 3.4) showed that these surfaces also include the inside faces of the engine nozzle.

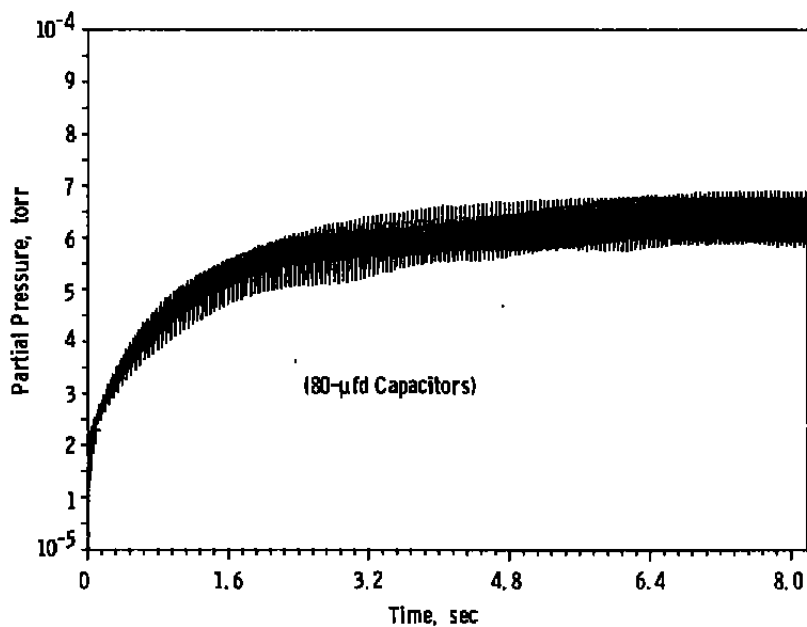


Figure 48. Engine pulse (mass 28).

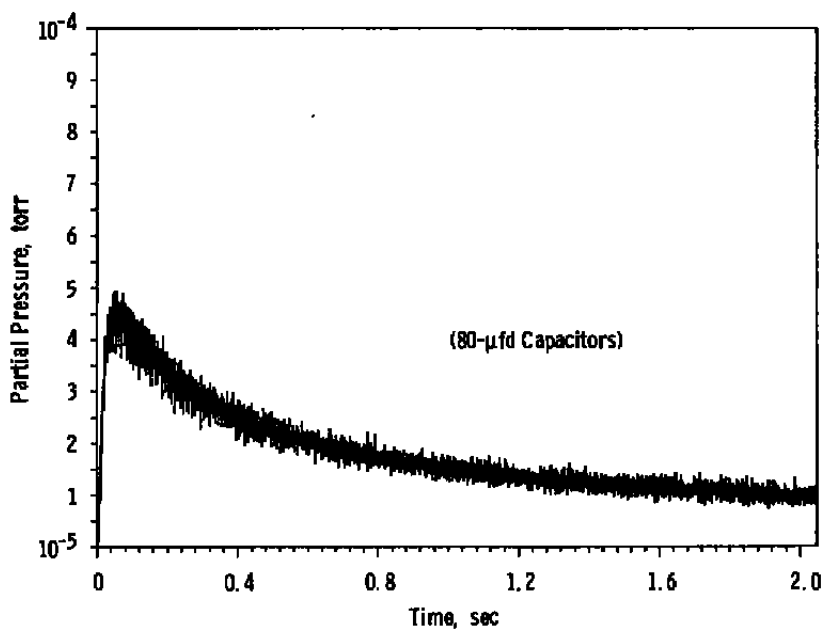


Figure 49. Engine pulse (mass 31).

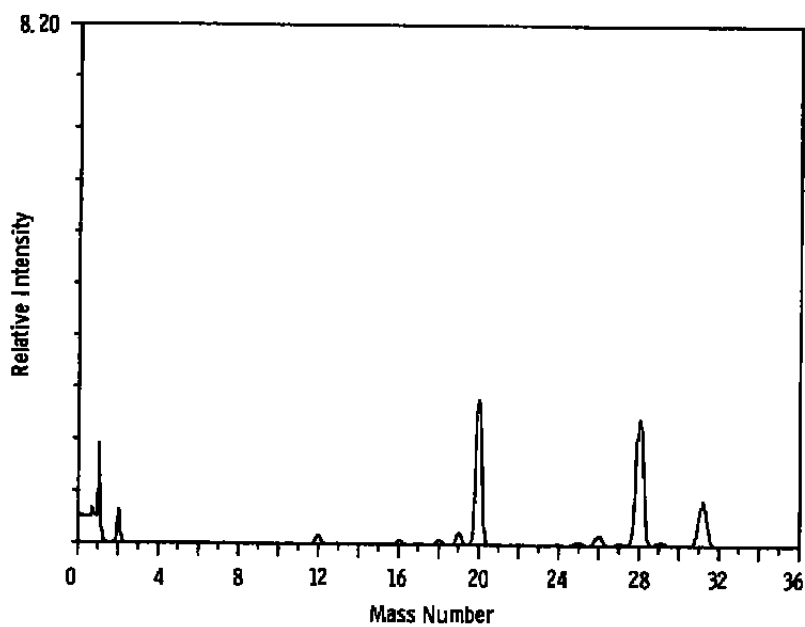


Figure 50. Cryopanel, 300°K.

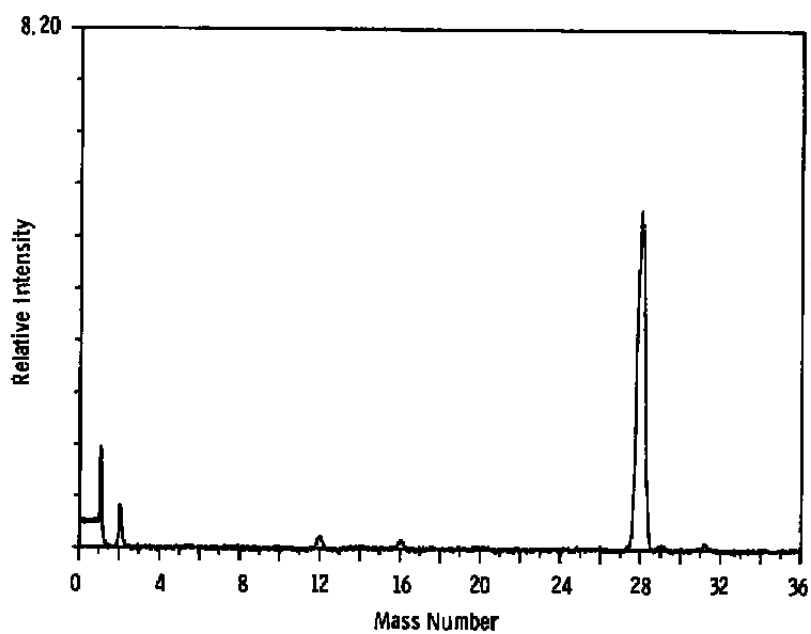


Figure 51. Cryopanel, 77°K.

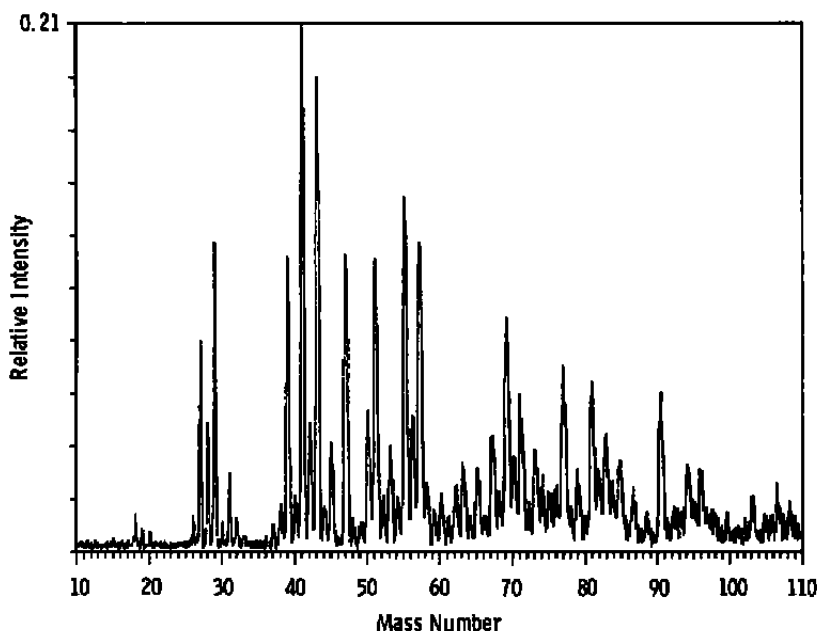


Figure 52. Cryopanel, -32°C .

3.5.5 Detection of Gas Neutrals and Ions

Two attempts were made to measure the direct flux of material from the engine nozzle in the exit plane. An ionization gage was located directly above the nozzle, and the mass spectrometer, as described previously, was installed below the engine.

3.5.5.1 Measurements with an Ionization Gage

A miniature G.E. ionization gage was mounted above the engine as noted in Fig. 35, with specific dimensions as shown in Fig. 53. The gage controller had been modified to provide a fast response. With the filament off, there was a large signal as the engine fired. Attempts to suppress this signal with electrostatic screen grids or by biasing the gage collector were unsuccessful. However, with the filament emission turned on, this initial signal was followed by a smaller but identifiable pulse.

The data presented in Fig. 54 were obtained by recording the ion gage signal with filament emission and then subtracting the next ion gage signal of an engine pulse recorded with the filament off. It is noted that this pulse of gas precedes the general pressure rise in

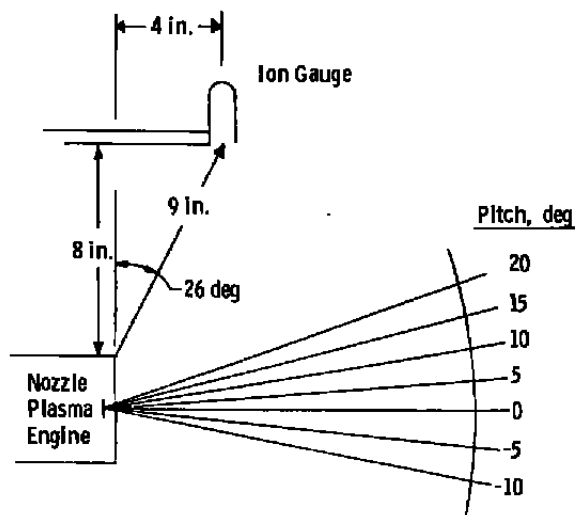


Figure 53. Location of ion gage.

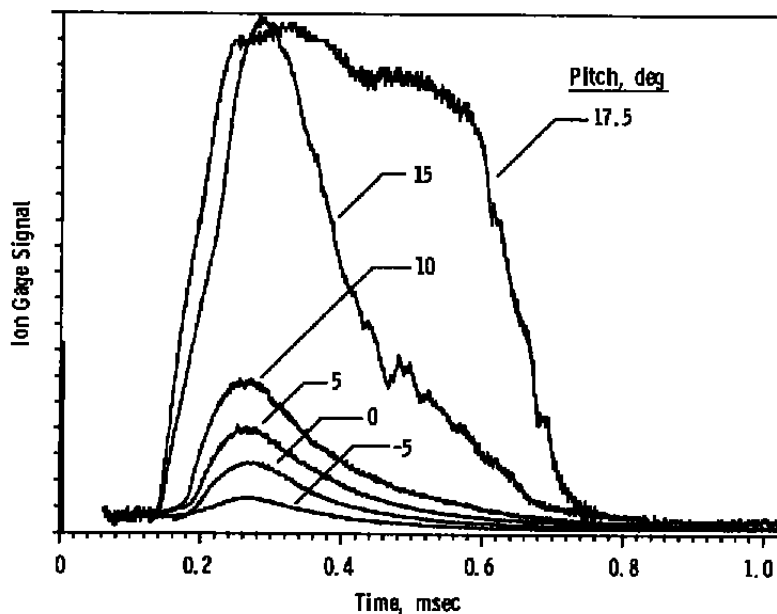


Figure 54. Neutral gas molecules.

the vacuum chamber which, as shown in Fig. 55, occurs at $t = 0.05$ sec. The signal recorded at $+17.5$ deg has obviously overloaded the gage although it might be considered of value in that it indicates the time duration of the pulse. The signal levels at each of the motor positions are larger than those obtained for steady-state operation of the ion gage, and thus care should be exercised in comparing the relative peak heights of the pulses since the gage response may not be linear. An attempt to calibrate the ion gage by adding gas to the

vacuum chamber to reproduce the gage output signal revealed that the gage filament could not maintain a steady-state emission at the pressures required to duplicate even the lowest pressure pulse. While the ion gage would therefore appear to be a useful diagnostic tool for backflow detection of neutral gases, it will require some kind of pulsed gas flux calibration scheme in order to quantify the data.

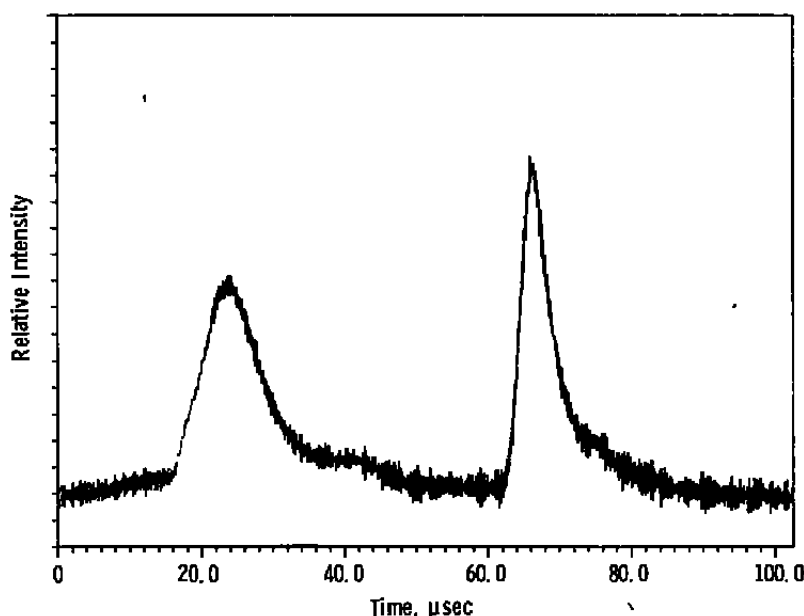


Figure 55. Ion pulse (mass 12).

3.5.5.2 Measurements with a Mass Spectrometer

The mass spectrometer was used with the solenoid shutter in the open position to look at that part of the engine pulse which saturated the ion gage. Figure 55 presents a typical signal for the first 100 μ sec. The first pulse is consistent and occurs even with all the mass spectrometer ionization, extractor, and quadrupole voltages set at zero. It can be eliminated by closing the solenoid shutter or by removing the high voltage from the electron multiplier detector on the mass spectrometer. The initial time and the duration of this signal are the same as those observed by the UV spectrometer, which was also looking across the exit plane of the engine nozzle (Section 3.4). This signal is induced by photons from the plasma. The second peak is not so well behaved. While the general width was fairly consistent, its timing varied from the earliest shown in Fig. 55 (i.e., 64 μ sec) to as late as 90 μ sec. Its intensity varied over two orders of magnitude, with the majority of the pulse heights giving 100-mv signals with occasional 10-v signals.

The spectrometer was tuned over the mass range from mass 4 to mass 28. The peak height of this second signal was averaged over 50 engine pulses at each setting, and the data are presented in Fig. 56. These data suggest that the signals are produced by carbon ions. There is some selectivity by the quadrupole section of the mass spectrometer, but it is obvious that the resolution is very bad. Attempts to improve the resolution by using the tuning controls on the instrument reduced the total signal levels but did not significantly narrow the bandwidth. Even with the poor selectivity, it can be noted that there is no evidence of fluorine ions. It would appear that these bursts of carbon ions can be associated with the bright spots which are observed on the electrodes in the Kerr cell photographs.

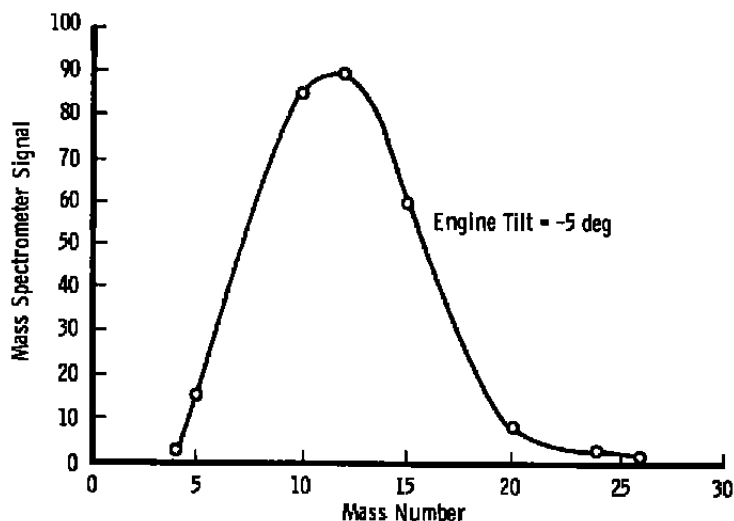


Figure 56. Carbon ion signal.

3.6 SOLIDS PRODUCED BY THE ENGINE

3.6.1 Particles Collected on Witness Plates

There are several types of particles emitted by the engine. Carbon flakes varying from 1 to 500 μm in diameter are consistently collected on witness plates located throughout the test chamber. Microphotographs of these particles and one possible source, i.e., the electrode surfaces, are presented in Ref. 1. One additional source has been identified during these tests. During the ablation process some carbon is produced at the edges of the Teflon bars (Fig. 57). These particles can be ejected as flakes, or they may be ejected along with some of the Teflon and deposited as particles in a Teflon matrix (Fig. 58). The diameter of the equivalent sphere from which these deposits were made is on the order of 10 μm . These events are erratic and not predictable. Periodic observation of witness plates located at the

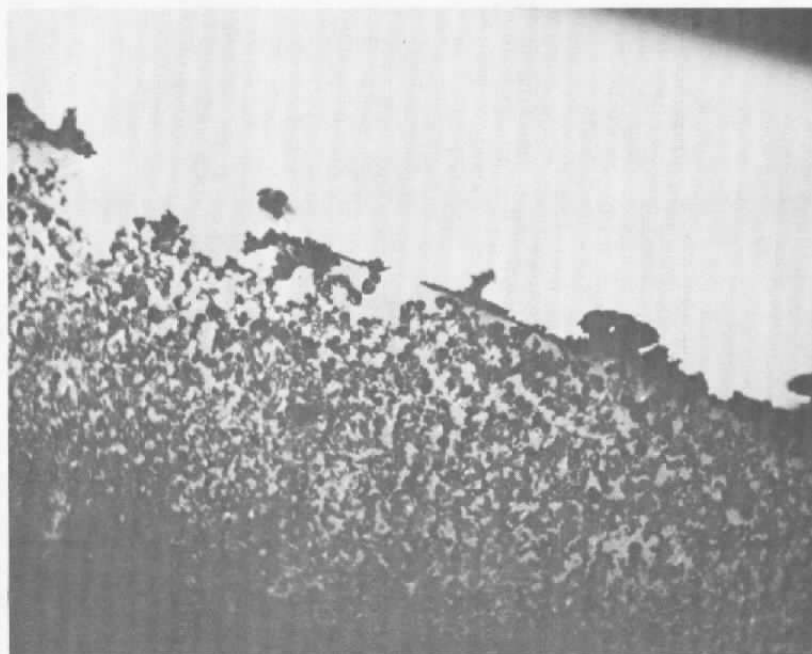


Figure 57. Ablating edge of Teflon fuel block.

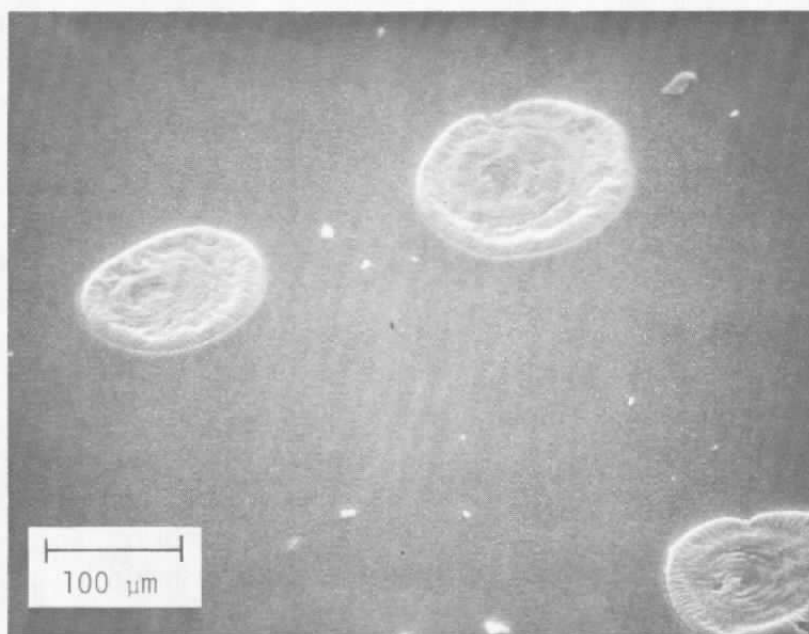


Figure 58. Scanning electron micrographs of deposits.

exit of the nozzle indicate that there may be several hundred pulses with no deposit followed by several pulses in which a noticeable accumulation of material is collected. There does not appear to be any correlation between production of these particles and steady-state pulsing versus startup after an extended shutdown. In a previous test (Ref. 1) witness plates located at a 45-deg angle to the exit plane did not collect any particles. Repeats of these tests gave similar results, leading to the conclusion that these relatively large particles are confined to at least a 45-deg, and probably smaller, trajectory angle. The photographs in Fig. 61 are among the few which indicate some ellipsicity to the deposit and thus suggest a significant axial velocity.

3.6.2 Material Collected on Test Chamber Walls

During the conduct of these tests a considerable quantity of a brown-colored, solid material collected on the downstream walls of the test chamber. The engine was removed from the test cell periodically and this deposit was cleaned from the walls. After the test sequence to measure the usage rate of the Teflon fuel (6184 engine pulses) the chamber was brought to atmospheric pressure and the engine was removed and disassembled. During this time the test chamber was left open, and the following day it was noted that the usual brown deposit had started to peel from the chamber walls. Previous deposits had required scrubbing with steel wool in order to remove them. A soft brush was used to collect as much of the deposit as possible. During the test 7.22 gm of Teflon were ablated from the fuel rods, and 2.7 gm of material were recovered from the chamber walls. A photograph of typical pieces of the deposit is shown in Fig. 59. A scanning electron microscope photograph at a magnification of 12,000X is presented in Fig. 60. The material, being a nonconductor, charged heavily under the electron beam, making it difficult to get a good focus. However, the general structure of fused spheres is quite evident. Spheres in this photograph range from 0.5 to 2.7 μm in diameter.

Subsequent tests on this material have shown that it is hygroscopic and that peeling occurs if the deposit is exposed to water vapor for a period of a few hours. Quantities of the material have been checked for chemical activity. Apart from its being hygroscopic, it appears to be as inert as the initial Teflon. The 2.7-gm sample collected from the test chamber was leached in neutralized distilled water and analyzed for HF. This test indicated a fluorine ion content of 0.22 percent by weight or approximately 6×10^{-3} gm of HF adsorbed in the sample.

The morphology of the wall deposit suggests that a considerable portion of it is a direct accumulation of material emitted from the plasma engine as particles or droplets. However,

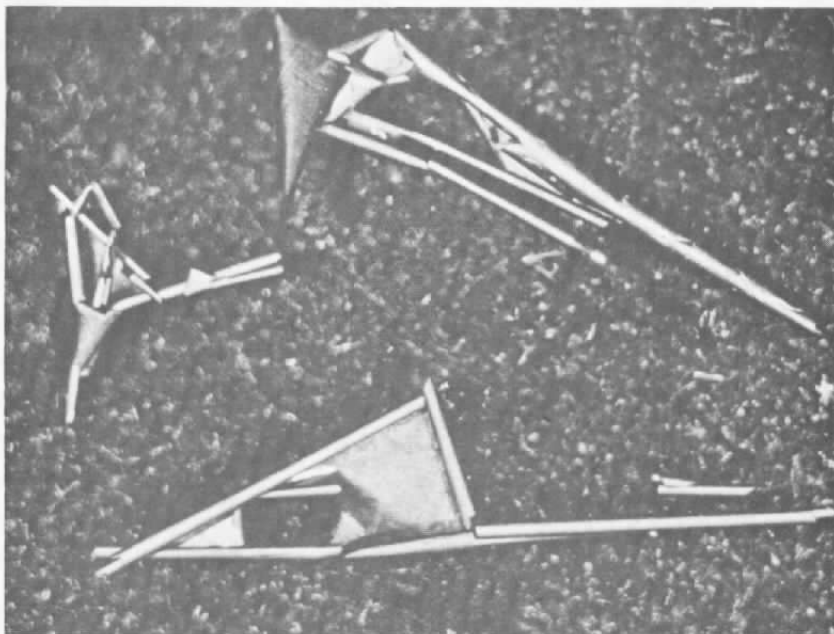


Figure 59. Material collected on test chamber walls.

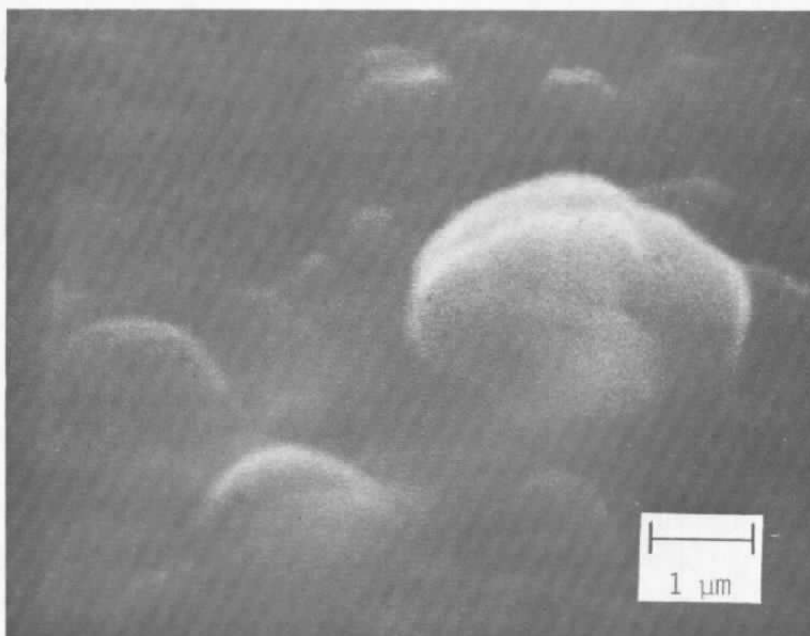


Figure 60. SEM photograph of surface of deposit (12,000X).

the quantity of this material (0.4×10^{-3} gm/pulse) seemed quite high, and therefore, some experiments were conducted to determine whether the material was being directly deposited from the engine. The first experiment was a simple shadow box with witness plates. This was followed by measurement of both the mass flux and its velocity using a quartz crystal microbalance (QCM) with a rotating shutter.

3.6.3 Backflow Observed with Shadow Box

Part way through this test program it was noted that there were distinct and well-defined shadow patterns where the partially depolymerized Teflon was collecting on the interior surfaces of the test chamber. Some of these shadows were aligned with the lip of the engine nozzle. A shadowbox shown schematically in Fig. 61 was constructed and installed in the test chamber. An examination of the detection plate inside the box after 6,000 engine pulses shows a distinct deposit of material expanding at 90 deg and a lesser but still observable

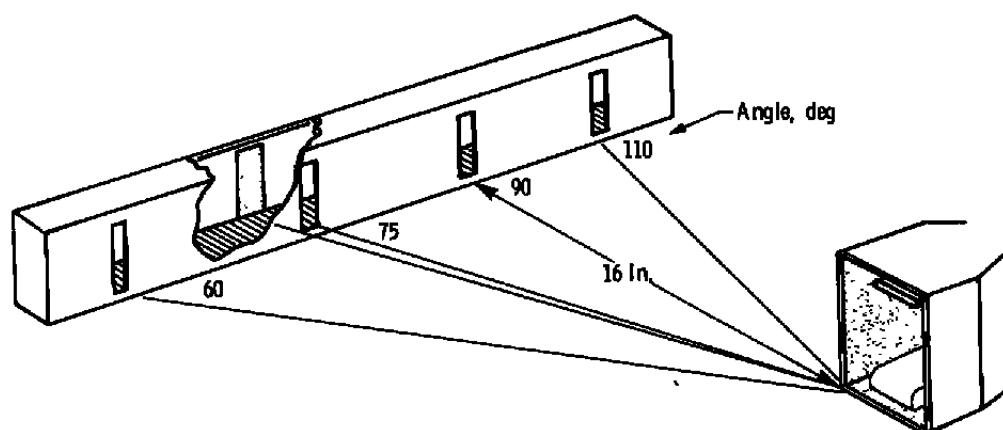


Figure 61. Schematic of shadow box.

deposit at 110 deg. This partially depolymerized Teflon is condensible at room temperature (300°K), and in thin layers is a light tan color. Heavier deposits are dark brown. A specular reflectance measurement was made from each of the samples in the wavelength range from 4000 to 600 cm^{-1} . The data presented in Fig. 62 show a strong absorption band in the 1200 cm^{-1} region, typical of the C-F molecular bond. The intensity of the absorption band can be associated with the quantity of material deposited. However, with this experiment there was no calibration scheme to provide a correlation between the absorption and the mass or thickness of the deposit.

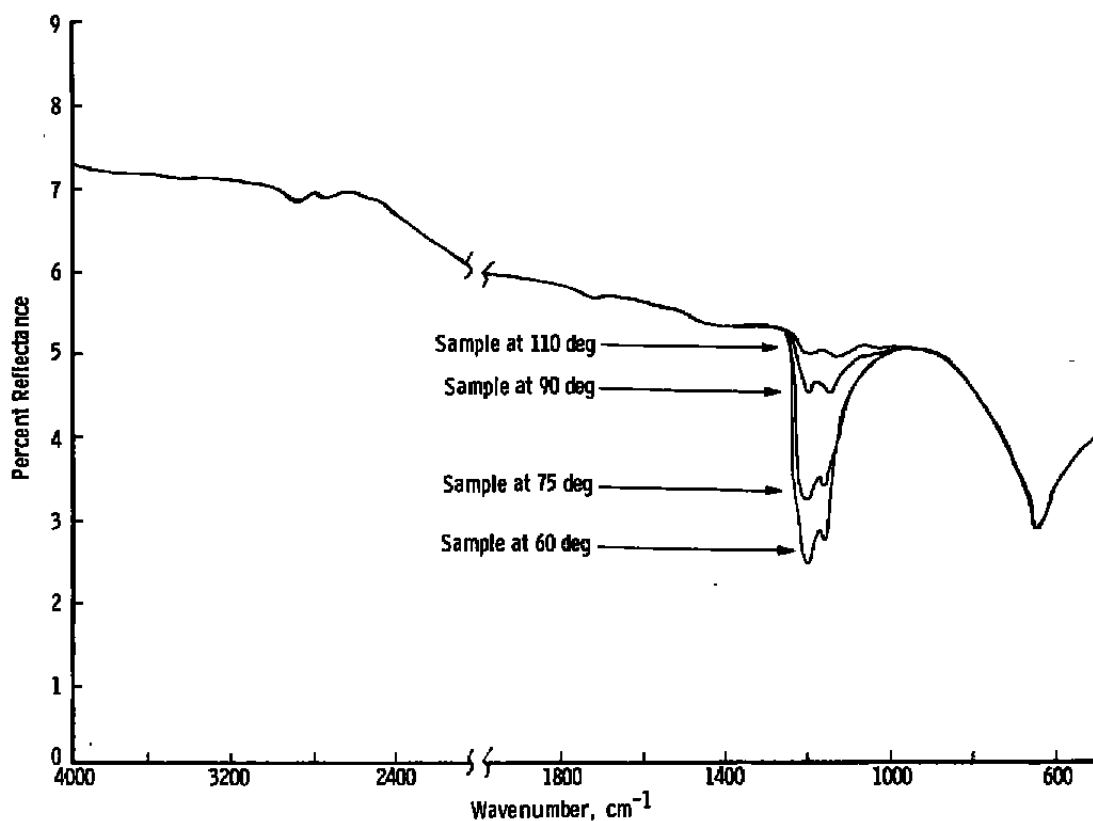


Figure 62. Specular absorption by shadow box deposits.

3.6.4 QCM and Chopper Wheel

A quartz crystal microbalance (QCM) was fitted with a high-speed rotating chopper wheel (Fig. 63) and installed in the test chamber 1.12 m downstream of the engine, 20 cm below centerline. The chopper was rotated by a 12,000-rpm synchronous motor. A photodiode and detector were used to monitor the rotational speed of the wheel and at the same time provide a timing pulse as the chopper orifice passed the detector, which was diametrically opposite the QCM.

For this series of experiments the engine trigger pulse was switched to channel D on the sequencer. Channel D was started by the first timing pulse initiated by the rotating chopper wheel after the main sequencer called for an engine firing. With this arrangement, for channel D set at zero delay, the engine fired when the chopper wheel orifice passed the detector. With channel D set at approximately 2500 μsec (i.e., time for one half revolution of the chopper wheel), the engine trigger pulse occurred when the chopper wheel orifice was

aligned with the QCM crystal. In order to allow for delays in this arrangement such as the 4 μsec associated with the start of the engine (Fig. 4) and possible slight misalignment of the detector on the chopper wheel, the complete system was calibrated by using the flash from the engine as a strobe and photographing the chopper wheel. This technique was used to record the locations of the chopper wheel orifice for various delay times and to check the repeatability of the delays.

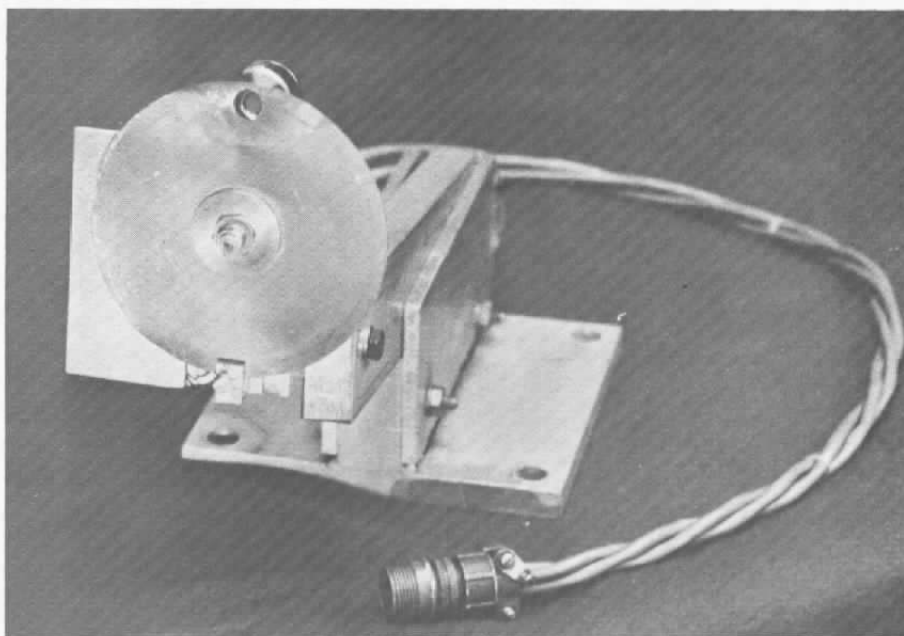


Figure 63. QCM and chopper wheel.

After this timing checkout the system was operated with the engine firing with zero delay. During this period there was no mass accumulation by the QCM. Then gradually increasing delays were dialed into the sequencer. As the time between the engine pulse and the coincidence of the chopper orifice with the QCM decreased, there was observed a point where the QCM recorded a mass deposit with each engine pulse. Further changes in the delay times resulted in larger deposits, which reached a maximum of $6 \times 10^{-8} \text{ gm/cm}^2$ per engine pulse. Beyond this point the mass accumulation decreased, and finally the time delays were so long that there was once again no mass accumulation. The data from this experiment are presented in Fig. 64. Complete alignment of the chopper orifice and the QCM occurred with 2530- μsec delay. The shutter function for two passing circular orifices with 100-percent transmission at 2530 μsec is co-plotted with the QCM data.

The total discharge time for the engine is on the order of 40 μsec ; however, the high-speed photographs indicate that the main plasmoid leaves the nozzle at 10 μsec with a duration of less than 10 μsec . Assuming that the bulk of the material collected by the QCM is contained in this plasmoid leads to a calculated velocity of 40,000 m/sec.

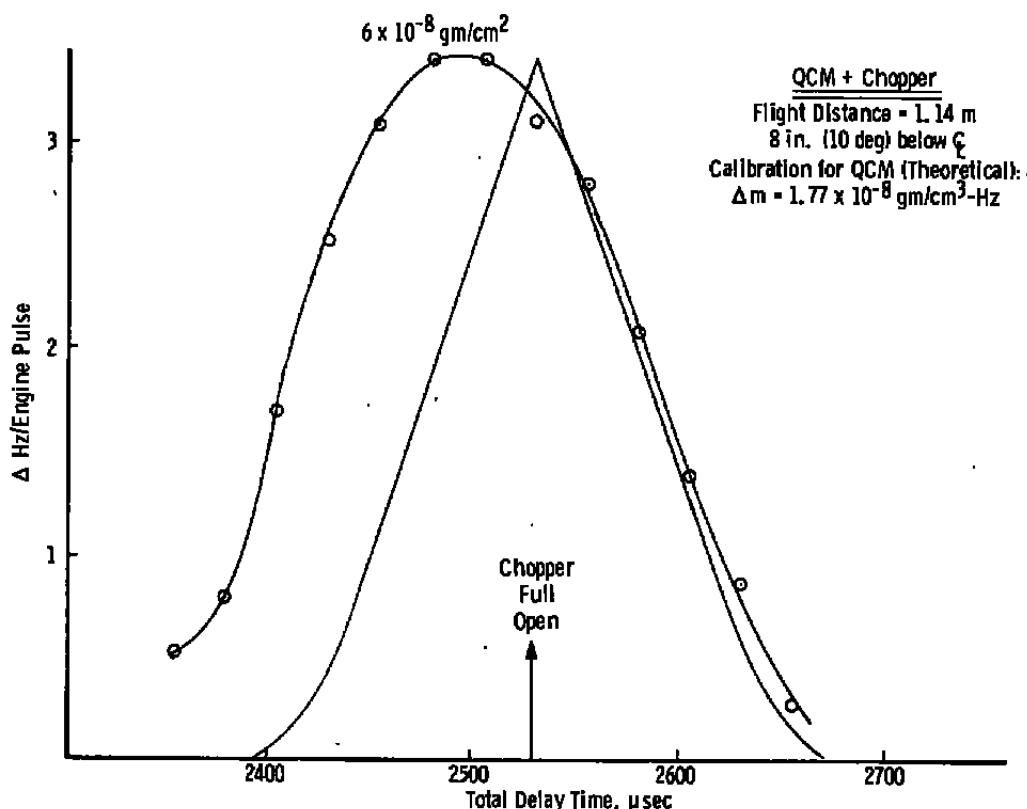


Figure 64. Mass collected by QCM.

The maximum mass deposition rate which was observed by the QCM at this location was $6 \times 10^{-8} \text{ gm/cm}^2\text{-pulse}$. This information plus the plume profiles as presented in Ref. 1 gives an integrated mass flux in the forward flow of $4.2 \times 10^{-4} \text{ gm/pulse}$.

One final comment on the operation of the QCM in this mode should be made. During the acquisition of the above data the QCM was quite stable, and data points were repeatable for the various delays. However, at the completion of the test the QCM was left in the test cell with the shutter in the open position, and the mass deposit per engine pulse was monitored. It was noted that after approximately 1000 engine firings the mass increase per engine pulse started to decrease. After approximately 2000 engine firings the QCM

sometimes showed a slight mass increase and sometimes showed a mass loss. A new crystal with its freshly coated gold electrode was installed, and the QCM again recorded a consistent gain with each engine pulse.

3.6.5 ATR Witness Plates

ATR plates were installed in the test cell to collect samples of the material deposited on the interior surfaces. The IR absorption spectrum of a sample collected from the front face of the engine after 12,000 engine pulses is presented in Fig. 65. This is primarily material which has rebounded or sputtered from the downstream wall of the test chamber. The spectra are quite similar to those reported in Ref. 1. The absorption at 1700 cm^{-1} and 1200 cm^{-1} is associated with C-F bonds. The absorption from 3600 cm^{-1} to 3800 cm^{-1} is associated with C-H bonds and was previously suggested as possible oil contamination from the vacuum chamber. However, due to the strong evidence of both H and O in the gas analysis, the C-H bonds could well be hydrogenated fluorocarbons in the deposit.

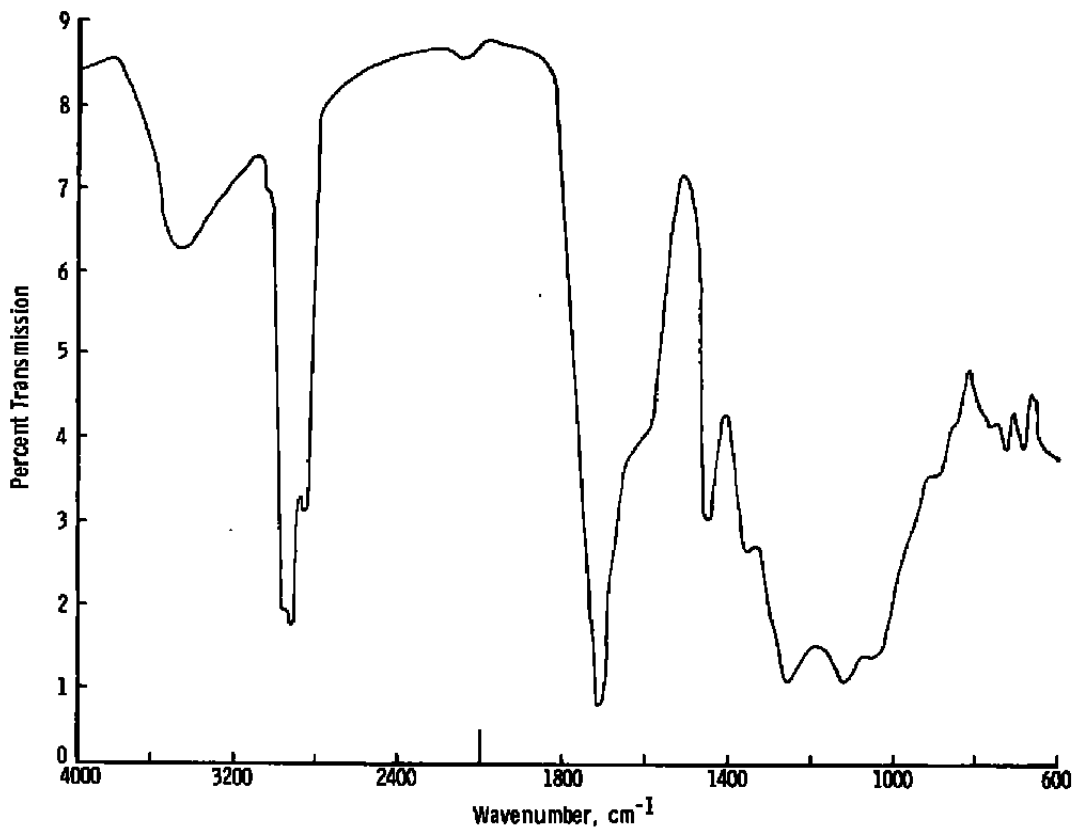


Figure 65. IR absorption spectrum of deposit on ATR plate.

4.0 SUMMARY

4.1 OPERATION OF THE PLASMA ENGINE

The engine was initially fitted with four 64- μ fd capacitors, and some data on the operating characteristics of the engine were acquired with this configuration. These capacitors were then replaced with four 80- μ fd units, and a complete set of data was obtained. With the 80- μ fd capacitors it was observed that the discharge is slightly underdamped and the resulting one and a half oscillations produce three plasma pulses per firing. All three plasmoids were detected with the current probes; however, the intensity of the third plasmoid was too weak to be recorded by the high-speed photography or the VUV/UV spectrometer. The total discharge lasts approximately 55 μ sec and ablates 1.71×10^{-3} grams of Teflon. The first and major plasmoid forms and leaves the engine within 20 μ sec; its velocity has been measured at 40,000 m/sec using a variety of techniques. The second plasmoid travels at 13,000 m/sec.

4.2 PLASMA CURRENTS

The plasma currents were mapped as they traveled down the electrodes. Currents on the order of 1000 amperes (A) were measured as far as 25 cm beyond the exit plane of the engine electrodes. Plasma velocities calculated from these data indicate that the plasma is still accelerating as it leaves the engine, reaching a steady velocity about 20 cm beyond the exit plane.

4.3 MAGNETIC FIELDS

The changing magnetic field during an engine pulse was recorded at selected points from the backwall of the engine (i.e., between the Teflon fuel blocks) to positions external to the engine. These data were very reproducible from one engine pulse to the next both in signal level and in timing. Peak magnetic fields of 0.85 Tesla were measured at the throat of the engine. This occurred at the same time that the peak current of 84 kA was flowing in the capacitor/electrode circuit of the engine.

4.4 PHOTONS PRODUCED BY THE ENGINE

The engine produces a brilliant flash with each firing. Most of the energy is contained in the vacuum ultraviolet portion of the spectrum. A rough estimate of the VUV flux which might be incident on neighboring satellite surfaces indicates levels 10^6 times more intense

than that received from the sun. Although the duration of this flux is only 10 μsec , the possible effects of this VUV pulse should be considered when questions about spacecraft charging and photochemical reactions are raised. Spectral analysis of the radiation from the plasma indicates that it contains multiply ionized C and F along with trace metallic elements identified as components of the ceramic insulators used in the construction of the engine. The plasma produced sufficient radiation in the visible portion of the spectrum to permit 100-nsec exposures and thus record time sequences of its acceleration and ejection from the electrodes.

4.5 GASES PRODUCED BY THE ENGINE

The identifiable plasmoids depart the engine within 55 μsec . Following the plasma discharge there is a hot gas expansion which lasts approximately 750 μsec . During this period background events are induced by the plasma's impacting the test chamber walls. That is, the impact produces electron showers and additional gases. The mass spectrometer has been used to identify these gases as CO, HF, and H_2 , with minor contributions from CO_2 , C_2H_2 , and a variety of $\text{C}_x\text{H}_y\text{F}_z$ compounds. The nature of this gas mixture changes if the test cell operates with cryogenic walls. In general, with cryogenic surfaces the quantity and complexity of the $\text{C}_x\text{H}_y\text{F}_z$ compounds increase, and COF is added to the mixture. These gases are formed from the reactions between C and F atoms in the plasma and previously adsorbed gases, including water vapor, on the cryosurfaces. It is felt that these reactions are somewhat aided by the strong VUV radiation which precedes each plasma impact.

4.6 SOLIDS PRODUCED BY THE ENGINE

Partially depolymerized Teflon is emitted in each engine firing. This material collects as a dark brown coating on all interior surfaces of the test chamber. Measurements with a quartz crystal microbalance fitted with a chopper wheel indicate that as much as 25 percent of the ablated fuel remains as a polymer and is accelerated to velocities comparable to that of the primary plasmoid. In addition to the polymer molecules emitted in each pulse there are periodic events which produce relatively large particles. The most abundant are carbon flakes ranging from 1 to 500 μm in diameter. It appears that these flakes are periodically torn from a carbon coating which gradually builds up on the electrodes of the engine. A second type of particle consists of carbon particles embedded in a Teflon matrix. These droplets are formed at the corners of the Teflon fuel blocks as a result of carbon buildup in the crevices between blocks. These particles exit the engine with relatively low velocities.

5.0 CONCLUSIONS

These tests provide a starting point to begin modeling the pulsed plasma engine. They provide a data base which describes the operation of this type engine and gives some insight as to the nature of the ablation and plasma discharge cycle. All of the data presented are referenced to a common starting point and thus can be directly compared on a temporal basis. Insofar as possible the effects of test chamber walls and events peculiar to a ground base space simulation facility operation have been noted. This information should be useful in evaluating data from tests on similar engines taken in other space simulation facilities. The effects of water vapor absorbed on surfaces should be particularly noted since this problem is ubiquitous in all vacuum test cells and is exacerbated by the periodic repressurizations required for engine modifications and instrumentation changes.

The engine firings (especially when fitted with the 80- μ fd capacitors) were in most respects extremely stable. The plasma formation and acceleration down the electrodes were reproducible from shot to shot and day to day with microsecond repeatability. However, there were random events such as carbon ion showers and the emission of 10- μ m-diam particles which were traceable to the engine. These phenomena may be peculiar to the design and construction of this particular engine and may not be typical of pulsed plasma engines, in general.

6.0 RECOMMENDATIONS

The tests conducted on this engine during the past months are reminiscent of the early contamination tests conducted at AEDC for bipropellant engines. In those tests the engine certainly produced more potential contamination in the form of unburned fuel than was acceptable. However, subsequent development of the engine and concurrent refinement of the contamination diagnostic techniques resulted in later tests which showed improved engine performance and minimal backflow contamination.

The pulsed plasma engine in its present configuration can meet acceptable performance standards (e.g., thrust, lifetime reliability, etc.) and is considered a valid option for performing station keeping and attitude control functions. However, the fact that as much as 25 percent of the fuel is ablated as high molecular weight polymers suggests that this engine has considerable potential for improved performance. Therefore, it is suggested that further investment should be made in its development. Some of the areas which should be investigated include:

1. Evaluation of the discharge oscillation with an attempt to suppress the third plasmoid: this portion of the discharge is most likely to produce thermal ablation with little electromagnetic acceleration.
2. Modification of the electrodes to try to minimize the carbon buildup: high-speed photographs of the plasma indicate that the magnetic fields apparently pinch the plasma so that it travels down the center of the anode; this might suggest a cylindrical tube rather than a flat plate geometry.
3. Carbon buildup: buildup between the fuel elements may be minimized by reducing the spacing between blocks.
4. Evidence in the high-speed photographs that some of the ablated gases are not confined to the arc region and instead flow out of the nozzle shield both above and below the electrodes: this could possibly be prevented by incorporating the electrodes into the surface of the shield.

Attempts were made during these tests to quantify some of the data obtained from diagnostics which might be useful in future backflow measurements. Reasonable success was obtained in calibrating the mass spectrometer for gaseous species. However, further work is required in the following areas:

1. Development of a system for *in situ* calibration of ion gases for short (millisecond) pressure pulses.
2. Coupling of a synchronized chopper, such as the one used in this test with QCM, with the mass spectrometer so that time-resolved data may be acquired for gases expanding or being reflected into the backflow region.
3. Application of molecular beam techniques for providing known molecular fluxes for *in situ* calibration of the mass spectrometer.
4. Development of an ionization-type detector which is sensitive to large polymer molecules. This might consist of an ionization region followed by a drift tube with a series of retarding grids ahead of a detector. This type of detector will be required if the plasma engines of the future still produce a significant quantity of the partially depolymerized Teflon molecules.

REFERENCES

1. Dawbarn, R., Steely, S.L., McGuire, R.L., and Price, L.L. "A Study of Test Techniques for Evaluating Ablative Plasma Engines in Vacuum Test Cells." AEDC-TR-81-8 (AD-A105875), October 1981.
2. Huddleston, R.H., and Leonard, S.L., eds. *Plasma Diagnostic Techniques*. Academic Press, New York, 1965.
3. Lochte-Holtgreven, W., ed. *Plasma Diagnostics*. North Holland Publishing Co., Amsterdam, 1968.
4. Kjeldseth Moe, O., et al. "A Spectral Atlas of the Sun Between 1175 and 2100 Angstroms." NRL Report 8056, December 31, 1976.
5. Dawbarn, R. "Cryosorption of Hydrogen by 12 — 20°K Carbon Dioxide Cryodeposits" AEDC-TR-67-125 (AD-655067), July 1967.
6. Cornu, A. and Massot, R. *Compilation of Mass Spectral Data*, Vols. I and II. Heyden, London, N.Y., Rheine, 1975 (Second Edition).
7. Dushman, S. *Scientific Foundations of Vacuum Technique*. J. Wiley and Sons, New York, 1958.

APPENDIX A

DETERMINATION OF EFFECTIVE R AND L FOR PLASMA DISCHARGE

The current flow can be described by the equation

$$i = D e^{-Rt/2L} \sin \left(\sqrt{\frac{1}{LC} - \frac{R^2}{4L^2}} t \right)$$

The damping term in this equation can be used to solve for the ratio of R/L , and then this ratio can be used in the oscillation term to solve for L and R , independently. Values of t , at i_{\max} , and t_2 , at i_{\min} , can be obtained from the data and used as follows:

$$\frac{i_{\max}}{i_{\min}} = e^{1/2(R/L)(t_2 - t_1)}$$

thus

$$2 \ln \left(\frac{i_{\max}}{i_{\min}} \right) = R/L(t_2 - t_1)$$

and

$$\underline{\underline{R/L = \frac{2 \ln \left(\frac{i_{\max}}{i_{\min}} \right)}{t_2 - t_1}}}$$

The current (i) passes through zero each time the argument of the sin function is equal to a multiple of π . Therefore, if the time, t_0 , is taken from the data, then

$$\left(\sqrt{\frac{1}{LC} - \frac{R^2}{4L^2}} \right) t_0 = \pi$$

$$\frac{1}{LC} = \left(\frac{\pi}{t_0} \right)^2 + \frac{1}{4} \left(\frac{R}{L} \right)^2$$

and

$$\underline{\underline{L = \frac{1}{C} \left[\left(\frac{\pi}{t_0} \right)^2 + \frac{1}{4} \left(\frac{R}{L} \right)^2 \right]^{-1}}}$$

For $C = 256 \times 10^{-6} \text{ F}$ (64- μfd capacitors)

then $L = 8.9 \times 10^{-8} \text{ H}$

and $R = 1.0 \times 10^{-2} \Omega$

thus $i = D e^{-0.107t} \sin 0.180t$

where $i = \text{amps}$

$t = \text{microseconds}$

For $C = 320 \times 10^{-6} \text{ F}$ (80- μfd Capacitors)

then $L = 9.7 \times 10^{-8} \text{ H}$

and $R = 1.3 \times 10^{-2} \Omega$

thus $i = D e^{-0.067t} \sin 0.66t$

NOMENCLATURE

A	Area, cm²
B	Magnetic field, Tesla
C	Capacitance, Farads
c	Velocity of light, Km/sec
D	Normalization constant
F	Coil shape factor
H	Henries
i	Current, amperes
K	Geometric constant
k	Conductance, l/sec
ℓ	Length, meters
N	Radiance, photons/sec-sr-cm²
n	Number
P	Pressure, torr
Q	Quantity of gas at standard temperature, torrℓ
R	Resistance, ohms Identification of right-hand Universal gas constant
r	Radius, cm
S	Signal from photomultiplier, volts
T	Temperature, °K
t	Time, sec
U	Velocity, Km/sec
V	Voltage, volts Volume, liters

β	Gage calibration constant
τ	Time constant, sec
λ	Wavelength, Å
Ω	Resistance, ohms

SUBSCRIPTS

f	Forepressure on calibrated leak, mm
g	Gage reading uncorrected
i	Initial value or input
o	Zero value